

May 2014

# Modeling of Instabilities and Self-Organization at the Frictional Interface

Vahid Mortazavi

*University of Wisconsin-Milwaukee*

Follow this and additional works at: <https://dc.uwm.edu/etd>



Part of the [Materials Science and Engineering Commons](#), and the [Mechanical Engineering Commons](#)

---

## Recommended Citation

Mortazavi, Vahid, "Modeling of Instabilities and Self-Organization at the Frictional Interface" (2014). *Theses and Dissertations*. 534.  
<https://dc.uwm.edu/etd/534>

This Dissertation is brought to you for free and open access by UWM Digital Commons. It has been accepted for inclusion in Theses and Dissertations by an authorized administrator of UWM Digital Commons. For more information, please contact [open-access@uwm.edu](mailto:open-access@uwm.edu).

# **Modeling of Instabilities and Self-organization at the Frictional Interface**

by

**Vahid Mortazavi**

A Dissertation Submitted in  
Partial Fulfillment of the  
Requirements for the Degree of

Doctor of Philosophy  
in Engineering

at

**The University of Wisconsin-Milwaukee**

**May 2014**

© Copyright by Vahid Mortazavi, 2014

All Rights Reserved

# **Abstract**

## **Modeling of Instabilities and Self-organization at the Frictional Interface**

By Vahid Mortazavi

The University of Wisconsin-Milwaukee, 2014

Under the Supervision of Professor Michael Nosonovsky

The field of friction-induced self-organization and its practical importance remains unknown territory to many tribologists. Friction is usually thought of as irreversible dissipation of energy and deterioration; however, under certain conditions, friction can lead to the formation of new structures at the interface, including in-situ tribofilms and various patterns at the interface.

This thesis studies self-organization and instabilities at the frictional interface, including the instability due to the temperature-dependency of the coefficient of friction, the transient process of frictional running-in, frictional Turing systems, the stick-and-slip phenomenon, and, finally, contact angle (CA) hysteresis as an example of solid-liquid friction and dissipation. All these problems are chosen to bridge the gap between fundamental interest in understanding the conditions leading to self-organization and practical motivation.

We study the relationship between friction-induced instabilities and friction-induced self-organization. Friction is usually thought of as a stabilizing factor; however, sometimes it leads to the instability of sliding, in particular when friction is coupled with another process. Instabilities

constitute the main mechanism for pattern formation. At first, a stationary structure loses its stability; after that, vibrations with increasing amplitude occur, leading to a limit cycle corresponding to a periodic pattern. The self-organization is usually beneficial for friction and wear reduction because the tribological systems tend to enter a state with the lowest energy dissipation.

The introductory chapter starts with basic definitions related to self-organization, instabilities and friction, literature review, and objectives. We discuss fundamental concepts that provide a methodological tool to investigate, understand and enhance beneficial processes in tribosystems which might lead to self-organization. These processes could result in the ability of a frictional surface to exhibit “self-protection” and “self-healing” properties. Hence, this research is dealing with the fundamental concepts that allow the possibility of the development of a new generation of tribosystem and materials that reinforce such properties.

In chapter 2, we investigate instabilities due to the temperature-dependency of the coefficient of friction. The temperature-dependency of the coefficient of friction can have a significant effect on the frictional sliding stability, by leading to the formation of “hot” and “cold” spots on the contacting surfaces. We formulate a stability criterion and perform a case study of a brake disk. We show that the mechanism of instability can contribute to poor reproducibility of aircraft disk brake tests reported in the literature. Furthermore, a method to increase the reproducibility by dividing the disk into several sectors with decreased thermal conductivity between the sectors is proposed.

In chapter 3, we study frictional running-in. Running-in is a transient period on the onset of the frictional sliding, in which friction and wear decrease to their stationary values. In this research, running-in is interpreted as friction-induced self-organization process. We introduce a

theoretical model of running-in and investigate rough profile evolution assuming that its kinetics is driven by two opposite processes or events, i.e., smoothening which is typical for the deformation-driven friction and wear, and roughening which is typical for the adhesion-driven friction and wear. To validate our modeling results, we examine experimentally running-in in ultrahigh vacuum friction tests for WC pin versus Cu substrate. We propose to calculate the Shannon entropy of a rough profile and to use it as a simple test for self-organization. We observe, theoretically and experimentally, how Shannon entropy as a characteristic of a rough surface profile changes during running-in, and quantifies the degree of orderliness of the self-organized system.

In chapter 4, we investigate the possibility of the so-called Turing-type pattern formation during friction. Turing or reaction-diffusion systems describe variations of spatial concentrations of chemical components with time due to local chemical reactions coupled with diffusion. During friction, the patterns can form at the sliding interface due to the mass transfer (diffusion), heat transfer, various tribochemical reactions, and wear. We present a mathematical model, and solve the governing equations by using a finite-difference method. The results demonstrate a possibility of such pattern-formation. We also discuss existing experimental data that suggest that tribofilms can form in-situ at the frictional interface due to a variety of friction-induced chemical reactions (oxidation, the selective transfer of Cu ions, etc.).

In chapter 5, we investigate how interfacial patterns including propagating trains of stick and slip zones form due to dynamic sliding instabilities. These can be categorized as self-organized patterns. We treat stick and slip as two phases at the interface, and study the effects related to phase transitions. Our results show how interfacial patterns form, how the transition between stick and slip zones occurs, and which parameters affect them.

In chapter 6, we use Cellular Potts Model to study contact angle (CA) hysteresis as a measure of solid-liquid energy dissipation. We simulate CA hysteresis for a droplet over the tilted patterned surface, and a bubble placed under the surface immersed in liquid. We discuss the dependency of CA hysteresis on the surface structure and other parameters. This analysis allows decoupling of the 1D (pinning of the triple line) and 2D effects (adhesion hysteresis in the contact area) and obtain new insights on the nature of CA hysteresis.

To summarize, we examine different cases in frictional interface and observe similar trends. We investigate and discuss how these trends could be beneficial in design, synthesis and characterization of different materials and tribosystems. Furthermore, we describe how to utilize fundamental concepts for specific engineering applications. Finally, the main theme of this research is to find new applications of concept of self-organization to tribology and the role played by different physical and chemical interactions in modifying and controlling friction and wear.

## **Acknowledgments**

First and foremost, I would like to thank my supervisor, Professor Michael Nosonovsky, not only for his invaluable advice and support, but also for his patience and the latitude he has allowed me. I owe a lot to him in discovering new and creative ways of looking into the most basic tribological problems.

I would also like to thank my co-advisor, Professor Roshan D'Souza, for his support, and introducing and guiding me into the world of Cellular Potts Modeling, in his Complex Systems Simulation Laboratory (CSSL).

Thanks are due to my three other committee members, Professors Kurt E. Beschoner, Konstantin Sobolev, and Professor Junhong Chen for their comments and time.

I also owe special thanks to Professor Wilfred T Tysoe and Dr. Octavio Javier Furlong for giving me a chance to do experiments about “running-in” project.

I would also like to thank Dr. Pradeep L. Menezes for his useful discussions, Ivan Komarov and Ali Bakhshinejad in CSSL for their helps and discussions about CPM.

Last but by no means least, I thank my father and mother in Iran, for all their love and support.



# Table of contents

## Table of Contents

Abstract .....	iii
List of Figures .....	xi
List of Tables .....	xv
Chapter 1 .....	1
Introduction.....	1
1.1. Self-organization, instabilities and friction: basic definitions.....	1
1.2. Self-organization: literature review .....	8
1.3. Entropy of Friction and dissipation .....	12
1.4. Criterion for self-organization.....	14
1.5. Self-organized criticality and stick–slip motion .....	16
1.6. Friction-induced instabilities.....	19
1.6.1. Instabilities due to velocity dependence of friction .....	19
1.6.2. Adams–Matrins (AMI) instabilities .....	20
1.6.3. Thermoelastic instabilities .....	21
1.6.4. Instabilities due to wear.....	22
1.7. Motivations of this study .....	23
1.8. Objectives of this study.....	25
Chapter 2.....	28
Stability of Frictional Sliding with the Coefficient of Friction depended on the Temperature .....	28
2.1. Objective .....	28
2.2. Background .....	28
2.3. Mathematical modeling.....	30
2.4. Reproducibility of disk brake test results.....	38
2.4.1. Numerical Model .....	38
2.4.2. Stability analysis.....	40
2.4.3. Results and discussion .....	42
2.5. Conclusion.....	46

Chapter 3.....	48
Running-in as a Self-organized process .....	48
3.1. Objective .....	48
3.2. Background .....	48
3.3. Shannon Entropy as a characteristic of a rough surface .....	50
3.4. Thermodynamic Model for surface roughness kinetics .....	53
3.5. Experimental.....	57
3.6. Results.....	58
3.7. Conclusion.....	62
Chapter 4.....	64
Frictional Turing systems .....	64
4.1. Objective .....	64
4.2. Turing systems and self-organization .....	64
4.3. Numerical simulation of frictional Turing systems .....	66
4.4. Results .....	69
4.5. Discussion.....	76
4.6. Conclusion.....	81
Chapter 5.....	82
Stick-slip motion and self-organization .....	82
5.1. Objective .....	82
5.2. Different models of stick–slip motion.....	82
5.3. Stick and slip friction phases.....	87
5.4. Numerical modeling.....	88
5.5. Conclusion.....	92
Chapter 6.....	93
Contact angle hysteresis as a solid-liquid energy dissipation.....	93
6.1. Objective .....	93
6.2. Numerical modeling of wetting .....	93
6.3. Contact angle hysteresis .....	97
6.4. The Cellular Potts Model.....	99
6.5. The Cellular Potts Modeling of wetting .....	102
6.6. Results.....	105

6.7. Conclusion.....	112
Chapter 7.....	113
Final conclusions .....	113
References.....	118

## List of Figures

- **Figure 1.1.** (a) A thermodynamic system as a quantity of matter or a region, separated from its surroundings (b) Closed and open thermodynamic systems
- **Figure 1.2.** A frictionless pendulum as an example of reversible process
- **Figure 1.3.** Some examples of self-organization: (a) Bénard cells (b) Reaction-diffusion systems (c) Belousov–Zhabotinsky reaction (a nonlinear chemical oscillator) (d) Purified cell-division proteins can form spiral waves
- **Figure 1.4.** Heat flow away from the frictional interface (Nosonovsky, 2010a)
- **Figure 1.5.** The sandpile model. Addition of a grain to the sandpile can have (1) the avalanche effect or (2) the local effect (Nosonovsky & Bhushan, 2009).
- **Figure 1.6** (a) A water drop on an inclined surface. (b) As the tilt angle  $\alpha$  grows, the critical state can be reached with a disappearing energy barrier between the wetted and dry states, so that the liquid advances (Nosonovsky & Bhushan, 2009).
- **Figure 1.7.** The pattern of propagating stick and slip zones can lead to friction reduction, as  $F < \mu W$  (Nosonovsky and Adams, 2001)
- **Figure 1.8.** Various mechanisms can create positive or negative feedbacks that lead to instabilities during friction (Nosonovsky, 2010).
- **Figure 2.1.** Response of the system to different values of values of  $\epsilon$ : (a) 0.0001, (b) 0.00005 and (c) 0.00001.  $\tau$  is the dimensionless time (Mortazavi et al., 2012).
- **Figure 2.2.** Schematic of a brake disk (Mortazavi et al., 2012).
- **Figure 2.3.** Temperature-dependence of the coefficient of friction (Mortazavi et al., 2012).
- **Figure 2.4.** Effect of the number of domains,  $N$ , on the reproducibility of the brake test (Mortazavi et al., 2012).

- **Figure 2.5.** Response of system to perturbation in whole domain for different values of  $\epsilon$ : (a) 0.0001, (b) 0.00001.  $\tau$  is the dimensionless time (Mortazavi et al., 2012).
- **Figure 2.6.** Simulation results for  $T$  at 1, 10, 100, and 1000 timesteps (a) random fluctuation (b) distribution of the average value of the coefficient of friction after 100 runs (Mortazavi et al., 2012).
- **Figure 2.7.** Simulation results for  $T$  at 1, 10, 100, and 1000 timesteps (a) random fluctuation (b) distribution of the average value of the coefficient of friction after 100 runs (Mortazavi et al., 2012).
- **Figure 3.1.** Example of how Shannon Entropy could be calculated for Rough Surface Profile
- **Figure 3.2.** For a periodic rectangular profile, the Shannon entropy is between 0 and 0.3.
- **Figure 3.3.** A feedback loop model (top) and its presentation in Simulink (bottom). Two simultaneous processes (adhesion and deformation) affect surface roughness parameter in different manners. Consequently, an equilibrium value of roughness exists, which corresponds to minimum friction.
- **Figure 3.4.** The time-dependence of the coefficient of friction and roughness parameter during the running-in simulated with Simulink for  $A=B$  and  $A \neq B$ . For  $A=B$ , while roughness reaches its equilibrium value, the coefficient of friction always decreases. Therefore, self-organization of the rough interface results in the decrease of friction and wear. For  $A \neq B$  the coefficient of can decrease or increase depending on the initial value of roughness.
- **Figure 3.5.** Friction coefficient change during running-in process.
- **Figure 3.6.** Variations of different roughness parameters during running-in period: Root Mean Square, Roughness Average, Extreme-value Height, Skewness, and Kurtosis respectively.
- **Fig. 3.7.** Shannon entropy during running-in period.
- **Figure 4.1.** Linear stability analysis. Region 1: uniform steady state, region 2: Oscillating instability, region 3: Turing patterns.

- **Figure 4.2.** Time evolution of amounts of  $u$  and  $v$  in different time steps, at  $t = 0, 0.001, 0.005, 0.01$ , and  $0.1$  (First case)
- **Figure 4.3.** Time evolution of  $u$  and  $v$  values in different time steps,  $t = 0, 0.001, 0.005, 0.01, 0.05$  and  $0.1$  (Second case)
- **Figure 4.4.** Time evolution of  $u$  and  $v$  values in two different time steps (Third case, using equations 4.18 and 4.19)
- **Figure 4.5.** Time evolution of  $u$  and  $v$  values in different time steps (Third case, using equations 4.18 and 4.20)
- **Figure 4.6.** Schematic presentation of the selective layer (b) obtained by friction between a surface of steel and (a) a surface of copper alloy (bronze)
- **Figure 5.1.** A typical mass-spring system. The stiffness  $K$  can represent an actual spring or an effective stiffness of the loading apparatus.  $M$  and  $V$  also represent mass, and velocity, respectively
- **Figure 5.2.** Three different sliding regimes for the system in Figure 5.1
- **Figure 5.3.** Schematic picture of spring-mass system;  $N$  denotes number of masses
- **Figure 5.4.** Distribution of Kinetic friction force for different masses (Number of mass = 1000)
- **Figure 5.5.** Total applied force versus slip zone (number of masses)
- **Figure 5.6.** Average friction force versus time
- **Figure 6.1.** Schematic of a 2D lattice and a spin flipping attempt in CPM.
- **Figure 6.2.** Initial configuration of simulation for droplet along a tilted homogeneous ( $f_{SL}=1$ ) solid surface
- **Figure 6.3.** Contact angle hysteresis versus solid-liquid fraction for droplet on the tilted surface; for three different drop diameters ( $R$ )
- **Figure 6.4.** Advancing and receding contact angles for different surface energies of solid-liquid
- **Figure 6.5.** Advancing and receding contact angles for different drop diameters

- **Figure 6. 6.** Advancing and receding contact angles versus titled angle for a droplet on the tilted surface
- **Figure 6. 7.** Advancing and receding contact angles versus titled angle for a bubble submerged in liquid
- **Figure 6.8.** Comparison of CA hysteresis for bubbles and droplet of the same surface energies
- **Figure 6. 9.** CA hysteresis obtained by experiment for (a) different droplet sizes on concrete TiO<sub>2</sub> coated tile, and for bubble (b) different bubble sizes on Al sample, for different tilt angles (TA)

## List of Tables

- **Table 1.1.** Self-organization effects in tribosystems (Nosonovsky, 2010)
- **Table 4.1.** Summary of different experimental pattern formation evidences discussed in literature (Mortazavi and Nosonovsky, 2011b)



# Chapter 1

## Introduction

### 1.1. Self-organization, instabilities and friction: basic definitions

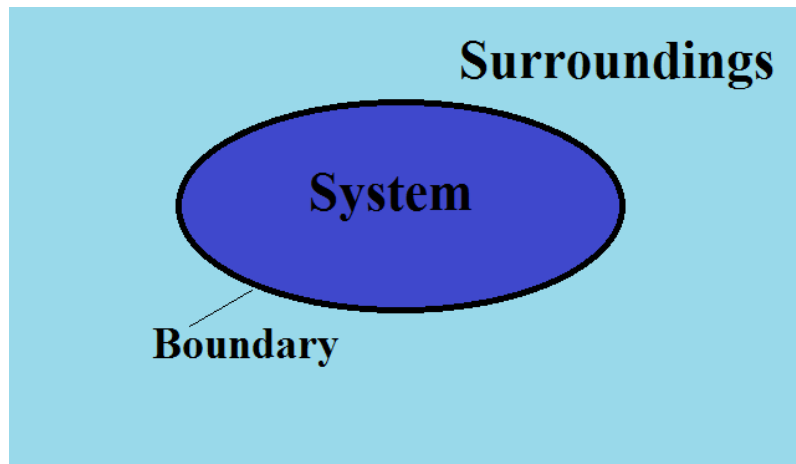
Tribology is defined as the science and technology of interacting surfaces in relative motion, or, in other words, the study of friction, wear and lubrication. Friction and wear are usually viewed as irreversible processes, which lead to energy dissipation (friction) and material deterioration (wear). However, it is known that under certain circumstances frictional sliding can result in the formation (self-organization) of spatial and temporal patterns.

Study of the concept of self-organization in tribology is not an old research area, nor is it old in other scientific fields. The development of this concept is one of the achievements of modern physics, which deals with complex processes of nature (Gershman & Bushe, 2006). The concept is based on the ideas of irreversible thermodynamics (Nosonovsky & Bhushan, 2009; Prigogine, 1980). Major progress in this area is associated with Prigogine (1980).

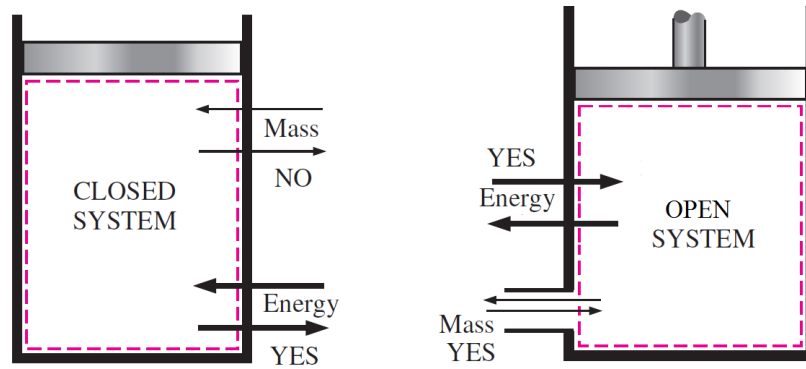
To give a definition of self-organization, and to explain its function at the frictional interface, this section will review some basic concepts of thermodynamics. Then, it will discuss how instabilities of a tribosystem can precede the self-organizing phenomena. Through this introduction, we will make a framework for study for instabilities and self-organization at the frictional interface in this thesis.

Let's start with definition of a thermodynamics system. Thermodynamically, a system is a quantity of matter or a region which is separated through its boundaries from its outside mass or region as it is called the surroundings (**Fig 1.1a**). A Thermodynamic system can be open or closed. An open system can exchange energy and mass with its surroundings, while mass cannot cross closed system's boundaries (**Fig 1.1b**).

A thermodynamics system is in equilibrium state, if there are no unbalanced potentials (or driving forces) within the system. A system in equilibrium experiences no changes when it is isolated from its surroundings (Cengel, 2001). The word equilibrium implies a state of balance. By contrast, in non-equilibrium system, there are net flows of mass or energy, or occurrence of phase change.



(a)



(b)

**Figure 1.1 (a) A thermodynamic system as a quantity of matter or a region, separated from its surroundings  
(b) Closed and open thermodynamic systems**

Thermodynamically, friction is a process which occurs in the open and non-equilibrium systems. This is an irreversible process; a process which cannot reverse itself and restore the system to its initial state. A reversible process is defined as a process that can be reversed without leaving any trace on the surroundings (**Fig 1.2**).

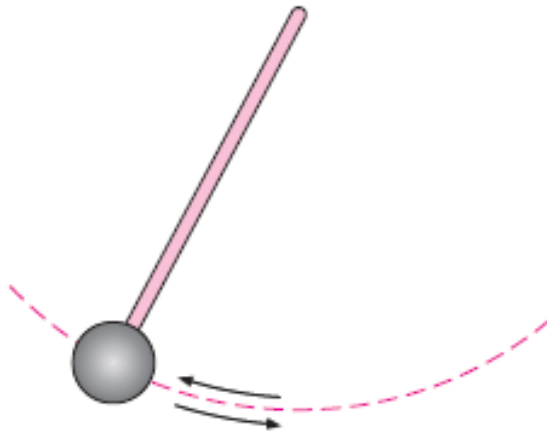


**Figure 1.2 A frictionless pendulum as an example of reversible process**

Clausius in the 1850s introduced entropy,  $S$ , as a measure of irreversibility of the thermodynamic system

$$dS = \frac{dQ}{T} \quad (1.1)$$

where  $T$  is the temperature and  $Q$  is the heat. When heat  $dQ$  is transferred from a body with temperature  $T_1$  to a body with temperature  $T_2$ , the entropy grows by the amount  $dS = dQ/T_1 - dQ/T_2$ . Thus, if heat is transferred from a hotter body to a colder one ( $T_1 > T_2$ ), the net entropy grows ( $dS > 0$ ). This provides a convenient formal basis for the second law of thermodynamics, stating that the net entropy of a closed system either remains constant (for a reversible process) or grows (for an irreversible process).

During friction as an irreversible, dissipative process, heat is generated. For example, when the friction force  $F$  is applied to a body that passes the distance  $dx$ , the energy  $dQ = Fdx$  is dissipated into the surroundings, and the entropy of the surroundings increases for the amount of  $dS = (\frac{F}{T})dx$ .

In 1877, L. Boltzmann suggested another definition of entropy using the statistical thermodynamics approach and the concept of microstates

$$S = k \ln \Omega \quad (1.2)$$

where  $k$  is Boltzmann's constant and  $\Omega$  is the number of microstates corresponding to a given macrostate. Microstates are arrangements of energy and matter in the system, which are distinguishable at the atomic or molecular level, but are indistinguishable at the macroscopic level (Craig 1992). A system tends to evolve into a less-ordered (more random) macrostate that has a greater number of corresponding microstates, and thus the entropy given by Eq. (1.2) increases.

From the preceding definition, it can be found that entropy depends on the energy of the system. Hence, irreversible processes are accompanied not only by the growth of entropy but

also by the change of energy within the system (internal energy). In this case, we have to consider the reduction of internal energy because, in an equilibrium state, entropy reaches to the possible maximum value whereas energy has the possible minimum value (Ebeling, 1990). Thus, irreversible processes should be accompanied by the dissipation of energy.

So, the change of entropy  $dS$  consists of two parts (Kostetsky, 1970). It includes a flow of entropy  $d_e S$ , caused by an interaction with the environment, and  $d_i S$ , a part of entropy change due to the processes that are taking place within the system (entropy production):

$$dS = d_e S + d_i S \quad (1.3)$$

And always

$$d_i S \geq 0 \quad (1.4)$$

The entropy production according to Eq. (1.4) is a general definition of irreversibility, which states entropy of irreversible system always increases. It is worth noting that the division of entropy change on two components (Eq. 1.3) allows the establishment of a distinction between closed (isolated) and open systems. Distinction is shown with  $d_e S$ , which takes into account the change of entropy due to an exchange of matter in open systems.

The concept of self-organization is based on the ideas of irreversible thermodynamics (Prigogine, 1961). Prigogine's theorem states that while the net entropy grows in most thermodynamic systems, some of them may lead to a process to decrease entropy production (Prigogine 1961). To do that, these systems should be thermodynamically open and operate far from thermodynamic equilibrium and can exchange energy, matter and entropy with the environment. The physical meaning of Prigogine's theorem is as follows: a system that cannot come to equilibrium attempts to enter a condition with the lowest energy dissipation. That is why we can expect that the wear rate under stable conditions will be minimal with an extremely low

contribution to entropy production (Gershman & Bushe, 2006). Mechanism of leading into this low entropy production is forming of some new structures that are called dissipative or secondary structures and the process of dissipative structure formation is called Self-organization. These dissipative structures can be spatial, temporal, or functional (Kondepudi & Prigogine, 2000). Spontaneous formation of dissipative structures is a result of perturbations that can be realized only in open systems, which exchange energy, matter, and entropy with their environments (Kondepudi & Prigogine, 2000).

In last two decades, the idea of self-organization of systems operating far from equilibrium has been widely used for fundamental research purposes in many areas of science (**Fig 2.1**). For example, we can mention Bénard cells in boiling liquid (Koschmieder,- 1993), reaction and diffusion systems (Mortazavi & Nosonovsky, 2012), the instability that arises at fusion, the solidification caused by pulse laser irradiation of crystals (Ebeling et al., 1990), space–time ordering at the liquid-phase interface during mechanical deformation (Prigogine, 1997), structures growing at the liquid–solid interface in the course of the growth of a crystal (Prigogine & Kondepudi, 1990), dissipative structures that are formed during the unidirectional growth of binary alloys from liquid (Prigogine, 1997), spatial heterogeneity as domains with various chemical concentration in rocks (Ebeling et al., 1990), and chemical reactions in biochemical systems (Prigogine & Kondepudi, 1990).

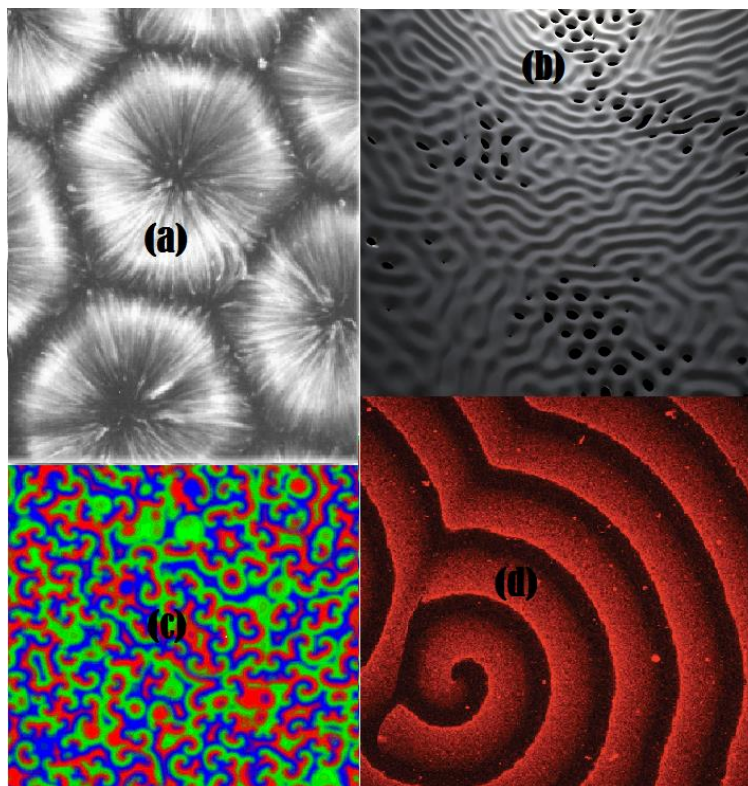


**Figure 1.3. Some examples of self-organization: (a) Bénard cells (b) Reaction-diffusion systems (c) Belousov–Zhabotinsky reaction (a nonlinear chemical oscillator) (d) Purified cell-division proteins can form spiral waves**

According to the theorem by Prigogine, only after passing through instability can the process of self-organizing begin. During regular deviation from equilibrium, i.e., when an increase occurs in a parameter that describes a system's condition or its external influence, the steady (and close-to-equilibrium) state is stable. However, if a certain critical value of one of the parameters in the system is exceeded, the state of the system could become unstable. The new order that has been established within the system could correspond to an ordered state, i.e., a new state with smaller entropy in comparison to a chaotic condition (Gershman & Bushe, 2006).

The irreversible processes of structure formations are associated with non-equilibrium phase transformations. These transformations are connected with specific bifurcation or instability points where the macroscopic behavior of the system changes qualitatively and may

either leap into chaos or into greater complexity and stability (Capra, 1996). In the latter case, as soon as the system passes these specific points, its properties change spontaneously because of self-organization and formation of dissipative structures (Fox-Rabinovich, 2007).

As it was described, friction and wear could be characterized by exchange of matter and energy with the environment. The flow of heat, entropy, and material away from the interface during the dry friction and wear can lead to formation of secondary structures. The secondary structures are either patterns that form at the interface (e.g., stick and slip zones) or those formed as a result of mutual adjustment of the bodies in contact. Formation of these structures and the transition to the self-organized state with low friction and wear occurs through the destabilization of the steady-state (stationary) sliding. The entropy production rate reaches its minimum at the self-organized state. Therefore, the self-organization is usually beneficial for the tribological system, as it leads to the reduction of friction and wear (Nosonovsky & Bhushan, 2009).

As it was mentioned concepts of self-organization and the destabilization of the steady-state are related together. Next sections of this chapter will concentrate on mechanisms of self-organization and instabilities at the frictional interface. Then, the practical problems which can be categorized as evidences of these concepts will be introduced. Each of these problems will be the main focus in one of the next chapters.

## **1.2. Self-organization: literature review**

Historically, first attempts to investigate friction-induced self-organization were made in Russia starting the 1970s. Several groups can be mentioned. First, B. Kostetsky and L. Bershadsky (1992, 1993) investigated the formation of the self-organized “secondary structures.” According to Bershadsky, friction and wear are two sides of the same phenomenon and they represent the tendency of energy and matter to achieve the most disordered state (Nosonovsky,



2010). However, the synergy of various mechanisms can lead to the self-organization of the secondary structures, which are “nonstoichiometric and metastable phases,” whereas “the friction force is also a reaction on the informational (entropic) excitations, analogous to the elastic properties of a polymer, which are related mostly to the change of entropy and have the magnitude of the order of the elasticity of a gas.” (Bershadsky, 1993).

These ideas were influenced by the theory of self-organization developed by Prigogine (1968) who used the ideas of the non-equilibrium thermodynamics to describe the processes of self-organization (Nicolis and Prigogine, 1977). At the same time, in the end of the 1970s, the concept of “Synergetics” was suggested by H. Haken (1983) as an interdisciplinary science investigating the formation and self-organization of patterns and structures in open systems, which are far from thermodynamic equilibrium.

The second Russian group to mention is Bushe and Gershman, which their results were summarized in the edited book by Fox-Rabinovich and Totten (2006). The third group is Garkunov (2004) and co-workers, who claimed the discovery of the synergetic “non-deterioration effect” also called the “selective transfer” (Nosonovsky, 2010).

In the English language literature, the works by Klamecki (1980) were the first to use the concepts of the non-equilibrium thermodynamics to describe friction and wear. His work was extended by Zmitrowicz (1987), Dai et al. (2000), Doelling et al. (2000) and others. Abdel-Aal (2006) developed a model to predict and explain the role of wear as a self-organizing occurrence in tribosystems. Indicating that in the work of Klamecki, the entropy flow due to mass loss was not explicitly expressed so that a direct correlation between wear and entropy was not apparent, Abdel-Aal (2006) examined the relationship between wear and the generation of entropy within the mechanically affected zone, MAZ, of a sliding material.

An important entropic study of the thermodynamics of wear was conducted by Bryant et al. (2008), who introduced a degradation function and formulated the Degradation-Entropy Generation theorem in their approach intended to study the friction and wear in complex. They note that friction and wear, which are often treated as unrelated processes, are in fact manifestations of the same dissipative physical processes occurring at sliding interfaces. The possibility of the reduction of friction between two elastic bodies due to a pattern of propagating slip waves was investigated by Adams (1998) and Nosonovsky and Adams (2001), who used the approach of the theory of elasticity.

A completely different approach to friction-induced self-organization is related to the theory of dynamical systems and involves the investigation of friction test results as time-series. Since the 1980s, it has been suggested that a specific type of self-organization, called “self-organized criticality,” plays a role in diverse “avalanche-like” processes, such as the stick-slip phenomenon during dry friction. The researches of Zypman (2003) and Ferrante (Adler, 2004; Buldyrev, 2006; Fleurquin, 2010) and others deal with this topic.

A different approach to describe some mechanisms resulting in self-organization was based on the reaction-diffusion systems and their important class the “Turing systems” (Kagan, 2010). Mortazavi and Nosonovsky (2011) investigated whether reaction-diffusion systems can describe certain types of friction-induced pattern formation involving heat transfer and diffusion-like mass transfer due to wear. In somehow similar trend, Nosonovsky and Bushan (2009, 2010) and Nosonovsky et al. (2009) suggested treating self-lubrication and surface-healing as a manifestation of self-organization. They noted that the orderliness at the interface can increase (and, therefore, the entropy is decreased) at the expense of the entropy either in the bulk of the

body or at the microscale. They also suggested that self-organized spatial patterns (such as interface slip waves) can be studied by the methods of the theory of self-organization.

Nosonovsky (2010a and b), Nosonovsky and Bhushan (2009) and Nosonovsky et al. (2009) suggested entropic criteria for friction-induced self-organization on the basis of the multiscale structure of the material (when self-organization at the macroscale occurs at the expense of the deterioration at the microscale) and coupling of the healing and degradation thermodynamic forces. Table 1.1 summarizes their interpretation of various tribological phenomena, which can be interpreted as self-organization. In addition, self-organization is often a consequence of coupling of friction and wear with other processes, which creates a feedback in the tribosystem.

**Table 1.1.** Self-organization effects in tribosystems (Nosonovsky, 2010)

Effect	Mechanism/driving force	Condition to initiate	Final configuration
Stationary microtopography distribution after running in	Feedback due to coupling of friction and wear	Wear affects microtopography until it reaches the stationary value	Minimum friction and wear at the stationary microtopography
In situ tribofilm formation	Chemical reaction leads to the film growth	Wear decreases with increasing film thickness	Minimum friction and wear at the stationary film thickness
Slip waves	Dynamic instability	Unstable sliding	Reduced friction
Self-lubrication	Embedded self-lubrication mechanism	Thermodynamic criteria	Reduced friction and wear
Surface-healing	Embedded self-healing mechanism	Proper coupling of degradation and healing	Reduced wear

### 1.3. Entropy of Friction and dissipation

Consider a rigid body sliding upon a flat solid surface with the sliding velocity  $V=dx/dt$  (**Fig. 1.4**). The normal load  $W$  is applied to the body and the friction force  $F=\mu W$  is generated (Nosonovsky and Bhushan, 2009). The work of the friction force is equal to the dissipated energy, and, therefore, it can be assumed that all dissipated energy is converted into heat (Nosonovsky, 2010a)

$$dQ = \mu W dx \quad (1.5)$$

The rate of entropy generation during friction is given by

$$\frac{dS}{dt} = \frac{\mu W V}{T} \quad (1.6)$$

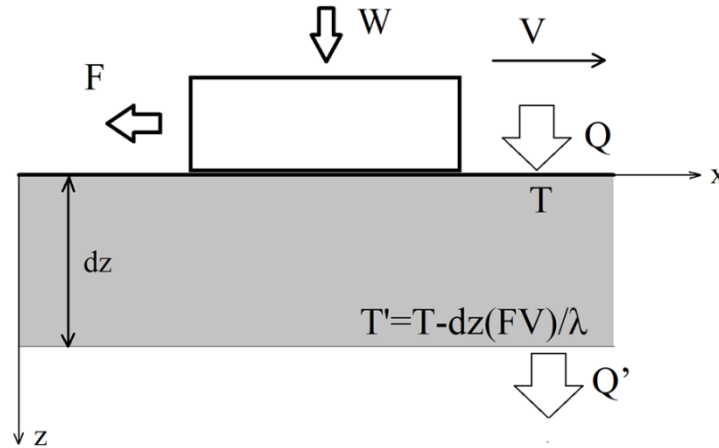


**Figure 1.4. Heat flow away from the frictional interface (Nosonovsky, 2010a)**

It is noted that friction is a non-equilibrium process. When a non-equilibrium process, which can be characterized by a parameter  $q$  (a generalized coordinate), occurs, a generalized thermodynamic force  $X$  that drives the process can be introduced in such a manner that the work of the force is equal to  $dQ=Xdq$ . The flux (or flow rate)  $J = \dot{q}$  is associated with the generalized coordinate. For many linear processes the flow rate is linearly proportional to  $X$ . For sliding

friction, the flow rate  $J=V$ , and the thermodynamic force  $X=\mu W/T$ . Note that, for the Coulombian friction,  $J$  is not proportional to  $X$ , which is the case for the viscous friction. Nosonovsky (2010b) discussed in detail the problem of bringing the linear friction in compliance with the linear thermodynamics.

The net entropy growth rate for frictional sliding of rigid bodies is given by Eq. (1.6). However, if instead of the net entropy, the entropy per surface area at the frictional interface is considered, the rate equation becomes more complicated. Nosonovsky (2010a) considered the 1D flow of entropy near the infinite interface in the steady-state situation, and suppose the flow is equal to entropy generation. Heat  $dQ$  is generated at the interface in accordance with Eq. (1.5). For simplicity, Nosonovsky (2010a) assumed that all generated heat is dissipated in one of the two contacting bodies and ignore the division of heat between the two bodies. The heat is flown away from the interface in accordance with the heat conduction equation

$$\lambda \frac{\partial T}{\partial z} = \mu W V \quad (1.7)$$

where  $z$  is the vertical coordinate (distance from the interface), and  $\lambda$  is the heat conductivity. Consider a thin layer near the interface with the thickness  $dz$ . The temperature drop across the layer is  $dT=(\mu W V/\lambda)dz$ . The ratio of the heat released at the interface,  $dQ$ , to that radiated at the bottom of the layer,  $dQ'$ , is equal to the ratio of the temperatures at the top and at the bottom of the layers

$$\frac{dQ'}{dQ} = \frac{T - \mu W V dz / \lambda}{T} \quad (1.8)$$

Therefore, the energy released at the subsurface layer of depth  $dz$  is given by (Nosonovsky and Bhushan, 2009)

$$dq = \frac{dQ - dQ'}{dz} = dQ \frac{\mu WV}{\lambda T} = \frac{(\mu WV)^2}{\lambda T} \quad (1.9)$$

Thus the entropy in the subsurface layer,  $dS/dt = dq/T$ , is given by

$$\frac{dS}{dt} = \frac{(\mu WV)^2}{\lambda T^2} \quad (1.10)$$

Note that  $S$  in Eq. (1.10) is entropy per unit surface area and thus it is measured in  $JK^{-1}m^{-2}$ , unlike the total entropy is Eq. (1.6), which is measured in  $JK^{-1}$  (Nosonovsky and Bhushan, 2009 & 2010).

The difference between Eq. (1.6) and Eq. (1.10) is that the latter takes into account the thermal conductivity and that in Eq. (1.6) gives the net entropy rate, while Eq. (1.10) gives the rate of entropy in the subsurface layer. Note the form for the thermodynamic flow is now  $J = \mu WV$ , and the thermodynamic force is  $X = \mu WV/(\lambda T^2)$  (Nosonovsky, 2010).

#### 1.4. Criterion for self-organization

The stability condition for the thermodynamic system is given in the variational form by

$$\frac{1}{2} \delta^2 \dot{S} = \sum_k \delta X_k \delta J_k \geq 0 \quad (1.11)$$

where  $\delta^2 \dot{S}$  is the second variation of entropy production rate (Nosonovsky and Bhushan, 2009) and  $k$  is the number of the generalized forces and flows. Eq. (1.11) states that the energy dissipation per unit time at the steady state should be at its minimum, or the variations of the flow and the force should be of the same sign. When equation (1.11) is not satisfied, the system is driven away from equilibrium, which creates the possibility for self-organization.

Another form of Eq. (1.11) is given by (Fox-Rabinovich et al. 2007):

$$\frac{\partial}{2\partial t}(\delta^2 S) = \frac{1}{2} \delta^2 \left( \frac{(\mu WV)^2}{\lambda T^2} \right) = \delta X \delta J = \delta(\mu WV) \delta \left( \frac{\mu WV}{\lambda T^2} \right) \geq 0 \quad (1.12)$$

Eq. (1.12) is a powerful tool to study frictional contact. It involves the coefficient of friction, thermal conductivity and the sliding velocity. In the case of any interdependence between these values, the stability of the system should be analyzed. It can be assumed (Nosonovsky and Bhushan, 2009) that the coefficient of friction depends on  $V$  and  $T$ , while the thermal conductivity depends on  $V$ .

$$\mu = \mu(V, T) \quad \lambda = \lambda(V) \quad (1.13)$$

The stability condition given by Eq. (1.24) takes the form of (Nosonovsky and Bhushan, 2009)

$$\frac{1}{2} \delta^2 \dot{S} = \frac{W^2}{\lambda T^2} \left( \frac{\partial \mu}{\partial V} V + \mu \right) \left( \frac{\partial \mu}{\partial V} V + \mu - \frac{\mu V}{\lambda} \frac{\partial \lambda}{\partial V} \right) (\delta V)^2 - \left( \frac{2V^2 W^2 \mu}{\lambda T^3} \right) \frac{\partial \mu}{\partial T} (\delta T)^2 \geq 0 \quad (1.14)$$

The stability condition is violated either if the coefficient of friction grows with temperature ( $\frac{\partial \mu}{\partial T} > 0$ ) or if, in the first term, the parentheses have different signs. The latter is possible if  $\frac{\partial \mu}{\partial V} < 0$ , and  $\frac{\partial \lambda}{\partial V} > 0$ , or if  $\frac{\partial \mu}{\partial V} > 0$ , and  $\frac{\partial \lambda}{\partial V} < 0$ . When the stability condition is violated, the Tribological system is likely to enter the self-organizing regime, with reduced friction and wear.

When the coefficient of friction and the thermal conductivity depend upon material's microstructure,  $\phi$ , it may be convenient to introduce a parameter  $\psi$  that characterizes the microstructure of the surface (for example, the density of a micropattern), so that

$$\mu = \mu(\psi, \phi) \quad (1.15)$$

$$\lambda = \lambda(\psi, \phi)$$

The stability condition given by Eq. (1.24) takes the form of

$$\frac{1}{2} \delta^2 \dot{S} = \frac{V^2 W^2}{T^2} \frac{\partial \mu}{\partial \phi} \left( \frac{1}{\lambda} \frac{\partial \mu}{\partial \phi} - \frac{\mu}{\lambda^2} \frac{\partial \lambda}{\partial \phi} \right) (\delta \phi)^2 \geq 0 \quad (1.16)$$

The stability condition can be violated if

$$\frac{\partial \mu}{\partial \phi} \frac{\partial \lambda}{\partial \phi} < 0 \quad (1.17)$$

It is known from non-equilibrium thermodynamics that when the secondary structure is formed, the rate of entropy production reduces (Fox-Rabinovich et al., 2007). Therefore, if Eq. (1.29) is satisfied, the frictional force and wear can reduce. By selecting appropriate values of  $\psi$  (e.g., the density of a micropattern), the condition of Eq. (1.17) can be satisfied. Note, that the wear rate is related to the rate of surface entropy production

$$\frac{dw}{dt} = B \frac{dS}{dt} = YJ \quad (1.18)$$

It is suggested to use the theory presented in this section to optimize the microstructure of a composite material in order to ensure that the self-organized regime occurs. For that end, the dependencies Eq. (1.17) should be investigated experimentally and their derivatives obtained. Following that the value of  $\psi$  should be selected, which provides the best chances for the transition to the self-organized regime (Nosonovsky, 2010a).

### 1.5. Self-organized criticality and stick–slip motion

Self-organized criticality (SOC) is a concept in the theory of dynamic systems that was introduced in the 1980s (Bak, 1996). The best-studied example of SOC is the ‘sandpile model’, representing grains of sand randomly placed into a pile until the slope exceeds a threshold value, transferring sand into the adjacent sites and increasing their slope in turn (**Fig. 1.5**). Placing a random grain at a particular site may have no effect, or it may trigger an avalanche that will



affect many sites at the lattice. Thus, the response does not depend on the details of the perturbation (Nosonovsky & Bhushan, 2009). It is worth mentioning that the scale of the avalanche is much greater than the scale of the initial perturbation.

There are typical external signs of an SOC system, such as the power-law behaviour (the magnitude distribution of the avalanches) and the ‘one-over-frequency’ noise distribution (Bak, 1996). The concept has been applied to such diverse fields as physics, cellular automata theory, biology, economics, sociology, linguistics and others (Nosonovsky & Bhushan, 2009).

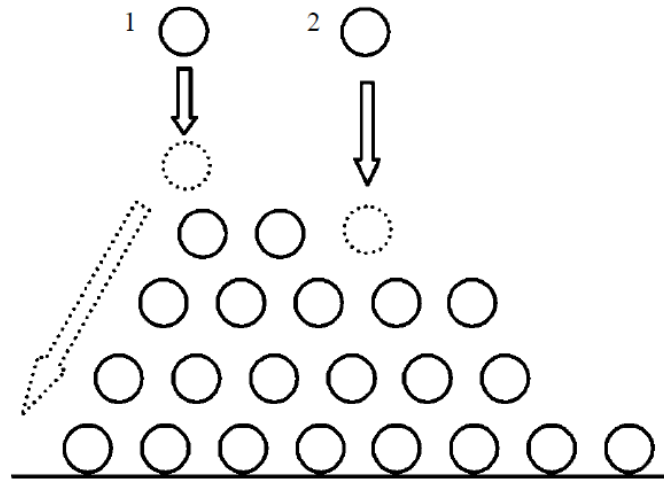


**Figure 1.5. The sandpile model. Addition of a grain to the sandpile can have (1) the avalanche effect or (2) the local effect (Nosonovsky & Bhushan, 2009).**

In the case of dry frictional sliding, it has been suggested that a transition between the stick and slip phases during dry friction may be associated with the SOC, since the slip is triggered in a similar manner to the sandpile avalanches and earthquake slides. Zypman et al. (2003) showed that, in a traditional pin-on-disc experiment, the probability distribution of slip zone sizes follows the power law. In a later work, the same group found nanoscale SOC-like

behaviour during atomic force microscopic studies of at least some materials (Zypman et al. 2003; Buldyrev et al. 2006). Thus ‘stick’ and ‘slip’ are two phases, and the system tends to achieve the critical state between them: in the stick state, elastic energy is accumulated until slip is initiated, whereas energy release during slip leads, again, to the stick state.

During wetting, SOC also apparently plays a role in wetting behaviours (di Meglio 1992; Nosonovsky & Bhushan 2008c). Frictional stick–slip motion and liquid spreading are examples of ‘avalanche’-like behaviour, when a small input into the system leads to a big change. For example, a droplet on an inclined surface starts its motion when the tilt angle exceeds a certain critical value, so that the gradient of gravity exceeds the energy barriers associated with the pinning of the triple line (Nosonovsky & Bhushan, 2009). Wetted and dry states are two stable states with an energy barrier between them (**Fig 1.6**). When the barrier vanishes, the liquid spreads. For example, when a sessile droplet is placed on an inclined surface, increasing the tilt angle increases the energy gradient due to the gravity, which overcomes the energy barrier at a certain critical value. The liquid starts to spread.

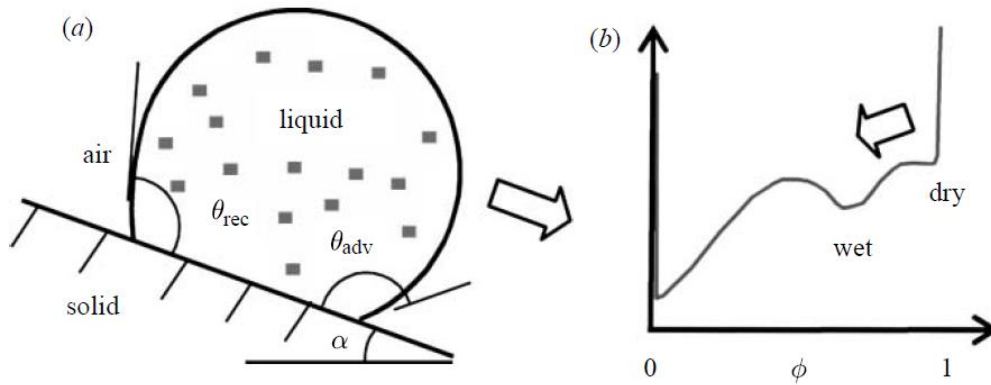


**Figure 1.6** (a) A water drop on an inclined surface. (b) As the tilt angle  $\alpha$  grows, the critical state can be reached with a disappearing energy barrier between the wetted and dry states, so that the liquid advances (Nosonovsky & Bhushan, 2009).

## 1.6. Friction-induced instabilities

Frictional sliding can lead to several types of instabilities due to the velocity dependence of the coefficient of friction, destabilization of interface elastic waves, thermal expansion and the effect of wear. As it was discussed, these instabilities can potentially result in the formation of secondary structures and leading to self-organization, e.g. in the form of a train of slip pulses that may lead to the reduction of friction. The best-known manifestation of these instabilities is ‘squealing brakes’ (Kincaid et al. 2003).

### 1.6.1. Instabilities due to velocity dependence of friction

If the coefficient of friction decreases with speed, dynamic instabilities (DI) can occur. This is because decreasing frictional resistance to sliding results in the acceleration, which leads to a higher velocity and, in turn, to even lower friction, thus creating a positive feedback loop. Various theories of velocity-dependent friction have been proposed in the literature (Adams and Nosonovsky, 2000; Rice et al., 2001).

This kind of instability can also be defined using Eq. (1.11) (Nosonovsky & Bhushan, 2009):

$$\frac{1}{2} \delta^2 \dot{S} = \delta \left( \frac{\mu W}{T} \right) \delta(V) (\delta V)^2 = \frac{W}{T} \frac{\partial \mu}{\partial V} (\delta V)^2 \geq 0 \quad (1.19)$$

Thus, if  $\frac{\partial \mu}{\partial V} \geq 0$  (the positive viscosity), the motion is stable; however, if  $\frac{\partial \mu}{\partial V} < 0$  (the ‘negative viscosity’), the motion is unstable, and secondary structures can form. The negative viscosity effect is often found in systems with dry friction. The physical meaning of this conclusion is clear: if the friction force decreases with increasing velocity, the velocity will further grow, leading to the instability (Rice & Ruina 1983; Nguyen 2003). The process will continue until it will leave the linear region and enter a limiting cycle, which is likely to be

manifested in the stick–slip motion. Such stick–slip motion can be viewed as a self-organized secondary structure.

### **1.6.2. Adams–Matrins (AMI) instabilities**

Adams (1995) and Martins (1995) showed that even for a constant value of the coefficient of friction, the steady sliding of two elastic half-planes can become dynamically unstable, even in the quasi-static limit of very small sliding velocities. In other words, frictional sliding of two elastic half-spaces can be unstable due to Adams–Matrins instabilities (AMI). The destabilization is in the form of a self-excited elastic wave at the interface between the contacting bodies. The amplitude of these waves grows exponentially with time. As the amplitude of an elastic wave grows, the frictional dissipation increases, leading to the further growth of the wave amplitude and thus creating a positive feedback loop. A similar type of instability may be observed during the sliding of rough surfaces, such as surfaces with periodic wavy profiles (Nosonovsky and Adams, 2000, 2004). Frictional instability can further lead to the formation of self-organized structures and patterns (Nosonovsky and Bhushan, 2009; Nosonovsky 2010a, b; Mortazavi and Nosonovsky, 2011).

These self-excited oscillations are confined to a region near the sliding interface and can eventually lead to either partial loss of contact or to propagating regions of stick–slip motion (slip waves). In a slip wave, a region of slip propagates along the interface, which is otherwise at the stick state. When a train of slip pulses propagates, two bodies shift relative to each other in a ‘caterpillar’ or ‘carpetlike’ motion (**Fig. 1.7**).

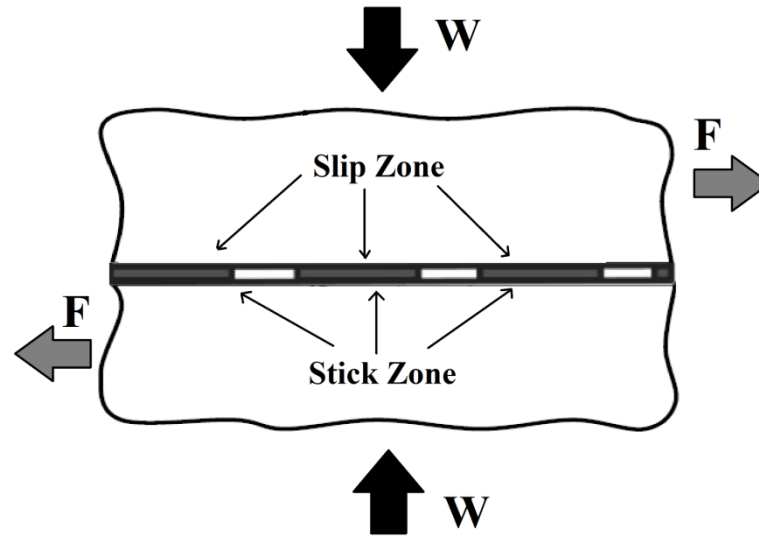


Figure 1.7. The pattern of propagating stick and slip zones can lead to friction reduction, as  $F < \mu W$

(Nosonovsky and Adams, 2001)

### 1.6.3. Thermoelastic instabilities

Another type of instability is a result of the interaction between the frictional heating, the thermoelastic distortion, and the contact pressure and it is referred to as the “thermoelastic instability” (TEI). As the interface temperature grows, the near-surface volumes of the contacting bodies expand, so the contact pressure grows as well. As a result, the friction force increases resulting in excess heat generation and the further growth of the temperature, thus creating another type of a positive feedback. The TEI leads to the formation of “hot spots” or localized high temperature regions at the interface (Barber, 1969). The TEI occurs for sliding velocities greater than a certain critical value. The coupling between the two types of instabilities constitutes the thermoelastodynamic instability (TEDI) (Aferrante et al., 2006).

#### 1.6.4. Instabilities due to wear

Another mechanism that may provide instability is the coupling between friction and wear. As friction increases, so does also the wear, which may result in an increase of the real area of contact between the bodies and in further increase of friction. The sliding bodies adjust to each other and the process is known as the self-organization during friction (Fox-Rabinovich and Totten, 2006). On the other hand, wear produces smoothening of the surface distorted by the TEI mechanism, and thus the wear and thermal expansion are competing factors, with the wear leading to stabilization of sliding and the thermal expansion leading to destabilization (Fig. 1.8).

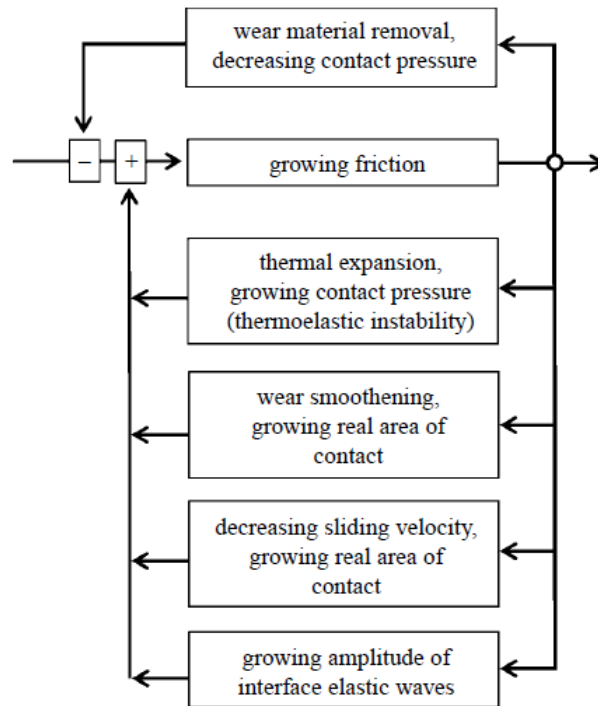


Figure 1.8. Various mechanisms can create positive or negative feedbacks that lead to instabilities during friction (Nosonovsky, 2010).

### **1.7. Motivations of this study**

As we discussed so far, the notion of friction-induced self-organization has been extensively studied in the past in relation to the fundamental concepts of irreversible thermodynamics. However, the question remains that how this notion might be successfully used for the development of advanced tribosystems and materials. As it was shown in the last sections, these fundamental concepts provide a powerful methodological tool to investigate, understand and enhance beneficial tribo-processes. These tribo-processes could result in the ability of a frictional surface to exhibit self-protection and self-healing properties. This research is dealing with the fundamental concepts that allow the possibility of the development of a new generation of tribosystem and materials that reinforce such properties, and, through them, exhibit kind of ‘adaptive’ or ‘smart’ behavior. This adaptive or smart behavior can be seen in response of the tribosystem to external mechanical, thermal, and chemical forces with a positive feedback loop that leads to minimized wear or degradation.

All problems discussed in next chapters are chosen to bridge the gap between fundamental interest in understanding the conditions leading to self-organization and practical motivation. In second chapter, we focus on instabilities originating due to the temperature dependency of coefficient of friction. Frictional instabilities may result in strong oscillations or abrupt motions, which, in turn, may be responsible for undesired noise or sever wear in engineering sliding systems. These instabilities may even to lead to catastrophic destruction and losses in mechanical systems.

One area in which impact of these instabilities can be seen is design of aircraft disk brakes. These brakes are designed to dissipate very large amounts of energy in order to stop the plane within a short time after an aircraft touches the runway. Large amounts of heat are generated in

aircraft disk brakes within seconds, resulting in high temperatures as well as very high temperature gradients. The disks should be made of a material which is light, wear-resistant, and able to absorb huge amounts of heat without melting or breaking.

The other problem we give especial attention in this research to is running-in. After the start of sliding contact between fresh, unworn solid surfaces, changes in friction, temperature, and rate of wear are commonly observed. These temporary fluctuations are sometimes ignored or simply accepted as the normal course of operation. However, for improving the performance of components such as bearings, gears, and seals, it can be beneficial to ensure that running-in is conducted in an optimized way. A common example is the running-in of replacement brake linings on vehicles. This is done both to ensure proper mating of the lining with the counterface and to form a uniform transfer layer on the counterface that promotes even stopping torque (Blau, 2005).

Furthermore, in addition to a fundamental interest in understanding the conditions leading to self-organized patterns, a practical motivation is that the unique microstructures stabilized by self-organization reactions often result in modifications of the properties of these materials, and in particular, their mechanical properties. These modifications can either be detrimental or beneficial to the performances of these materials. Hence, a better understanding and control of self-organization reactions, and patterns formed due to them, may thus provide a path for improving materials performances.

Finally, we focus on modeling of the solid-liquid energy dissipation. In the last decade, material scientists have given attention to surfaces that are non-wetting, non-sticky, antifouling, ice-phobic, and self-cleaning. In order to reach optimized design, synthesis and characterization of such surfaces, different analytical and numerical models of wetting of rough surfaces have



been developed. However, better understanding of solid-liquid energy dissipation and its manifestation, i.e., contact angle (CA) hysteresis can improve current status of design of self-cleaning materials.

This research describes how to utilize fundamental concepts for specific engineering applications. The main theme of this research is the application of concept of self-organization to tribology and the role played by physical and chemical interactions in modifying and controlling friction and wear. This topic is becoming increasingly important with the current drive for increased productivity, often under conditions in which a lubricant cannot be used (such as dry machining conditions), that characterizes modern trends for different tribological applications.

### **1.8. Objectives of this study**

In this chapter, we discussed how self-organizing behavior might take place in certain situations at the frictional interface. We also reviewed recent studies combining the mechanical and thermodynamic methods in tribology and thus extending the field of mechanical friction-induced vibrations to non-mechanical instabilities and self-organizing processes. In next chapters, we will investigate practical engineering cases that would lead to self-organization. In next chapters, we will focus on some different practical tribological problems and investigate instabilities and/or self-organization in each. We can summarize our objectives in this study as in the following:

1. To investigate instabilities due to the temperature-dependency of the coefficient of friction. While most of studies on the thermoelastic instability investigate the positive feedback that forms with friction and heat generation during slide of the elastic materials and may lead to instabilities, they ignored the temperature-dependency of the coefficient of friction. This temperature-dependency can have a significant effect

- on the stability, by leading to formation of hot and cold spots on the disks. We will formulate a stability criterion and perform a case study of a brake disk. It is our hypothesis that the mechanism of instability can contribute to poor reproducibility of aircraft disk brake tests reported in the literature. Finally, a method to increase the reproducibility should be based on the results of this study.
2. To study frictional running-in as a friction-induced self-organization process. Running-in is a very common tribological phenomenon. It is defined as a transient stage on the onset of the frictional sliding, in which friction and wear decrease to their stationary values. We will introduce a theoretical model of running-in and investigate rough profile evolution. We will compare our modeling results with experimental observations. Moreover, we will develop a mathematical criterion for orderliness and self-organization of a rough surface profile.
  3. To investigate the possibility of pattern formation during friction. There are different type of patterns can form at the sliding interface due to the mass transfer (diffusion), heat transfer, various tribochemical reactions, and wear. We will study the possibility of Turing-type patterns in frictional interface. Turing or reaction-diffusion systems describe variations of spatial concentrations of chemical components with time due to local chemical reactions coupled with diffusion. We will present mathematical modeling, and will compare our mathematical findings with existing experimental data.
  4. To investigate how interfacial patterns including propagating trains of stick and slip zones formed due to dynamic sliding instabilities can be categorized as

self-organized patterns. By treating stick and slip as two phases at the interface, we will study the effects related to such phase transitions.

5. To study contact angle (CA) hysteresis as an example of solid-liquid energy dissipation. We will use Cellular Potts Model to simulate CA hysteresis for a droplet over the tilted patterned surface, and a bubble placed under the surface immersed in liquid. We will discuss dependency of CA hysteresis on the surface structure and other parameters.

## **Chapter 2**

### **Stability of Frictional Sliding with the Coefficient of Friction depended on the Temperature**

#### **2.1. Objective**

Different type of instabilities was discussed in Section 1.6. This chapter investigates another type of instability due to the temperature-dependency of the coefficient of friction. There are many studies of the so-called frictional thermoelastic instability which investigate extensively the positive feedback that forms with friction and heat generation during slide of the elastic materials and may lead to instabilities. However, these studies ignored the temperature-dependency of the coefficient of friction. This temperature-dependency can have a significant effect on the frictional sliding stability, by leading to the formation of “hot” and “cold” spots on the contacting surfaces. We will formulate a stability criterion and perform a case study of a brake disk. We will discuss how the mechanism of instability can contribute to poor reproducibility of aircraft disk brake tests reported in the literature. Furthermore, a method to increase the reproducibility by dividing the disk into several sectors with decreased thermal conductivity between the sectors will be discussed.

#### **2.2. Background**

One area where frictional instabilities are particularly important is the design of disk brakes. Frictional instabilities in car disk brakes have been an object of investigation mostly because of the disk brake squeal (Lee and Barber, 1993; Kincaid et al., 2003; Paliwal et al., 2003). Aircraft disk brakes often have a similar construction to car disk brakes; however, the instability

constitutes even more crucial problem for the aircraft brakes. Aircraft disk brakes are designed to dissipate very large amounts of energy in order to stop the plane within a short time after an aircraft touches the runway. Large amounts of heat are generated in aircraft disk brakes within seconds, resulting in high temperatures as well as very high temperature gradients. The disks should be made of a material which is light, wear-resistant, and able to absorb huge amounts of heat without melting or breaking. In brief, the brake materials should have good heat sinking ability in order to minimize the interface temperature at the braking surface arising out of frictional heat (Venkataraman and Sundararajan, 2002). The materials that provide a compromise between weight, strength and heat transfer are the carbon-carbon (CC) composites (Stimson and Fisher, 1980; Byrne, 2004). A number of studies have been conducted in the past decade to investigate the tribological performance of the CC composite disk brake material at various sliding velocities, temperatures and levels of humidity (Gomes et al., 2001; Luo et al., 2004; Yuan et al., 2005; Kasem et al., 2007). Venkataraman and Sundararajan (2002) showed that CC composites exhibit a transition from a low coefficient of friction during the “normal” wear regime, to a high coefficient of friction during the “dusting” wear regime, when the normal pressure times the sliding velocity exceeds a critical value. The transition is associated with the attainment of a critical temperature at the interface between the two CC composite bodies sliding against each other. Yen and Ishihara (1994) showed that two types of surface morphology can be distinguished on the sample surface and argued that the TEI is responsible for this effect.

Most theoretical studies of the instabilities have concentrated on investigating the onset of the instability and stability criteria. However, the quantitative study of the unstable motion is also of great practical importance. Due to various safety requirements, the aircraft brake disks should demonstrate highly reproducible performance. However, the instability of frictional

sliding between a disk brake and a pad may result in the high sensitivity of the tribological system to initial random perturbations. As a result, the time and distance required to stop a plane may vary significantly even under the same conditions (such as the mass and initial velocity of the plane).

### 2.3. Mathematical modeling

Most of current models of friction-induced instabilities ignore the temperature-dependency of the coefficient of friction. These models usually assume that either elastodynamic or thermoelastic s can give rise to friction-induced instabilities and vibrations. The time-scales of these effects differ considerably, so it is usual to neglect the coupling between them, i.e. to neglect the thermal effects in elastodynamic analyses and to use the quasi-static approximation in thermoelastic analyses. In addition, these models assume that the coefficient of friction is constant, i.e. not varying with temperature.

On the other hand, there is experimental evidence that CC composites undergo a transition from a low to a high value of the coefficient of friction depending on the temperature change (Venkataraman and Sundararajan, 2002; Filip, 2002; Roubicek, et al. 2008). Here we investigate the possibility that the temperature-dependency of the coefficient of friction leads to instability.

First, we consider the 1D heat conduction equation in rectangular coordinates with a heat generation source resulted from friction, in a slab of length  $L$ . We assume that the 1D region represents a 2D slab with a small thickness  $w$ , so that the heat propagates instantly throughout the thickness and a 1D approximation is valid.

$$\begin{aligned} \frac{\partial^2 T(x,t)}{\partial x^2} + \frac{1}{wk} g(x,t) &= \frac{1}{\alpha} \frac{\partial T(x,t)}{\partial t} & \text{in} & \quad 0 < x < L, \quad t > 0 \\ -k \frac{\partial T}{\partial x} + h(T - T_0) &= 0 & \text{at} & \quad x = 0, \quad t > 0 \end{aligned} \quad (2.1)$$

$$k \frac{\partial T}{\partial x} + h(T - T_0) = 0 \quad \text{at} \quad x = L, t > 0$$

$$T(x, 0) = F(x) \quad \text{for} \quad 0 \leq x \leq L, t=0$$

where  $T(x, t)$  is the temperature,  $x$  and  $t$  are the spatial coordinate and time, and  $k$  and  $\alpha$  are the thermal conductivity and diffusivity, respectively and  $h$  is the coefficient of convective heat transfer. We assume that the slab is initially at a temperature  $F(x)$  and, for times  $t > 0$ , it dissipates heat into the environment with constant temperature  $T_0$ .

The heat generation term due to friction is given by

$$g(x, t) = PV\mu \quad (2.2)$$

where  $P$  is pressure,  $V$  is sliding velocity, and  $\mu$  is the coefficient of friction which we assume to be linearly temperature-dependent

$$\mu = \mu_0[1 + \lambda(T - T_0)] \quad (2.3)$$

where  $\lambda$  is the constant of proportionality.

It is convenient to consider Eq. 1 in the non-dimensional form by defining dimensionless parameters

$$\theta(X, \tau) = \frac{T - T_0}{T_0}, \quad \tau = \frac{t\alpha}{L^2}, \quad X = \frac{x}{L}, \quad G = \left(\frac{PVL^2}{wk}\right) \left(\frac{\mu_0}{T_0}\right), \quad H = \frac{Lh}{k}, \quad \epsilon = \lambda T_0 \quad (2.4)$$

Eq. (2.1) becomes

$$\frac{\partial^2 \theta}{\partial X^2} + G(1 + \epsilon\theta) = \frac{\partial \theta}{\partial \tau} \quad \text{in} \quad 0 < X < 1, \tau > 0 \quad (2.5)$$

$$-\frac{\partial \theta}{\partial X} + H\theta = 0 \quad \text{at} \quad X = 0, \tau > 0$$

$$\frac{\partial \theta}{\partial X} + H\theta = 0 \quad \text{at} \quad X = 1, \tau > 0$$

$$\theta(X, 0) = f(X) \quad \text{for} \quad 0 \leq X \leq 1, \tau = 0$$

The non-homogeneous term  $G\epsilon\theta$  in Eq. (2.5) is due to the non-dimensional parameter  $\epsilon$ , which defines the temperature-dependency of the coefficient of friction. Eq. (2.5) has a steady solution

$\theta_s(x)$ . We investigate the stability of this steady state by considering the possibility that a small perturbation in the temperature can grow with time. Thus, we write

$$\theta(X, \tau) = \theta_s(X) + \tilde{\theta}(X, \tau) \quad (2.6)$$

where  $\tilde{\theta}(X, \tau)$  is the perturbation. Now substituting the Eq. (2.6) into the Eq. (2.5)

$$\frac{\partial^2 \tilde{\theta}}{\partial X^2} + G\epsilon \tilde{\theta} = \frac{\partial \tilde{\theta}}{\partial \tau} \quad \text{in} \quad 0 < X < 1, \tau > 0 \quad (2.7)$$

$$-\frac{\partial \tilde{\theta}}{\partial X} + H\tilde{\theta} = 0 \quad \text{at} \quad X = 0, \tau > 0$$

$$\frac{\partial \tilde{\theta}}{\partial X} + H\tilde{\theta} = 0 \quad \text{at} \quad X = 1, \tau > 0$$

$$\tilde{\theta}(X, \tau) = \tilde{f}(X) \quad \text{for} \quad 0 \leq X \leq 1, \tau = 0$$

We express solution of Eq. (2.7) as a sum of normal modes, each of which has the general form

$$\tilde{\theta}(X, \tau) = \psi(X)e^{S\tau} \quad (2.8)$$

where  $S$  is a constant. Substituting Eq. (2.8) into Eq. (2.7) we get

$$\frac{d^2 \psi}{dX^2} + (G\epsilon - S)\psi = 0 \quad \text{in} \quad 0 < X < 1 \quad (2.9)$$

$$-\frac{d\psi}{dX} + H\psi = 0 \quad \text{at} \quad X = 0$$

$$\frac{d\psi}{dX} + H\psi = 0 \quad \text{at} \quad X = 1$$

Solution of Eq. (2.9) is in the form of

$$\psi(X) = C_1 \sin(m\pi X) + C_2 \cos(m\pi X) \quad (2.10)$$

where  $C_1$  and  $C_2$  are two constants which can be obtained from the boundary conditions and  $m$  is a natural number. Substituting Eq. (2.10) into Eq. (2.9), we get

$$S = G\epsilon - (m\pi)^2 \quad (2.11)$$

We conclude from Eq. (2.8) that the stability of a small perturbation depends on whether the exponential term grows or decays with time  $\tau$ , which, in turn, depends upon the sign of  $S$  for any



$m$ . Thus, from Eq. (2.11), decaying in any  $m$ -th mode is observed for  $G\epsilon < (m\pi)^2$ . Since  $m$  is increasing, the stability condition should be satisfied for the first term  $G\epsilon < \pi^2$ . In the case of  $\epsilon = 0$ , i.e. when there is no temperature-dependency of the coefficient of friction, and, with increasing time,  $\theta(X, \tau)$  will approach the steady temperature distribution,  $\theta_s(X)$ . However, in the case of  $\epsilon \neq 0$ , the stability condition requires

$$\epsilon < \pi^2 \left( \frac{wk}{PVL^2} \right) \left( \frac{T_0}{\mu_0} \right) \quad (2.12)$$

Let's call  $\epsilon_{critical} = \pi^2 \left( \frac{wk}{PVL^2} \right) \left( \frac{T_0}{\mu_0} \right)$  and we conclude that if  $\epsilon > \epsilon_{critical}$ , the solution is unstable. Note that  $\epsilon_{critical}$  depends on the geometry ( $L$ ), pressure ( $P$ ) and sliding velocity ( $V$ ) in our system. This is in agreement with the experimental report by Venkataraman and Sundararajan (2002), who found that there were different regimes of the temperature-dependency of the coefficient of friction and that these three parameters had considerable influence on the regimes.

Note also that for the negative  $\epsilon < 0$ , the stability condition is always satisfied. That means that if the coefficient of friction decreases with temperature, there is no unstable behavior. This is because the instability is caused by the positive feedback between the coefficient of friction and temperature, i.e, a small positive local fluctuation of temperature would cause a local increase of the coefficient of friction, which, in turn, would cause further growth of temperature. When the feedback is negative ( $\epsilon < 0$  and, therefore  $\lambda < 0$ ) this type of unstable behavior does not occur.

To find the exact solution of Eq. (2.5), one can use the transformation

$$\theta(X, \tau) = \psi(X, \tau)e^{G\epsilon\tau} \quad (2.13)$$

which yields, on substituting

$$\frac{\partial^2 \psi}{\partial X^2} + G e^{G\epsilon\tau} = \frac{\partial \psi}{\partial \tau} \quad \text{in} \quad 0 < X < 1, \tau > 0 \quad (2.14)$$

$$-\frac{\partial \psi}{\partial X} + H\psi = 0 \quad \text{at} \quad X = 0, \tau > 0$$

$$\frac{\partial \psi}{\partial X} + H\psi = 0 \quad \text{at} \quad X = 1, \tau > 0$$

$$\psi(X, 0) = f(X) \quad \text{for} \quad 0 \leq X \leq 1, \tau = 0$$

Eq. (2.14) can be solved analytically, using first, the method of the separation of variables and then the Green's function (Özışık, 1993). First, we find the solution of the homogeneous equation without the term  $G \exp(G\epsilon\tau)$

$$\psi'(X, \tau) = 2 \sum_{m=1}^{\infty} e^{-(m\pi)^2 \tau} \sin(m\pi X) \left( \int_{X'=0}^1 \sin(m\pi X') f(X') dX' \right) \quad (2.15)$$

Here we assumed that the both sides of the slab are kept at the constant temperature  $T_0$ , i.e.,  $\psi(0, \tau) = \psi(1, \tau) = 0$  and  $H \rightarrow \infty$ . This assumption simplifies the solution without affecting the stability analysis, since the stability is governed by the exponential term of the solution which is not affected by the boundary conditions.

The solution of the homogeneous equation can be written in terms of Green's function (Özışık, 1993)

$$\psi'(X, \tau) = \int_{X'=0}^1 \gamma(X, \tau; X', \tau' = 0) f(X') dX' \quad (2.16)$$

Comparing Eq. (16) with Eq. (2.15), we construct the Green's function by replacing  $\tau$  by  $\tau - \tau'$

$$\gamma(X, \tau; X', \tau') = 2 \sum_{m=1}^{\infty} e^{-(m\pi)^2 (\tau - \tau')} \sin(m\pi X) \sin(m\pi X') \quad (2.17)$$

where  $X'$  and  $\tau'$  are integration parameters. Then, the solution of the non-homogeneous problem is given in terms of the Green's function

$$\psi(X, \tau) = \psi'(X, \tau) + \int_{\tau'=0}^{\tau} d\tau' \int_{X'=0}^1 G \exp^{G\epsilon\tau} \gamma(X, \tau - \tau', X', ) dX' \quad (2.18)$$

Substituting Eq. (2.17) into Eq. (2.18) yields the solution of Eq. (2.14)

$$\begin{aligned}
\psi(X, \tau) = & \\
& 2 \sum_{m=1}^{\infty} e^{-(m\pi)^2 \tau} \sin(m\pi X) \left( \int_{X'=0}^1 \sin(m\pi X') f(X') dX' \right) + \\
& 2 \sum_{m=1}^{\infty} \frac{G}{(m\pi)^2 - G\epsilon} e^{-G\epsilon \tau} \sin(m\pi X) X (1 - \cos(m\pi)) \quad \text{for } 0 < X < 1
\end{aligned} \tag{2.19}$$

Finally, substituting Eq. (2.18) into Eq. (2.13), we find the solution of Eq. (2.5)

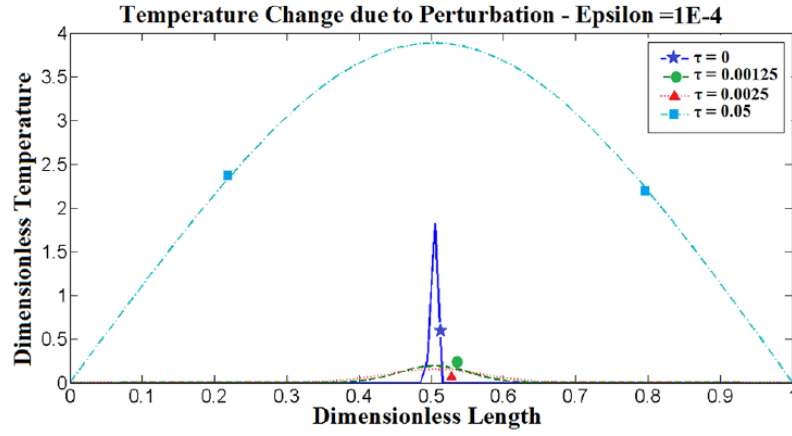
$$\begin{aligned}
\theta(X, \tau) = & \\
& 2 \sum_{m=1}^{\infty} e^{(G\epsilon - (m\pi)^2) \tau} \sin(m\pi X) \left( \int_{X'=0}^1 \sin(m\pi X') f(X') dX' \right) + \\
& 2 \sum_{m=1}^{\infty} \frac{G}{(m\pi)^2 - G\epsilon} \sin(m\pi X) (1 - \cos(m\pi)) \quad \text{for } 0 < X < 1
\end{aligned} \tag{2.20}$$

The stability of a small perturbation of the solution given by Eq. (2.19) is governed by Eq. (2.12). This can be observed directly from Eq. (2.19) noting that the stability depends on whether the exponential term grows or decays with time  $\tau$ , which, in turn, depends upon whether  $G\epsilon - (m\pi)^2 < 0$  for any  $m$  and should be satisfied for the first term  $G\epsilon < \pi^2$  as it was explained above.

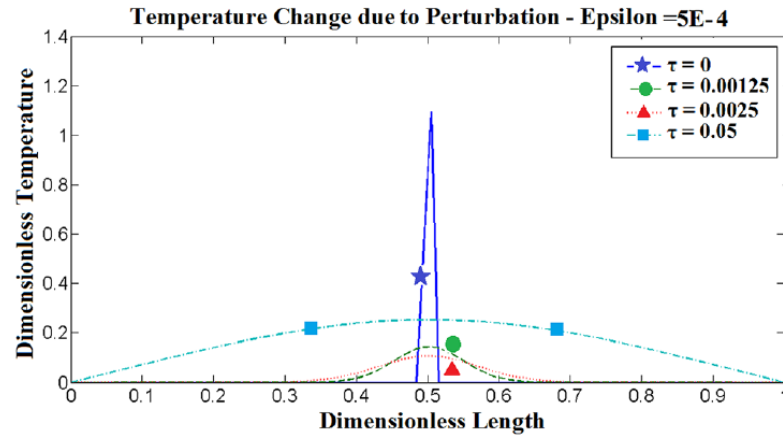
To examine stability condition (Eq. 2.12), numerical results for solution of Eq. (2.7) is presented in **Figure 2.1**. The simulation was performed using the Matlab software package. In order to investigate the evolution of a localized hot/cold spot, we introduced a small random perturbation imposed over a constant temperature field and confined between  $0.49 < X < 0.51$ , i.e., at the center of the domain. The perturbation was a random function built by assigning random numbers with the amplitude between 0 and 2 to the values in  $0.49 < X < 0.51$  and zero otherwise. Spatial and temporal step size for the numerical simulation was 0.01 and 0.005, respectively. **Figure 2.1** shows the response of the system to small perturbation for different values of  $\epsilon$  (0.0001, 0.00005 and 0.00001). Transient temperature is presented for four different values of the dimensionless time (0, 0.00125, 0.0025, 0.05). The parameters of Eq. (2.12) were

chosen according to the experimental values reported in the literature on CC composites in disk brakes (for example Zhao et al., 2007):  $P = 1 \text{ MPa}$ ,  $k = 50 \text{ W/mK}$ ,  $L = 0.5 \text{ m}$ ,  $V = 1000 \text{ m/s}$ . These values correspond to  $\epsilon_{critical} = 3.88 \times 10^{-5}$ . It is observed from **Fig. 2.1** that the solution grew unboundedly in the first two cases corresponding to  $\epsilon > \epsilon_{critical}$  and decayed in the third case  $< \epsilon_{critical}$  in agreement with the stability criterion of Eq. (2.12).

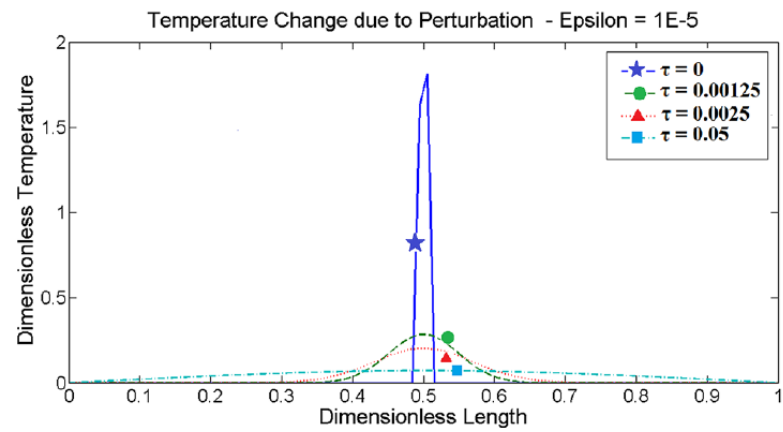
We found in this section that when the temperature dependency of the coefficient of friction is introduced, the solution for the temperature field is unstable for  $\epsilon > \epsilon_{critical}$ . The comparison with experimental data shows that in practical cases the value of  $\epsilon$  is comparable with  $\epsilon_{critical}$  (Zhao et al., 2007). Therefore, the effect of the temperature dependency of the coefficient of friction should be taken into account when the stability of the frictional sliding with heat generation is analyzed. Although a rectangular slab was studied in this section, a similar effect is expected with a circular disk, as it will be discussed below.



(a)



(b)



(c)

Figure 2.1. Response of the system to different values of values of  $\epsilon$ : (a) 0.0001, (b) 0.00005 and (c) 0.00001.  $\tau$

is the dimensionless time (Mortazavi et al., 2012).

## 2.4. Reproducibility of disk brake test results

In this section we present a model for an aircraft or car disk brake in contact with a pad with a temperature-dependent coefficient of friction between them and show that frictional instabilities affect the reproducibility of brake test results, e.g., the time needed to stop the car or aircraft.

### 2.4.1. Numerical Model

Let us consider a rigid brake disk with the outer and inner radii of  $R_{out}$  and  $R_{in}$  in contact with a rigid pad pressed together by the pressure  $P$  (**Fig. 2.2**). The torque created by the disk is

$$M = \int_{r=R_{in}}^{R_{out}} 2\pi r^2 \mu_m P dr = \frac{2}{3} \pi \mu_m P (R_{out}^3 - R_{in}^3) \quad (2.21)$$

where  $\mu_m$  is the mean coefficient of friction throughout the entire disk surface. The aircraft or car brake is usually equipped with  $n$  disks, so the force that decelerates the aircraft or car is given by

$$F = nC \frac{M}{R_{out}} = \frac{2}{3R_{out}} nC \pi \mu_m P (R_{out}^3 - R_{in}^3) \quad (2.22)$$

where  $C$  is a non-dimensional coefficient dependent on the radii of the disks and pads. In Eq. (2.22), it is assumed that the pad radius and brake radius are identical. For an aircraft or vehicle of mass  $m$  and initial velocity  $V$ , the time required to stop is given by

$$t = \frac{Vm}{F} = \frac{3VmR_{out}}{2nC\pi\mu_m P (R_{out}^3 - R_{in}^3)} \quad (2.23)$$

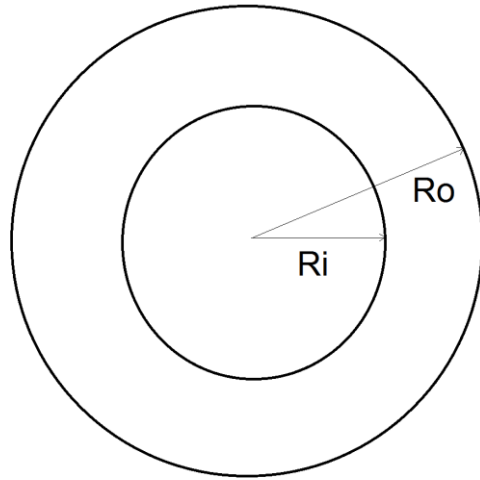


**Figure 2.2. Schematic of a brake disk (Mortazavi et al., 2012)**

Let us assume now that the coefficient of friction depends on temperature as described by Eq. (2.3), and  $T_m$  is mean temperature at a certain time during transient stage so that  $\mu_m = \mu(T_m)$ . We assume a simple linear dependency given by Eq. (2.3) within a certain domain between the minimum and the maximum temperatures, so that the range of the coefficient of friction is  $\mu_{min} < \mu(T) < \mu_{max}$  (**Fig. 2.3**).

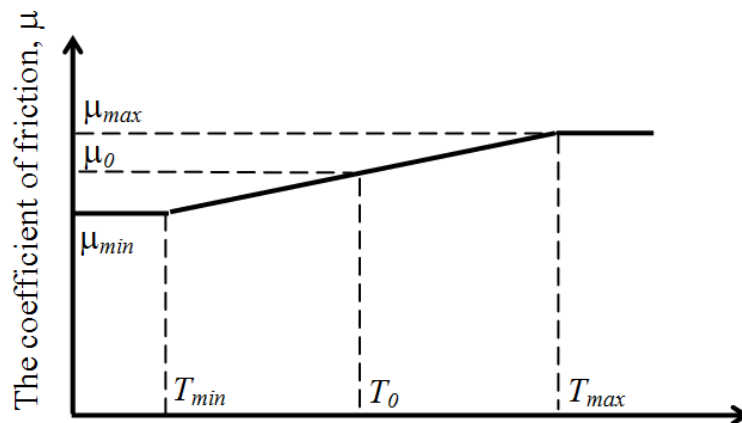


**Figure 2.3 Temperature-dependence of the coefficient of friction (Mortazavi et al., 2012)**

The time required to stop the aircraft is now in the range  $t_{\min} < t < t_{\max}$ , with corresponding values calculated from Eq. (2.23)

$$t_{\min} = \frac{3VmR_{out}}{2nC\pi\mu_{\max}P(R_{out}^3 - R_{in}^3)}$$

$$t_{\max} = \frac{3VmR_{out}}{2nC\pi\mu_{\min}P(R_{out}^3 - R_{in}^3)} \quad (2.24)$$

Most of the mechanical energy is converted into heat. The temperature field at the interface should satisfy the heat conduction equation, which is written here in polar coordinates

$$\frac{1}{r} \frac{\partial}{\partial r} \left( r \frac{\partial T}{\partial r} \right) + \frac{1}{r^2} \frac{\partial^2 T}{\partial \phi^2} + \frac{1}{wk} g(T) = \frac{1}{\alpha} \frac{\partial T}{\partial t}$$

$$g(T) = \mu \text{Pr} \omega \quad (2.25)$$

Stability of the solution of Eq. (2.17) should be analyzed now.

#### 2.4.2. Stability analysis

As discussed in the preceding sections, a small perturbation in the temperature field distribution (an elevated or reduced temperature) can grow unboundedly if the solution is unstable. The stability can depend on the sign of  $\lambda$  in Eq. (2.3). For  $\lambda > 0$ , the coefficient of friction will grow with temperature, and additional heat will be generated leading to a further increase of  $\mu$ . The heat will also be conducted to neighboring points, so the coefficient of friction at those points will grow as well, and the unstable behavior with a growing size of the “hot spot” will be observed. For  $\lambda < 0$ , quite oppositely, friction will decrease and the temperature will eventually drop to the steady-state level. In practical conditions, the coefficient of friction can either grow or decrease with temperature. Thus, Roubicek et al. (2008) observed that the coefficient of friction decreased with increasing temperature during the SAE J2430 friction test which is frequently used in the USA for evaluating the brake performance. This is attributed to physical and chemical changes in the friction layer which forms on the friction surface (Filip,



2002). As it was mentioned earlier, Venkataraman and Sundararajan (2002) found that the dependency of the coefficient of friction varied within different working ranges of the sliding velocity and load. We will concentrate on the potentially unstable case of  $\lambda > 0$ .

In the case of unstable behavior, any small perturbation grows and the maximum value of the coefficient of friction,  $\mu_{max}$  (in the case of a positive perturbation), or its minimum value,  $\mu_{min}$  (in the case of a negative perturbation) will be reached within a short time. Furthermore, the hot spot will spread to neighboring regions of the surface. The area of the hot spot can be estimated as the thermal diffusivity times time  $t\alpha$ . Since the perturbation can be either positive or negative, the disk area will be divided into  $N$  domains of either the maximum or minimum coefficient of friction. The number of domains can be estimated by dividing the total area by the size of the region of perturbation

$$N = \frac{n\pi(R_{out}^2 - R_{in}^2)}{t\alpha} \quad (2.26)$$

The probability distribution function for a large number of trials of equal probability (e.g., coin flips) is given by the normal distribution

$$p(x) = \frac{1}{\sqrt{2\pi}\sigma} \exp\left(-\frac{(x - \mu_{mean})^2}{2\sigma^2}\right) \quad (2.27)$$

where  $\sigma$  is the standard deviation and  $\mu_{mean} = (\mu_{max} + \mu_{min})/2$  is the mean value. The value of  $\sigma$  is given by

$$\sigma = \frac{(t_{max} - t_{min})}{N} \sqrt{\frac{N}{4}} = (t_{max} - t_{min}) \sqrt{\frac{t\alpha}{4n\pi(R_{out}^2 - R_{in}^2)}} \quad (2.28)$$

in which  $t$  is defined by Eq. (2.23)

$$\sigma = \frac{(t_{max} - t_{min})}{2n\pi} \sqrt{\frac{3Vm\alpha R_{out}}{2C\mu_m P(R_{out}^2 - R_{in}^2)(R_{out}^3 - R_{in}^3)}} \quad (2.29)$$

For the reproducibility of the results, it is desirable that the standard deviation is as small as possible (**Fig. 2.4**). One possible way to decrease  $\sigma$  is to decrease the thermal diffusivity  $\alpha$  or to increase the total working disk area  $n\pi(R_{out}^2 - R_{in}^2)$  and the frictional traction  $\mu_m P$ . Another approach to increase the reproducibility may be texturing the disk surface so that it is artificially divided into a significant number  $N$  of domains.

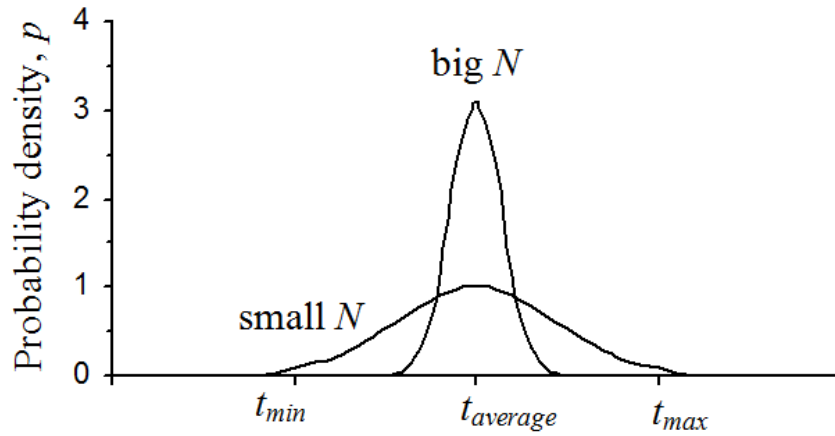


Figure 2.4. Effect of the number of domains,  $N$ , on the reproducibility of the brake test

### 2.4.3. Results and discussion

The heat conduction equation in polar coordinates (Eq. 16) is written in the dimensionless form

$$\frac{1}{r^*} \frac{\partial}{\partial r^*} \left( r^* \frac{\partial \theta}{\partial r^*} \right) + \frac{1}{r^{*2}} \frac{\partial^2 \theta}{\partial \phi^{*2}} + G(1 + \varepsilon \theta) = \frac{\partial \theta}{\partial \tau} \quad (2.30)$$

where  $r^*$  and  $\phi^*$  are the dimensionless radius and angle, respectively. Moreover, we assume that the coefficient of friction depends linearly on temperature, and that the values of temperature are limited by  $T_{min} < T < T_{max}$ . A small perturbation of the steady solution  $\theta_s(r^*, \phi^*)$  of Eq. (30) is given by

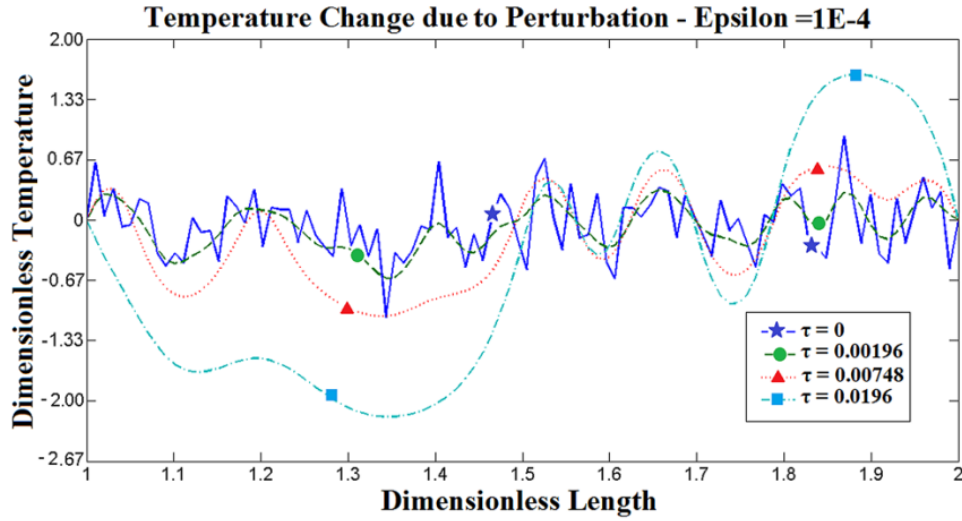
$$\theta(r^*, \phi^*, \tau) = \theta_s(r^*, \phi^*) + \tilde{\theta}(r^*, \phi^*, \tau) \quad (2.31)$$

where  $\tilde{\theta}(r^*, \phi^*, \tau)$  is the small perturbation of the dimensionless temperature. Substituting Eq. (23) in Eq. (22) yields

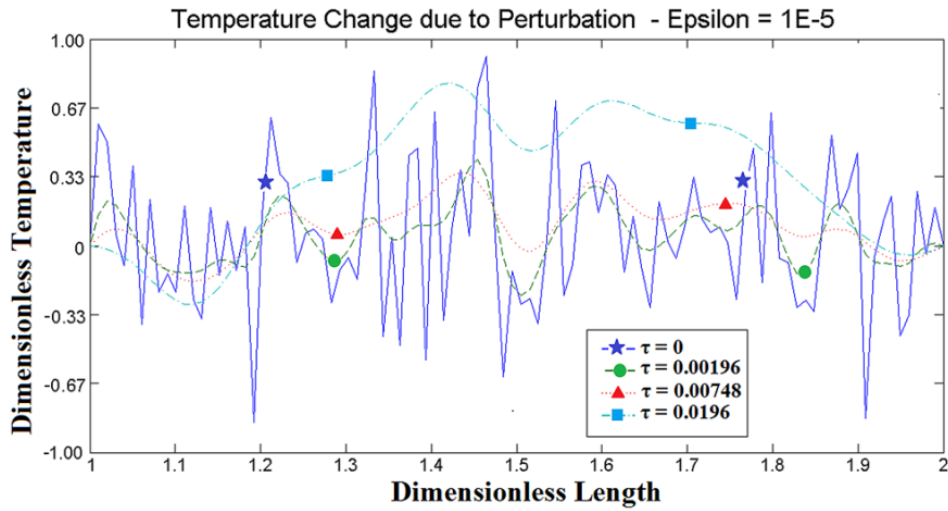
$$\frac{1}{r^*} \frac{\partial}{\partial r^*} (r^* \frac{\partial \tilde{\theta}}{\partial r^*}) + \frac{1}{r^{*2}} \frac{\partial^2 \tilde{\theta}}{\partial \phi^{*2}} + G\epsilon \tilde{\theta} = \frac{\partial \tilde{\theta}}{\partial \tau} \quad (2.32)$$

The feedback loop is created due to the coupling of the temperature and the coefficient of friction, and response of system to onset of perturbation in whole domain is shown in **Fig. 2.5**. The results are presented for following parameters:  $P = 1 \text{ MP}$ ,  $k = 50 \text{ W/mK}$ ,  $R_{in} = 1 \text{ m}$ ,  $R_{out} = 2 \text{ m}$ ,  $n = 2000 \text{ rpm}$ . **Fig. 2.5** clearly shows how value of  $\epsilon$  affects growing or decaying instabilities caused by perturbation in whole domain.

Then we focus our attention to reproducibility of test results. **Fig. 2.6** and **Fig. 2.7** compare the results of response of system in two different cases, respectively: first for rigid brake, and then for a brake with divided to different sectors. For simplicity, we present data in these two figures assuming  $\theta = \theta(\phi^*, \tau)$ . A random initial perturbation at every point of the disk results in initially positive perturbations tend to propagate and grow into the positive area, while initially negative perturbation tend to propagate and grow into the negative area (**Fig. 2.6a**). As a result, the disk surface after 1000 time steps of simulation was divided into several domains with the maximum and minimum values of temperature. The average value of the friction force was calculated by averaging the coefficient of friction at the entire disk and then by all time steps. The simulation was run 100 times and a histogram showing a probability distribution of the average  $\mu$  was produced (**Fig. 2.6b**).



(a)

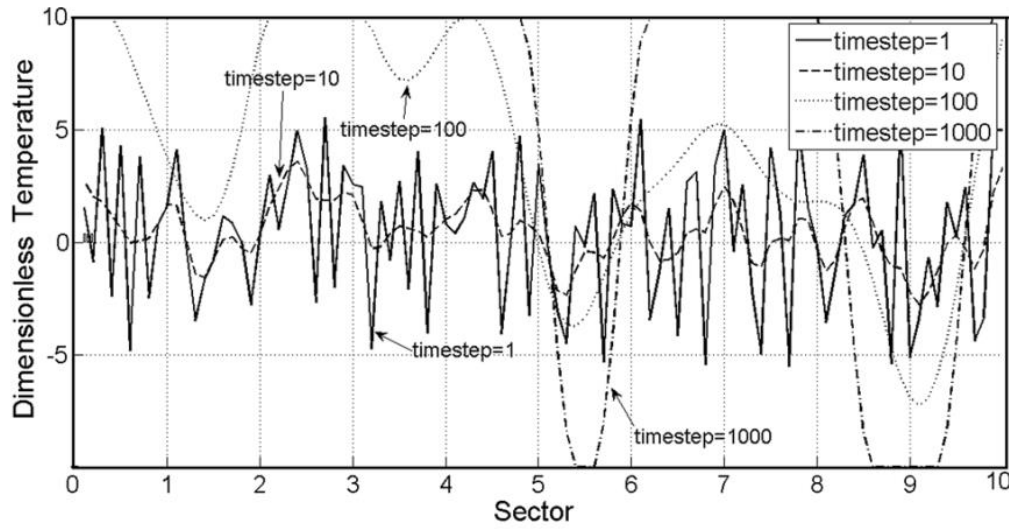


(b)

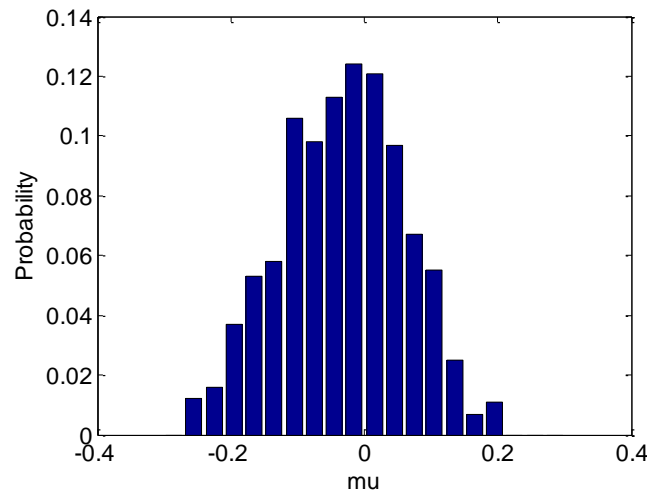
**Figure 2.5. Response of system to perturbation in whole domain for different values of  $\epsilon$ : (a) 0.0001, (b) 0.00001.  $\tau$  is the dimensionless time (Mortazavi et al., 2012)**

After that, it was assumed that the disk was divided into 10 sectors in  $\phi$  direction with zero thermal conductivity between the sectors. The same simulations were run and the results are shown in **Fig. 2.7**. It is observed that a random initial perturbation at any point results in the formation of a number of domains (identical with the sectors) with maximum or minimum temperature (**Fig. 2.7a**). Again, the histogram showing the average value of the average  $\mu$  was

produced on the basis of 100 simulation (**Fig. 2.7b**). The results show that the deviation of the average  $\mu$  is much lower in this case (namely, the variance  $\sigma^2=0.0027$ ) that in the first case ( $\sigma^2=0.0086$ ), which is understandable, since due to the insulation of the sectors the instability cannot propagate throughout the entire area of the disk. It is therefore, suggested that texturing the disk or dividing it into sectors can increase the reproducibility of the results.

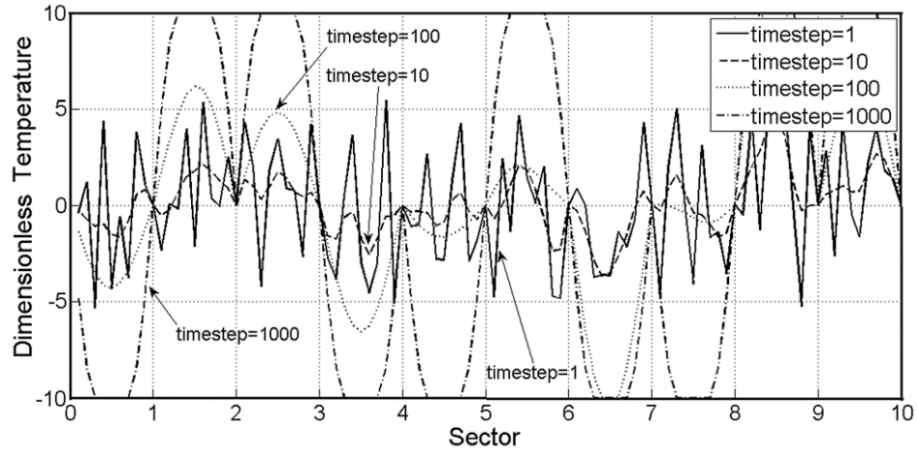


(a)

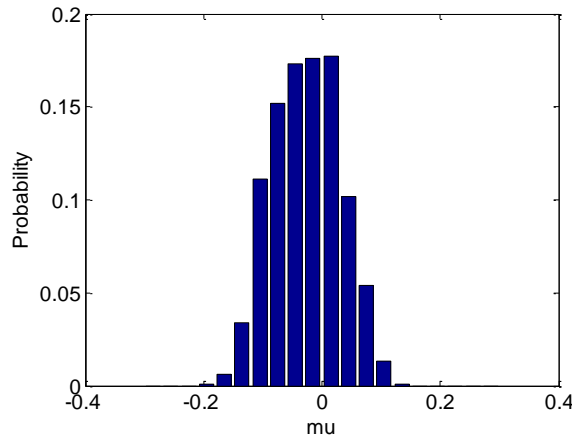


(b)

**Figure 2.6. Simulation results for  $T$  at 1, 10, 100, and 1000 timesteps (a) random fluctuation (b) distribution of the average value of the coefficient of friction after 100 runs (Mortazavi et al., 2012)**



(a)



(b)

**Figure 2.7. Simulation results for  $T$  at 1, 10, 100, and 1000 timesteps (a) random fluctuation (b) distribution of the average value of the coefficient of friction after 100 runs (Mortazavi et al., 2012)**

## 2.5. Conclusion

In this chapter, we studied the stability of frictional sliding with the temperature-dependent coefficient of friction. Although this temperature-dependency is usually ignored in most disk-pad contact models, we showed that it can have a significant effect on the stability. We presented a mathematical model and formulated the stability condition governing whether the perturbations imposed on the surface temperature in the frictional sliding can grow or decay. Our results

demonstrate how different working conditions such as pressure, sliding velocity and geometry can affect grow or decay of the imposed perturbations. Furthermore, we examined how the temperature-dependency of the coefficient of friction leads to the formation of hot and cold spots on the disks. The number of these spots or domains depends upon the thermal diffusivity of the disk material and affects the reproducibility of the brake test results. Larger number of spots is desirable for better reproducibility. It can be achieved either by decreasing of the thermal diffusivity (however, this approach comes in conflict with the need of high dissipation rates), by increasing the disk area, or, alternatively, by texturing the surface and dividing it artificially into domains.

## Chapter 3

### Running-in as a Self-organized process

#### 3.1. Objective

In this chapter, we study frictional running-in. Running-in is a transient period on the onset of the frictional sliding, in which friction and wear decrease to their stationary values. In this research, running-in is interpreted as friction-induced self-organization process. We introduce a theoretical model of running-in and investigate rough profile evolution assuming that its kinetics is driven by two opposite processes or events, i.e., the smoothening which is typical for the deformation-driven friction and wear, and the roughening which is typical for the adhesive-driven friction and wear. To validate our modeling results, we examine experimentally running-in in ultrahigh vacuum friction tests for WC pin versus Cu substrate. Furthermore, we propose to calculate the Shannon entropy of a rough profile and to use it as a simple test for self-organization.

#### 3.2. Background

When frictional sliding of two solid bodies is initiated, friction and wear usually remain high during a certain initial transient period, referred to as the running-in period (Blau, 1989). After the running-in, friction and wear tend to decrease to their stationary values. This decrease of kinetic friction after the initiation of the motion is a general trend. The opposite trend – increasing friction during the running-in – is rarely reported in the literature. Furthermore, the



coefficient of kinetic friction (i.e., after sliding has been initiated) is normally higher than the coefficient of static friction (i.e., before sliding has been initiated). In addition, in the models of dynamic friction, such as the state-and-rate models, it is usually assumed, on the basis of experimental observations, that with any change of the sliding velocity, the friction force tends to rise abruptly and then to decrease to its stationary value during a transient process (Nosonovsky, 2007). Therefore, there is a general tendency for friction to decrease during the transient, or running-in process.

There are numerous phenomenological explanations of the running-in phenomenon, dealing with various mechanisms, such as viscoplastic deformation, creep, deformation of asperities. Researchers have paid most of their attention to the empirical change laws, and the characterization of surface topography in running-in process (Blau, 1989; Begtsson and Ronnenberg, 1986; Roy Chowdhury et al., 1979). However, a general thermodynamic description of the running-in, which would explain its underlying physical principles, is absent from the literature.

During the running-in, surface topography evolves until it reaches a certain stationary state referred to as the equilibrium roughness distribution. The surfaces adjust to each other, leading to a more ordered state with lower dissipation rates. In this chapter, we consider the running-in as a self-organized process leading to a more ordered state of the surface corresponding to lower dissipation rates. We introduce a surface roughness parameter (the Shannon entropy), which characterizes quantitatively the degree of surface orderliness, and investigate how the evolution of surface roughness during friction affects the rates of dissipation (i.e., friction) and surface deterioration (i.e., wear).

### 3.3. Shannon Entropy as a characteristic of a rough surface

Friction and wear are two processes which occur during the sliding of solid surfaces and are intimately related to each other. They both reflect the tendency of materials to irreversibly deteriorate and energy to dissipate. During friction, heat is generated and dissipated, so the thermodynamic entropy grows. During wear, the surface is deteriorated so that parts of the material are removed as wear particles. The integrity of the material is measured by the so-called configurational entropy. There is evidence that wear rate, and therefore rates of configurational entropy, are proportional to the rates of thermodynamic entropy thus making friction and wear two sides of the same process.

The configurational entropy is related to the number of ways of arranging all the particles of the system while maintaining some overall set of specified system properties, such as energy. The concept is closely related to the idea of bits of information needed to describe the interface. If the position of the surface profile  $y(x_n)$ , (where  $n=1$  to  $N$ ) at any point  $x_n$  is independent, then  $I=N\log_2(B)$  bits of information are needed to describe the state of the interface in general, where  $B$  is the range of  $y$  (number of “bins” of the vertical resolution), **Fig. 3.1**. However, if the interface is not completely random, less information can be needed.

Fleurquin et al. (2010) proposed the Shannon entropy of a rough profile as a measure of profile's randomness

$$S = -\sum_{j=1}^B p_j \ln(p_j) \quad (3.1)$$

where  $N_j$  is the number of appearances in the bin  $j$ ,  $N$  is the total number of data points,  $p_j = N_j / N$  is the probability of appearance of a height in the bin  $j$ , and  $B$  is the total number of bins. The Shannon entropy is a generalization of the thermodynamic entropy suggested by

L.Boltzmann for the information theory. Fleurquin et al. (2010) used the so-called “Robin-Hood model” to investigate the evolution of the surface roughness due to wear, assuming diffusion-like kinetic law (height is “redistributed” between neighboring points, similarly to the wealth redistribution by Robin Hood).

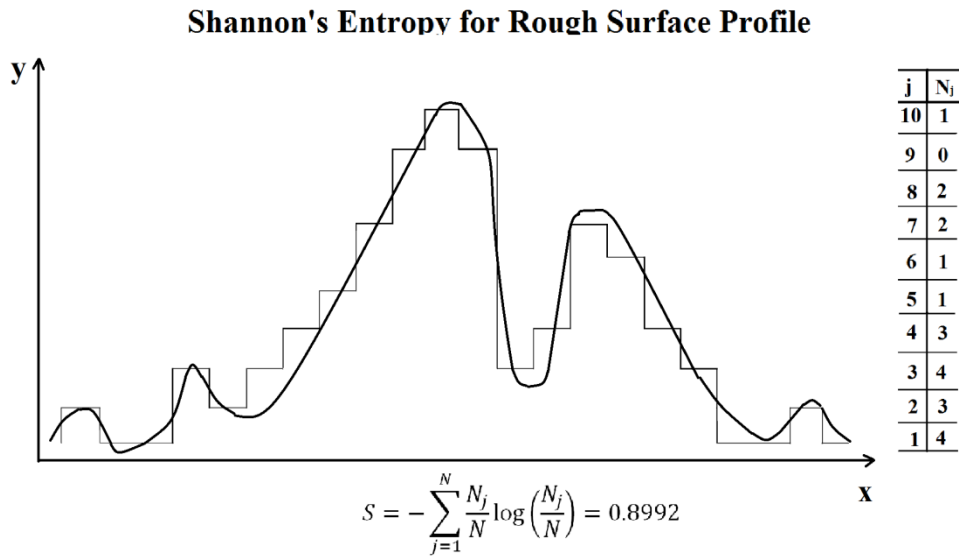


**Figure 3.1. Example of how Shannon Entropy could be calculated for Rough Surface Profile**

A surface profile with lower Shannon entropy is “more ordered” (or “less random”) than a profile with a higher Shannon entropy, and, therefore, decreasing Shannon entropy during the transient process is indication of self-organization. Thus, a smooth surface ( $B = 1$ ,  $p_1 = 1$ ) has the lowest possible entropy  $S = 0$ , and for a periodic rectangular profile (**Fig. 3.2**) we have  $0 < S < 0.3$ .

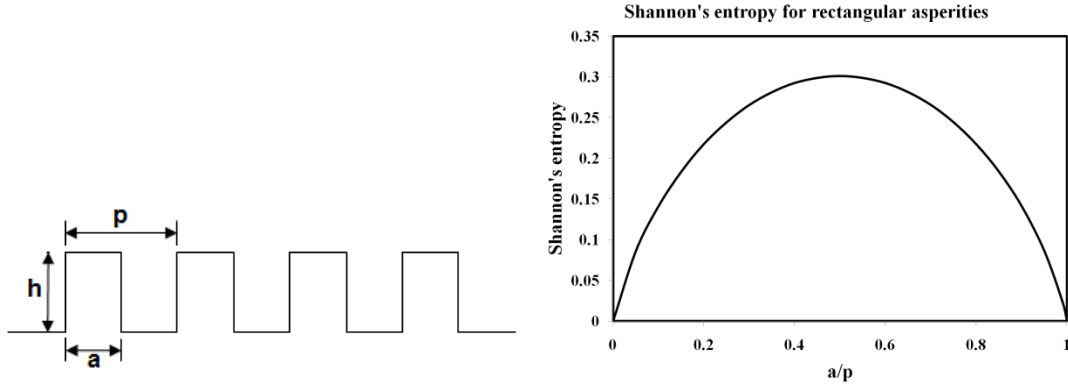


**Figure 3.2.** For a periodic rectangular profile, the Shannon entropy is between 0 and 0.3.

Note that the Shannon entropy, as defined by Eq. 1, takes into consideration only the height distribution of the profile and does not depend upon the spatial distribution. In this regard, the Shannon entropy is similar to the Root-mean-square (RMS) or the standard deviation ( $\sigma$ ), the standard roughness parameters popular among the tribologists, measured over the range  $L$ , where  $m$  is defined as the mean value,

$$\sigma^2 = \frac{1}{L} \int_0^L [y(x) - m]^2 dx, \quad m = \frac{1}{L} \int_0^L y(x) dx \quad (3.2)$$

The RMS, similarly to the Shannon entropy, does not take into consideration the spatial distribution and correlation of heights between neighboring points. However, such spatial correlation is an important characteristic of the profile. The parameter known as the correlation length,  $\beta$ , is used sometimes and it is defined as the length scale at which correlation between the heights of the neighboring points decays.

Note that the profile entropy as a measure of randomness is not the same as other surface roughness parameters in a traditional sense, such as the RMS. The profile can have the same degree of randomness at different values of the RMS, and different RMS for the same level of randomness.

### 3.4. Thermodynamic Model for surface roughness kinetics

We will investigate rough profile evolution, assuming that its kinetics is driven by two types of processes or events:

(1) The smoothening event is typical for the deformation-driven friction and wear. High asperities fracture due to the deformation (abrasive wear) resulting in smoothening of the profile.

(2) The roughening event is typical for the adhesive-driven friction and wear, which has higher rate for smoother surfaces.

When a particle is removed from the interface due to abrasive or adhesive wear, the data point  $y(x)$  is driven from a high bin  $j$  into a lower bin  $i$ , so the Shannon entropy would change by

$$\Delta S = \frac{N_j - 1}{N} \ln \frac{N_j - 1}{N} - \frac{N_j}{N} \ln \frac{N_j}{N} + \frac{N_{j-1} + 1}{N} \ln \frac{N_{j-1} + 1}{N} - \frac{N_{j-1}}{N} \ln \frac{N_{j-1}}{N} \quad (3.3)$$

Using  $\ln(x + \Delta x) - \ln(x) \approx \Delta x / x$  yields

$$\Delta S = \frac{1}{N} \ln \frac{N_i}{N_j} \quad (3.4)$$

Smoothening occurs when a particle moves from a less populated bin  $j$  into a more populated bin  $i$ , and the change of entropy is negative, whereas in the opposite case of roughening the change of entropy is positive.

As discussed in the previous section, two types of processes occur at the interface: roughening and smoothening. Furthermore, for a very rough surface smoothening is significant whereas for a very smooth surface roughening is significant, so that a certain value of equilibrium roughness can exist. While a comprehensive model of these processes would involve many complex factors, we suggest here a phenomenological model. We assume that the entropy

rate due to smoothening is proportional to the value of Shannon entropy, whereas the entropy rate due to roughening is inverse-proportional to the value of entropy.

$$\dot{S} = -AS + B/S \quad (3.5)$$

where  $A$  and  $B$  are phenomenological coefficients.

The first term in Eq. (3.5) represents the tendency of a rough surface to smoothen, which is typical for the deformational/abrasive wear (high asperities are destroyed due to deformation). The second term represents the tendency of a smooth surface to roughen, which is typical for the adhesive wear (smoother surface has higher adhesion). The solution of Eq. (3.5) has a stationary point that corresponds to  $\dot{S} = 0$ , and it is given by  $S = \sqrt{B/A}$ .

Sliding friction is caused by a number of mechanisms. The intensity of some of these mechanisms (such as the deformation of asperities) grows with roughness, whereas the intensity of others (such as adhesion) decreases with roughness. Again, we assume a simple phenomenological model, in which the coefficient of friction is related to roughness as

$$\mu = C_{def}S + C_{adh}/S \quad (3.6)$$

where  $C_{def}$  and  $C_{adh}$  are phenomenological coefficients related to the deformation and adhesion. The coefficient of friction and wear that correspond to the stationary state are given by

$$\mu = C_{def}\sqrt{B/A} + C_{adh}/\sqrt{B/A} \quad (3.7)$$

Note that the minimum friction corresponds to  $S = \sqrt{C_{adh}/C_{def}}$ . The stationary point of Eq. 5 corresponds to the minimum friction if  $B/A = C_{adh}/C_{def}$ . The assumption can be justified if the coefficients  $A$  and  $B$  are proportional to wear rates due to deformation and adhesion, which in turn, are proportional to friction components due to deformation and adhesion as designated by  $C_{def}$  and  $C_{adh}$ .

A control model, using the concept specified above, was developed with Matlab / Simulink software (**Fig. 3.3**). The model shows two feedback loops due to the deformation and adhesion mechanisms. The first feedback tends to decrease roughness when it is high, whereas the second tends to increase roughness when it is low.

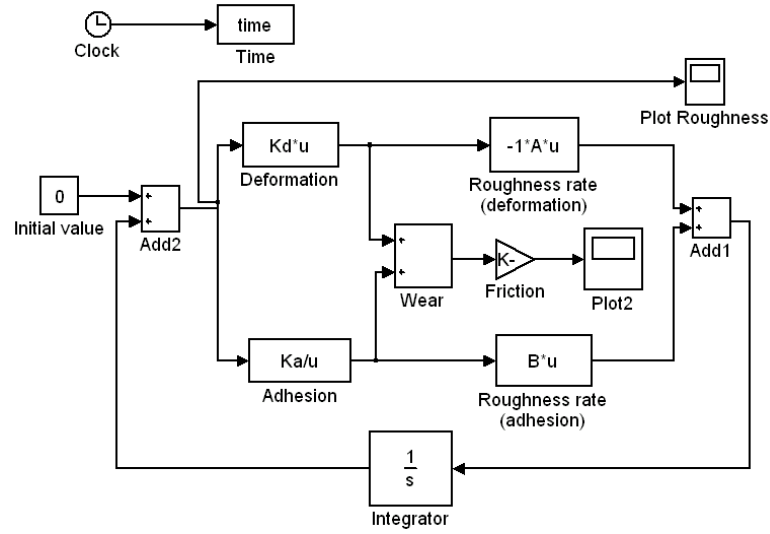


**Figure 3.3. A feedback loop model (top) and its presentation in Simulink (bottom). Two simultaneous processes (adhesion and deformation) affect surface roughness parameter in different manners. Consequently, an equilibrium value of roughness exists, which corresponds to minimum friction.**

Results of simulations are displayed in **Fig. 3.4**. The time-dependence of the coefficient of friction and roughness during the running-in simulated with Simulink for  $C_{def}=C_{adh}=1$  and for two cases:  $A=B$  and  $A \neq B$ . Several initial values of roughness were chosen and the evolution of roughness and the coefficient of friction was determined. In both cases, following the transient running-in process, roughness reaches its equilibrium value. For  $A=B$ , the coefficient of friction always decreases and reaches its minimum value as predicted by Eq. (3.4). However, for  $A \neq B$  the coefficient of friction can decrease or increase depending on the initial value of roughness.

For most practical situations, the initial roughness state of surface is rougher than the equilibrium steady-state roughness, so both the roughness and the coefficient of friction decrease during the running-in transient period and the self-organization takes place.

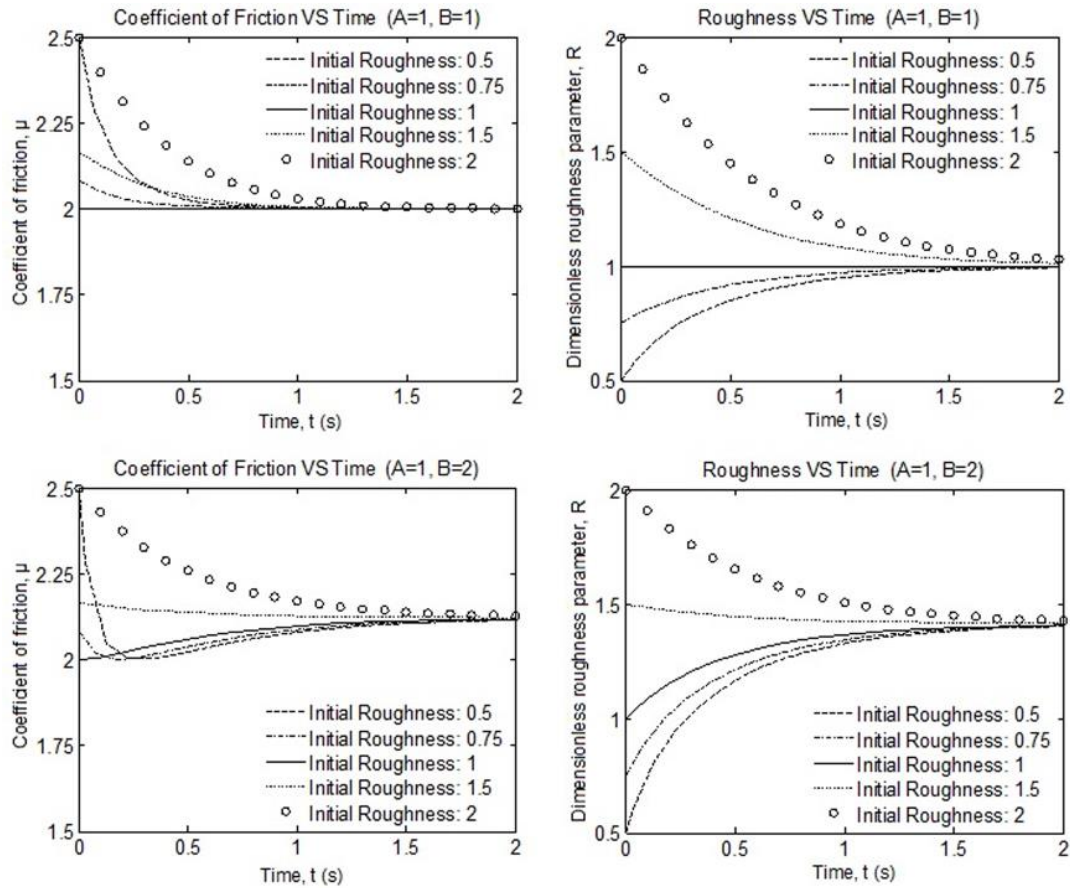


**Figure 3.4.** The time-dependence of the coefficient of friction and roughness parameter during the running-in simulated with Simulink for  $A=B$  and  $A \neq B$ . For  $A=B$ , while roughness reaches its equilibrium value, the coefficient of friction always decreases. Therefore, self-organization of the rough interface results in the decrease of friction and wear. For  $A \neq B$  the coefficient of can decrease or increase depending on the initial value of roughness.



### 3.5. Experimental

To investigate the evolution of roughness parameters in a transient running-in process, an experiment was conducted for the sliding friction of a copper (Cu) pin vs. tungsten carbide (WC) substrate. In order to eliminate the effects of oxidation and contamination, the experiment was carried out in an ultra-high vacuum (UHV) chamber tribometer, operating at the pressure  $\sim 3.5 \times 10^{-10}$  atmospheres.

The testing sample was made of 99.99% pure copper, while the material of pin was tungsten carbide (WC), selected due to its hardness and stiffness. The Cu sample (about  $20 \times 10 \times 1$  mm thickness) was mounted to a sample manipulator, which was oriented horizontally on the vacuum chamber and on the opposite of the tribometer. This allowed the sample to be moved to the center of the chamber for tribological experiments to be carried out. Moreover, sample could be placed in front of an ion bombardment source for sample cleaning.

The vacuum tribometer consisted of a tribopin mounted to the end of an arm that could be moved horizontally (in the  $x$  and  $y$  directions) and also vertically (in the  $z$  direction), either toward or away from the sample, which is oriented horizontally during experiment. These motions were controlled by external servomotors, which allowed the pin position to be precisely determined and normal ( $z$  direction) and lateral or friction ( $x$  direction) forces were simultaneously measured by strain gauges mounted to thinned sections of the triboarm. The apparatus was under computer control, so the loads, scan speed, scan area and scan pattern could be selected. More details of the apparatus are presented in Wua et al., (2002).

Measurements were made using a single pass in the same direction with the sliding speed of 4 mm/s with a normal load of 0.9 N, and the experiment was conducted at the room temperature. The aim was to produce scratches with a different number of scans (rubblings), each

one representing different period of transient running-in process. To do so, number of scans of tribopin on the surface of sample respectively increased for scratch No. 1 to 5, namely, 1, 4, 8, 16 and 32 scans. Two series of these scratches, each one with the length of 4 mm, were produced.

After conducting the scratching experiments, Atomic force microscopy (AFM) images of different scratches were obtained using Pacific Nanotechnology Nano-R™ AFM. The AFM includes a motorized zoom/focus video microscope, an AFM scanner, three motors for moving the probe towards the sample, a sample holder and a motorized X-Y positioning stage. The AFM cantilever was made of silicon with  $\text{Si}_3\text{N}_4$  coating, in conical shape and with the tip radius of about 10 nm. The topography images were produced in the contact mode. Scans (512 x 215 pixels) were collected at a minimum of three different locations on each scratch. Then, image processing was performed using SPIP software package (by Image Metrology) to obtain figures of different roughness parameters such as roughness Average ( $R_a$ ), root mean square (RMS), Extreme-value height descriptor ( $R_t$ ), Skewness (SK) and Kurtosis (K).

### 3.6. Results

Using direct measuring of both the normal and lateral forces (the normal force, however, was kept constant at 0.9 N, as described), the coefficient of friction during running-in process was calculated, and is displayed in Fig. 6. As expected, the coefficient of friction was reduced during running-in until it reached the steady state value of 0.43.

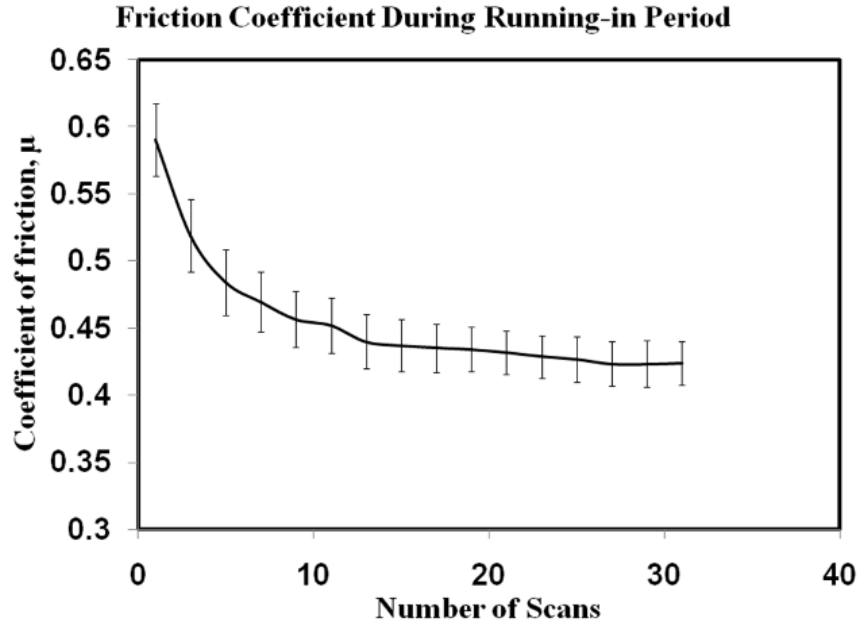


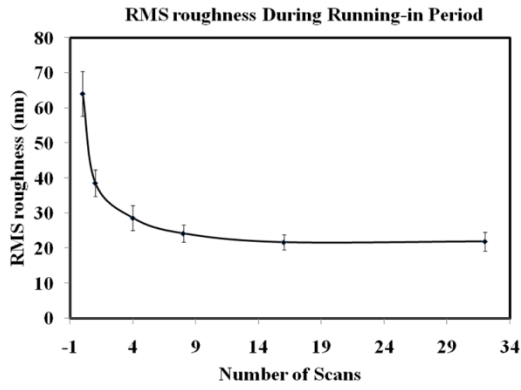
Figure 3.5. Friction coefficient change during running-in process.

As described above, five roughness parameters, Average ( $R_a$ ), root mean square (RMS), Extreme-value height descriptor ( $R_t$ ), Skewness (SK) and Kurtosis (K) were obtained. The variations of these roughness parameters are displayed in Fig. 5(a-e).

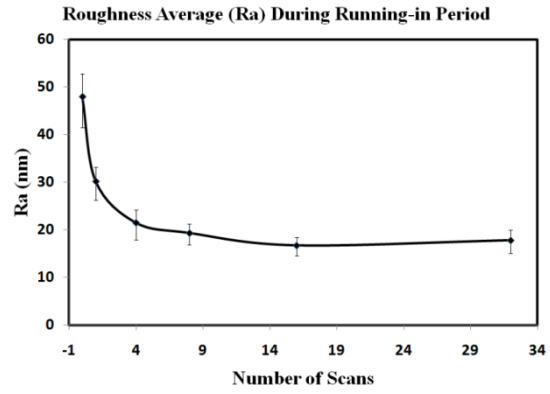
The Root-mean-square, roughness average, extreme-value height, and surface skewness, decreased during the transient process, showing the progressive change in the surface topography. The dramatic decrease of these parameters, which occurred in the very early scans can be attributed to removing the predominant peaks of initial roughness. As discussed theoretically, the surfaces were observed to be smoothened steadily until equilibrium roughness was achieved. However, the trend with the kurtosis was different. **Fig. 5e** displays the increase of surface kurtosis during first scans from  $K=4.349$  to  $K=6.198$ , and, reaching average of  $K=6.522$  in last scans. Increasing value of kurtosis means increasing of degree of pointedness of

surface profile. With obtaining probability density function, the Shannon entropy values during running-in stage could be calculated.

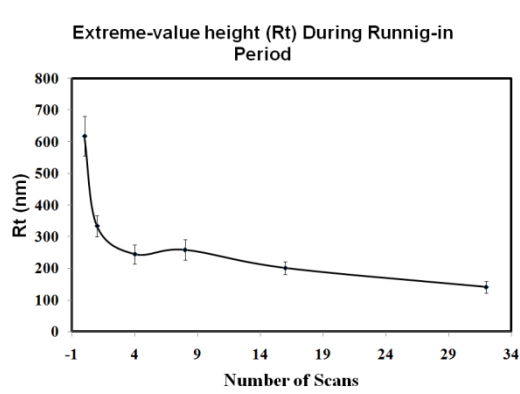
To compute the Shannon entropy during running-in stage we proceeded as follows. We obtained the height probability distribution for each location using above mentioned software. We took a fixed range of heights in this profile and divide this interval in  $B$  bins. We numerically found that for number of bins more than 1000 the amount of error in calculation of Shannon entropy was less than 1% thus we subsequently chose  $B = 1000$ . Then using Eq. 1, the results were plotted as shown in **Fig. 3.7**. It is observed that the entropy tended to decrease indicating that self-organization had occurred during the run-in period. This indicates that self-organization occurred during the transient run-in process due to mutual adjustment of surface roughness topography.



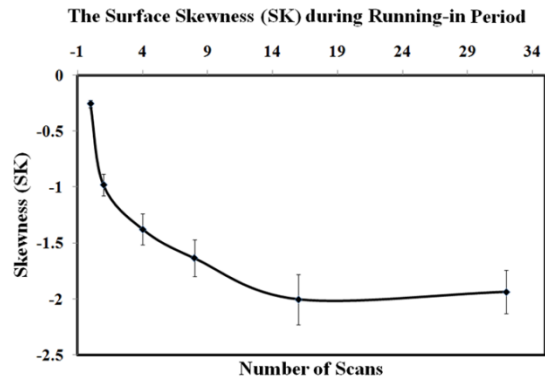
(a)



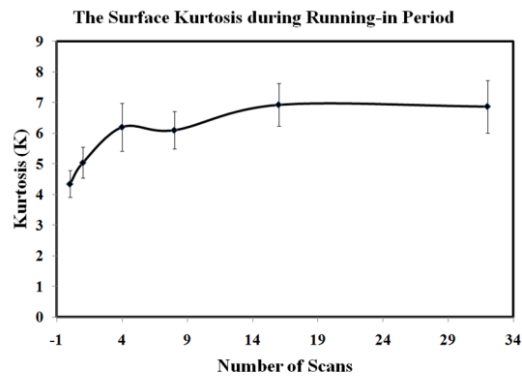
(b)



(c)



(d)



(e)

**Fig 3.6: variations of different roughness parameters during running-in period: Root Mean Square, Roughness Average, Extreme-value Height, Skewness, and Kurtosis respectively.**

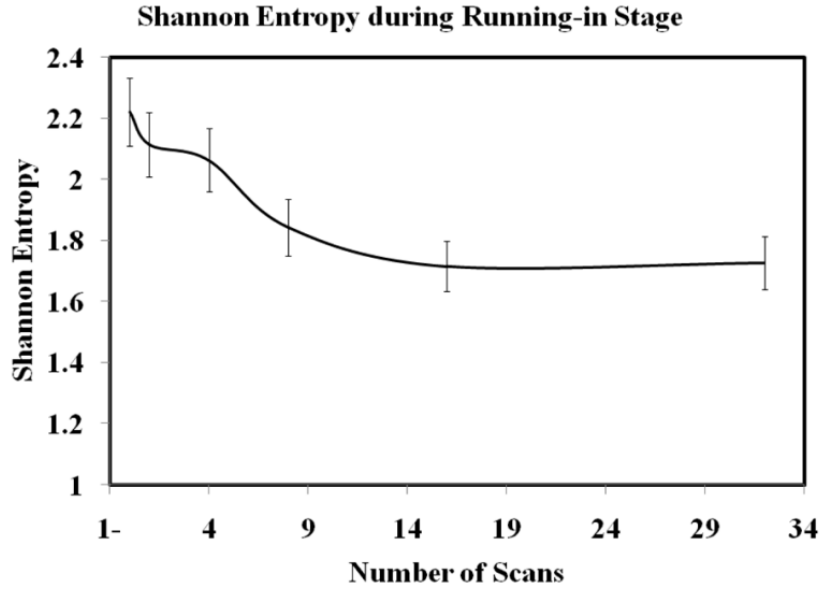


Figure 3.7: Shannon entropy during running-in period.

### 3.7. Conclusion

In this chapter, we developed a theoretical approach to study running-in period as an example of friction-induced self-organization. We conclude that friction, due to non-linear effects, can lead to a less random surface profile, and we used Shannon entropy as a measure of profile self-organization. The adjustment of surface roughness to an equilibrium value during the running-in transient process leads to the minimization of friction and wear and it was investigated by considering a feedback loop due to the coupling of two processes or mechanisms (in our example, adhesion and deformation). We found experimental evidences for our theoretical considerations. We observed how Shannon entropy as a characteristic of a rough surface profile quantifies the degree of orderliness of the self-organized system. Our

experimental and theoretical results showed that Shannon entropy decreases during running-in period, which indicates reaching more smother and more ordered surface profile.

## Chapter 4

### Frictional Turing systems

#### 4.1. Objective

In this chapter, we investigate the possibility of Turing-type pattern formation during friction. There are different type of patterns can form at the sliding interface due to the mass transfer (diffusion), heat transfer, various tribochemical reactions, and wear. We will study the possibility of Turing-type patterns in frictional interface. Turing or reaction-diffusion systems describe variations of spatial concentrations of chemical components with time due to local chemical reactions coupled with diffusion. We will present mathematical modeling, and will compare our mathematical findings with existing experimental data.

#### 4.2. Turing systems and self-organization

The reaction-diffusion systems and their important class called the “Turing systems” constitute a different type of self-organization mechanism. Kagan (2010) suggested that reaction-diffusion systems can describe certain types of friction-induced pattern formation involving heat transfer and diffusion-like mass transfer due to wear. While AMI and TEI involve wave propagation (hyperbolic) partial differential equations (PDE), which describes dynamic behavior of elastic media, the reaction-diffusion (RD) system involves parabolic PDE, typical for diffusion and heat propagation problems. The RD systems describe evolution of concentrations of reagents in space and time due to local chemical reactions and the diffusion of the product of reactions (Leppänen, 2004). The RD system of PDEs is given by



$$\frac{\partial w_j}{\partial t} = f_i(w_j) + d_{ij}\Delta w_j \quad (4.1)$$

where  $w_j$  is the vector of concentrations,  $f_i$  represent the reaction kinetics and  $d_{ij}$  and  $\Delta$  are a diagonal matrix of diffusion coefficients and Laplace operator, respectively. Alan Turing (1952) showed that a state that is stable in the local system can become unstable in the presence of diffusion, which is counter-intuitive, since diffusion is commonly associated with a stabilizing effect. The solutions of RD equations demonstrate a wide range of behaviors including the traveling waves and self-organized patterns, such as stripes, hexagons, spirals, etc.

While parabolic RD equations cannot describe elastic deformation, they may be appropriate for other processes, such as viscoplastic deformation and interface film growth. For a system of two components,  $u$  and  $v$ , Eq. (4.1) has the following form:

$$\frac{\partial u}{\partial t} = f(u, v) + d_u \left( \frac{\partial^2 u}{\partial x^2} + \frac{\partial^2 u}{\partial y^2} \right) \quad (4.2)$$

$$\frac{\partial v}{\partial t} = g(u, v) + d_v \left( \frac{\partial^2 v}{\partial x^2} + \frac{\partial^2 v}{\partial y^2} \right) \quad (4.3)$$

where  $f$  and  $g$  are the reaction kinetics functions and  $d_{ij}$  is a diagonal matrix ( $d_{11} = d_u$  and  $d_{22} = d_v$ ). Suppose that  $u$  represents the non-dimensional temperature at the sliding interface and  $v$  is the local slip velocity, also non-dimensional. The non-dimensional values of  $u$ ,  $v$ ,  $x$ ,  $t$ , and other parameter are obtained from the dimensional values by division of the latter by corresponding scale parameters. Then Eq. (4.2) is interpreted as the description of heat transfer along the interface, and Eq. (4.3) describes the flow of viscous material along the interface. In this chapter, we discuss several types of kinetic functions which can lead to the formation of periodic patterns.

### 4.3. Numerical simulation of frictional Turing systems

In this section, we define Turing systems which can describe pattern-formation at the frictional interface and a numerical scheme to simulate such systems. We suggest two interpretations of Eqs (4.2-4.3), which can describe the frictional contact of non-elastic materials and tribofilm formation. First, during friction, heat is generated and mass transfer occurs. The function  $f(u, v)$  characterizes the heat generation due to friction and can be taken, for example, in the form of

$$f(u, v) = w_0(\mu_0 + \alpha_1 u + \beta_1 v)u \quad (4.4)$$

where  $\mu_0 + \alpha_1 u + \beta_1 v$  is the coefficient of friction dependent on the temperature  $u$  and local slip velocity  $v$ , and the non-dimensional coefficients  $\alpha_1$  and  $\beta_1$  and  $w_0$  are constant. The function  $g(u, v)$  characterizes rheological properties of the material and depends on its viscous and plastic properties.

The second interpretation of Eqs. (4.2-4.3) can be used if the growth of a tribo-film (a thin interfacial layer activated by friction) is considered. Whereas  $u$  still represents the interfacial temperature,  $v$  can be interpreted as the non-dimensional thickness of the tribofilm formed at the interface. The tribofilm can grow due to the material transfer to the interface via diffusion activated by friction, due to precipitation of a certain component (e.g., a softer one) in an alloy or composite material, due to a chemical reaction, temperature gradient, etc. For example, during the contact of bronze vs. steel, a protective Cu tribofilm can form at the interface, which significantly reduces the wear. Such in-situ tribofilm has protective properties for the interface since it is formed dynamically and compensates the effect of wear. Furthermore, if wear is a decreasing function of the tribofilm thickness, it is energetically profitable for the film to grow, since growing film reduces wear and further stimulates its growth forming a feedback loop, until

a certain equilibrium thickness is attained. Therefore, such tribofilms can be used for machine tool protection and other applications, as discussed in the literature (Aizawa et al., 2005). The growth of the film is governed by interfacial diffusion and by a local kinetic function  $g(u, v)$  dependent upon the temperature and local film thickness.

One of the standard forms for functions  $f(u, v)$  and  $g(u, v)$  based on transferring original reaction-diffusion equations and proper scaling was proposed to be (Dufiet and Boissonade, 1991 and 1992):

$$f(u, v) = \gamma(a - u + u^2v) \quad (4.5)$$

$$g(u, v) = \gamma(b - u^2v) \quad (4.6)$$

In order to investigate the possibility of pattern-formation in a Turing system, a stability analysis should be performed. In the absence of diffusion,  $u$  and  $v$  can approach a linearly stable, uniform, steady state. However, under certain conditions, spatially inhomogeneous patterns can evolve by the diffusion-driven instability (Murray, 1989). A reaction-diffusion system exhibits diffusion-driven instability or Turing instability if the homogeneous steady state is stable to small perturbations in the absence of diffusion; however, it is unstable to small spatial perturbations when diffusion is introduced. Diffusion results in the spatially inhomogeneous instability and determines that spatial patterns that evolves.

From the linear stability analysis one can show that, when  $d_v > 1$  and  $d_u = 1$ , a solution with pattern-formation (Turing pattern) can exist, if the parameters satisfy the following conditions simultaneously (Dufiet and Boissonade, 1991 and Murray, 1989):

$$0 < b - a < (a + b)^3 \quad (4.7)$$

$$[d_v(b - a) - (a + b)^3]^2 > 4d_v(a + b)^4 \quad (4.8)$$

$$d_v(b - a) > (a + b)^3 \quad (4.9)$$

The results of the stability analysis are summarized in **Fig. 4.1** for  $d_v = 20$  (Dufiet and Boissonade, 1992; Murray, 1989). The plot shows two curves corresponding to the inequalities introduced by Eq. (4.7) and (4.8), whereas the third inequality (Eq. 4.9) corresponds to a curve which, for the given vales, lies outside the domain of the plot. Therefore, the inequalities divide the parameter space  $(a, b)$  into three regions. In the region 1, the steady state is stable to any perturbation. In the region 2, the steady state exhibits an oscillating instability. In the region 3, the steady state is destabilized by inhomogeneous perturbations. Along the border (1, 3) transitions from the uniform state to stationery spatial patterns occurs through a so-called Turing bifurcation. The region 3 is sometime called the “Turing space” and it is of interest for us, because it corresponds to pattern-formation.

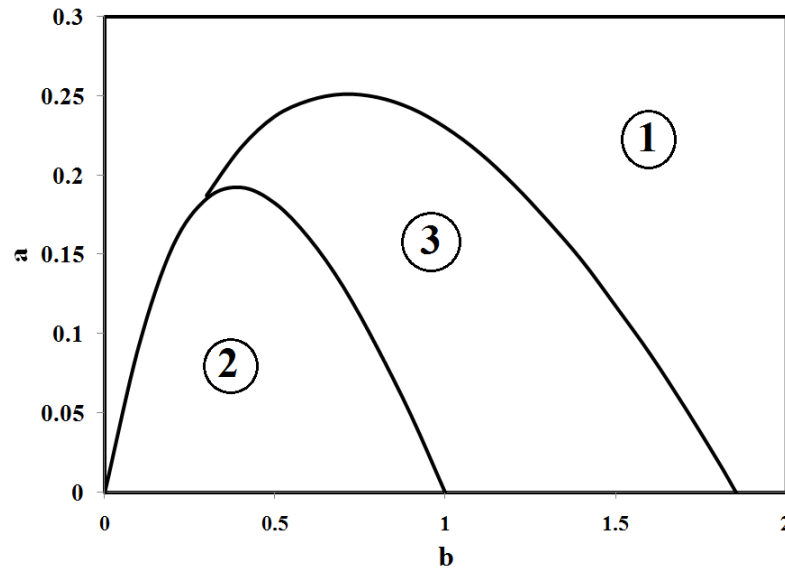


**Figure 4.1: Linear stability analysis. Region 1: uniform steady state, region 2: Oscillating instability, region 3: Turing patterns (Mortazavi & Nosonovsky, 2011b)**

After determining the region of parameters appropriate for pattern-formation from the stability analysis, we need to perform a numerical simulation. To solve the system of equations (2 - 3), a number of numerical schemes have been proposed. Approximating the diffusive term by second order backward difference, we used the second order semi implicit Backward Difference Formula (BDF) scheme proposed by Ruth (1995):

$$\frac{1}{2\Delta t}(3u^{n+1} - 4u^n + u^{n-1}) = 2f^n - f^{n-1} + d_u\Delta_h u^{n+1} \quad (4.10)$$

$$\frac{1}{2\Delta t}(3v^{n+1} - 4v^n + v^{n-1}) = 2g^n - g^{n-1} + d_v\Delta_h v^{n+1} \quad (4.11)$$

where  $n$  corresponds to the current time step and,  $n-1$  and  $n+1$  show the previous and next time steps.

Numerical simulations with different initial conditions are performed with the numerical scheme of Eqs. (4.10) and (4.11) with spatial step size,  $\Delta x = 0.001$ , and time step of  $\Delta t = 10^{-6}$ . The length and width of system is considered to be equal by 1 ( $L=1$ ).

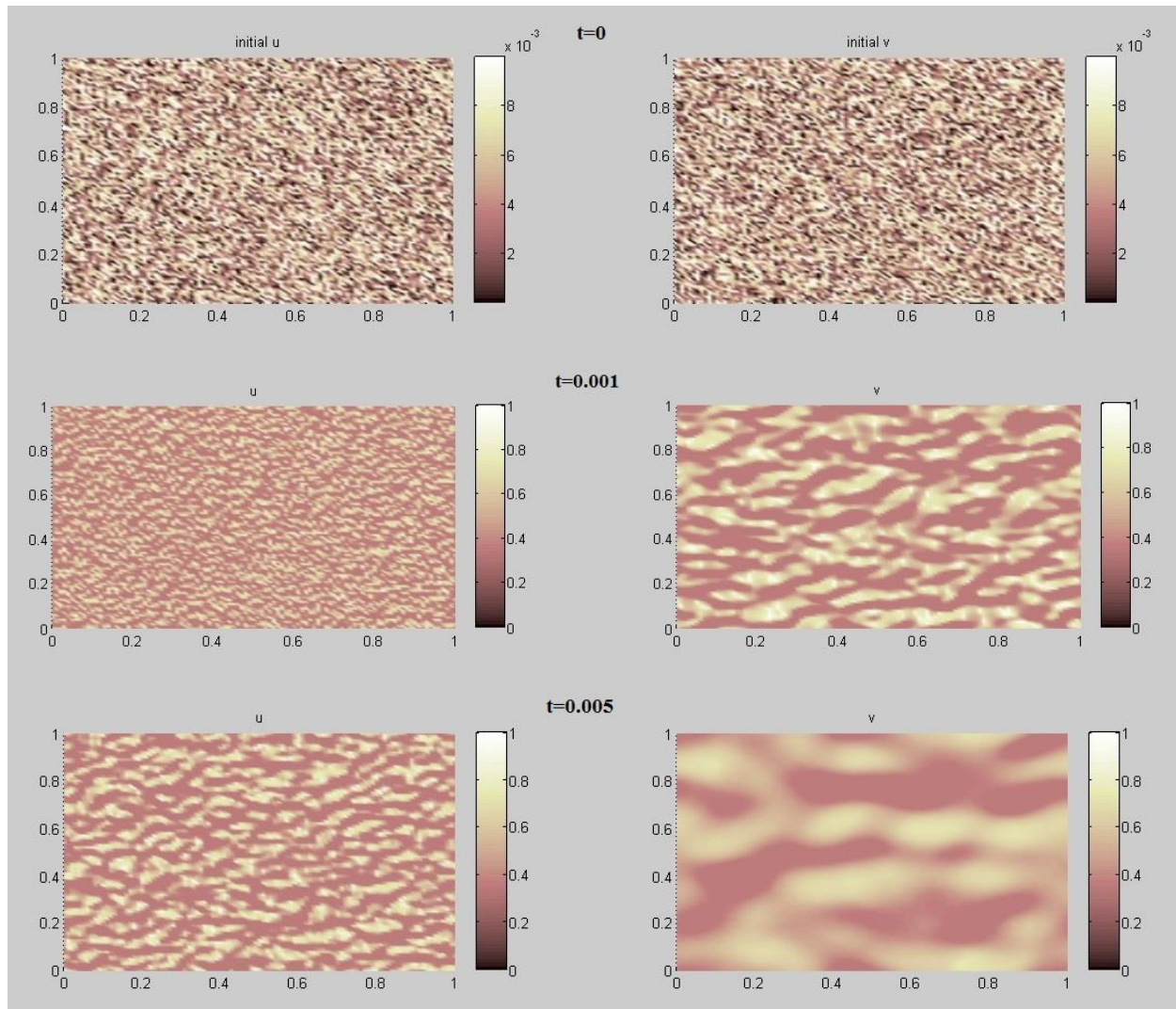
#### 4.4. Results

In this section we discuss several exemplary cases of parameter values and initial conditions which can lead to patterns. The cases 1 and 2 are the classical examples of the Turing systems, whereas the case 3 is justified by the frictional mechanism of heat generation and mass transfer.

For the first case, we selected the following values of the parameters in Eqs. (4.5) and (4.6) based on discussion of the stability presented in the preceding section

$$\gamma = 10000, d_v = 20, a = 0.02, \text{ and } b = 1.77 \quad (4.12)$$

For the initial conditions we set a random distribution function (using Matlab 7.0 standard package) for both values of  $u$  and  $v$ . Time evolution of  $u$  and  $v$  at different time steps is shown in **Fig. 4.2**.



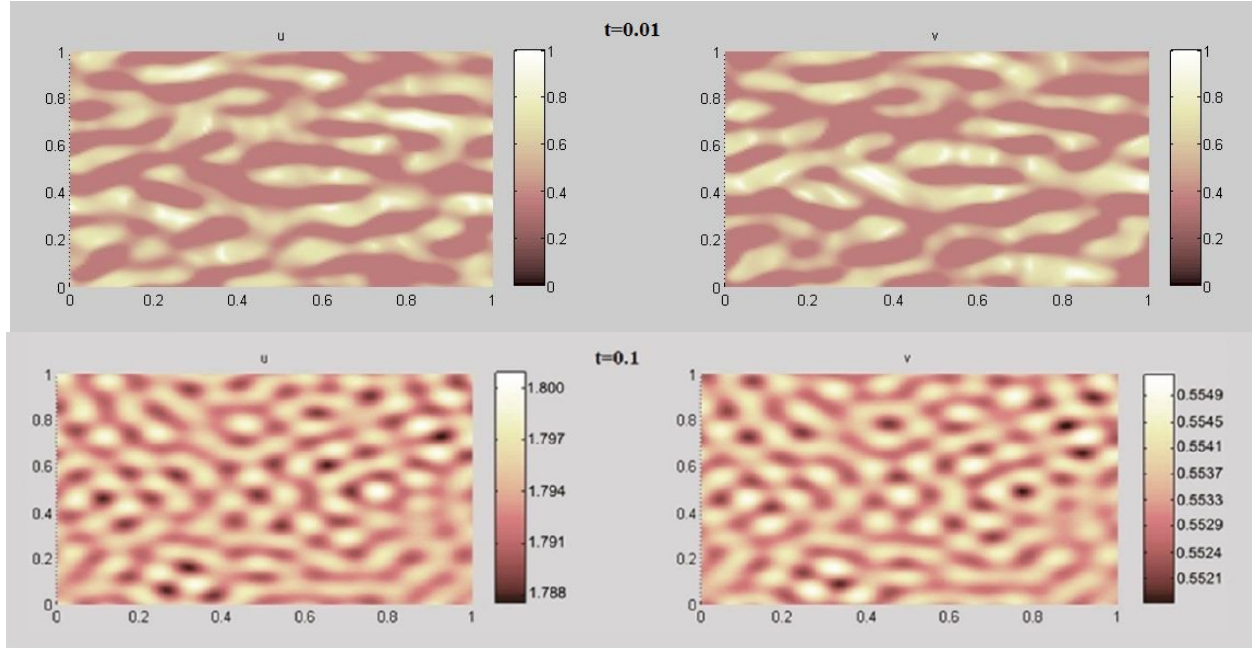


**Figure 4.2:** Time evolution of amounts of  $u$  and  $v$  in different time steps, at  $t = 0, 0.001, 0.005, 0.01$ , and  $0.1$  (First case) (Mortazavi & Nosonovsky, 2011b)

For the second case, we used the following values for the parameters in Equations 4.5 and 4.6 based on above mentioned points

$$\gamma = 10000 \quad \& \quad d_v = 20 \quad \& \quad a = 0.07 \quad \& \quad b = 1.61 \quad (4.13)$$

For initial conditions, we considered the following harmonic functions

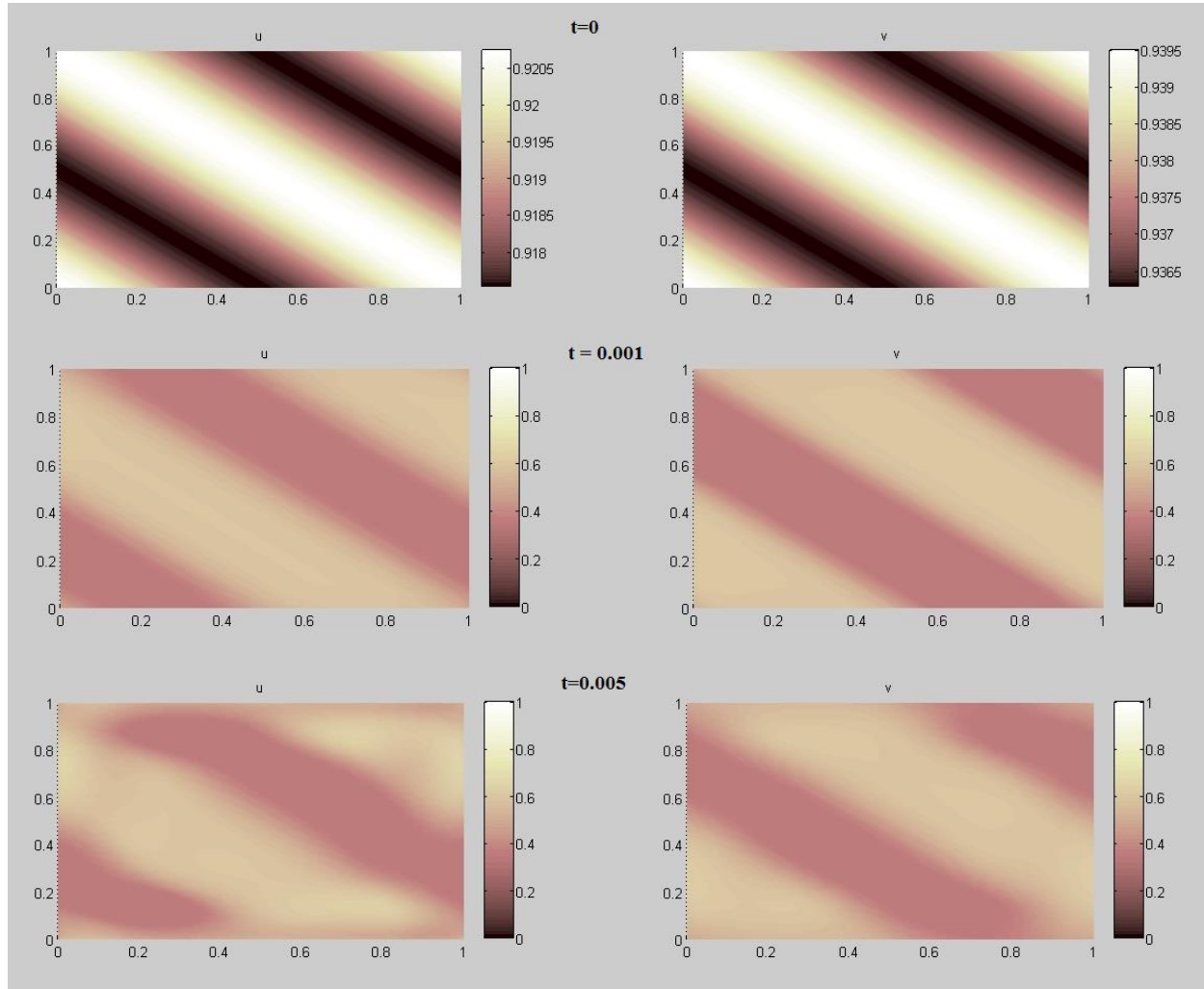
$$u(x, y) = 0.919145 + 0.0016 \cos(2\pi(x + y)) \quad (4.14)$$

$$v(x, y) = 0.937903 + 0.0016 \cos(2\pi(x + y)) \quad (4.15)$$

The time evolution of  $u$  and  $v$  at different time steps ( $t = 0, 0.001, 0.005, 0.01, 0.05$  and  $0.1$ ) is shown in **Figure 4.3**.

The results in **Fig. 4.3** present five consecutive snapshots of the system described by Eqs. 2- 3 corresponding to different time steps. The results, here, show how gradually, from initially striped patterns, the reaction-diffusion mechanism leads to a new periodic patterns. For

example, a comparison of the concentrations of  $u$  and  $v$  demonstrates how an almost perfectly stripped patterns ( $t = 0.001$ ) starts to break down at  $t = 0.005$ . Similarly to what has been observed in **Fig. 4.2**, the phase difference between  $u$  and  $v$  values in each point is found: when  $u$  has a high value,  $v$  has a low one, and vice versa.





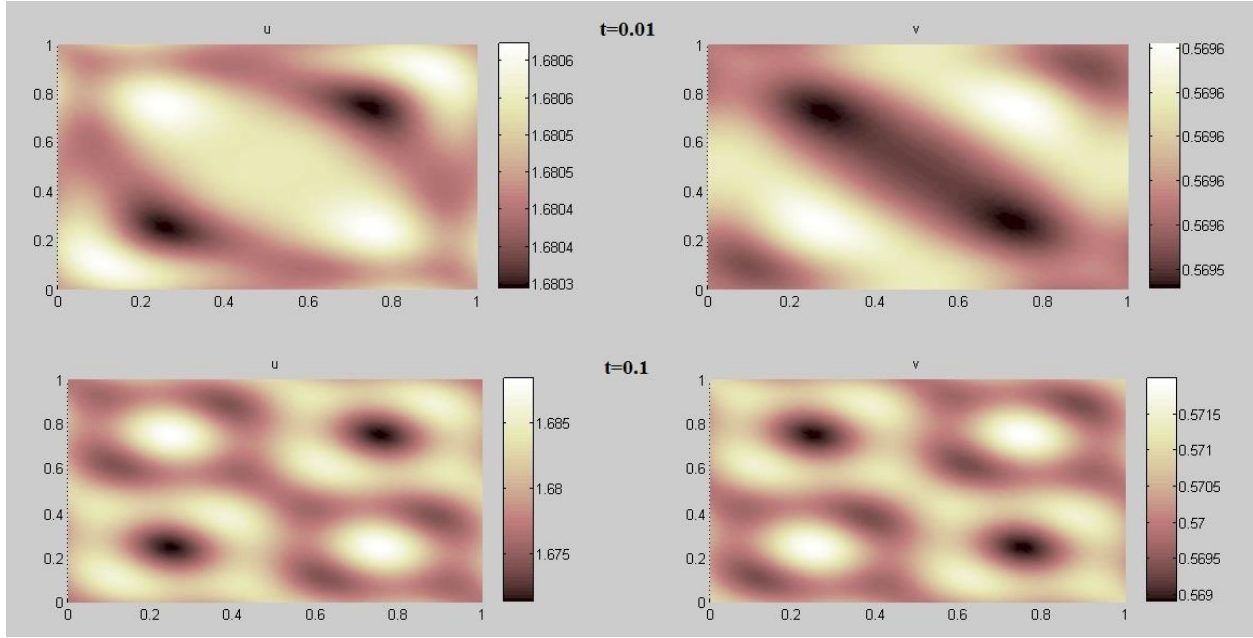


**Figure 4.3: Time evolution of  $u$  and  $v$  values in different time steps,  $t = 0, 0.001, 0.005, 0.01, 0.05$  and  $0.1$**

**(Second case) (Mortazavi & Nosonovsky, 2011b)**

Whereas the two first cases showed that our model is capable of capturing the self-organized patterns in Turing systems, in the third case we tried to use more specific functions of reaction kinetics, which are expected to characterize friction-induced reaction mechanisms. Let's consider  $u$  as a non-dimensionalized temperature and  $v$  as a non-dimensionalized tribofilm thickness

$$\frac{\partial u}{\partial t} = f(u, v) + d_u \left( \frac{\partial^2 u}{\partial x^2} + \frac{\partial^2 u}{\partial y^2} \right) \quad (4.16)$$

$$\frac{\partial v}{\partial t} = g(u, v) + d_v \left( \frac{\partial^2 v}{\partial x^2} + \frac{\partial^2 v}{\partial y^2} \right) \quad (4.17)$$

And let's assume that functions  $f(u, v)$  and  $g(u, v)$  to be in the following forms

$$f(u, v) = w_0(\mu_0 + \alpha_1 u + \beta_1 v)u \quad (4.18)$$

$$g(u, v) = (\alpha_2 u + \beta_2 v) \quad (4.19)$$

or:

$$g(u, v) = (\alpha_2 u + \beta_2 v)u \quad (4.20)$$

As initial conditions, we used following equation as a temperature distribution

$$u(x, y) = 0.002 \cos(2\pi(x + y)) + 0.01 \sum_{j=1}^8 \cos(2\pi jx) \quad (4.21)$$

and random distribution function as an initial roughness for  $v(x, y)$ . Moreover, we considered following values for parameters of Eqs. 4.18 and 4.19

$$\begin{aligned} w_0 &= 10^2, \quad \alpha_1 = 10^{-4}, \quad \beta_1 = 10^{-4}, \quad \mu_0 = 5 * 10^{-1}, \\ \alpha_2 &= 10^{-4}, \quad \beta_2 = 10^{-4} \end{aligned} \quad (4.22)$$

The results for different time steps, using Eqs. 4.18 and 4.19 are shown in **Figure 4.4**. Similar results with considering Eq. 4.20 as  $g(u, v)$ , a non-linear function, is shown in **Figure 4.5**.

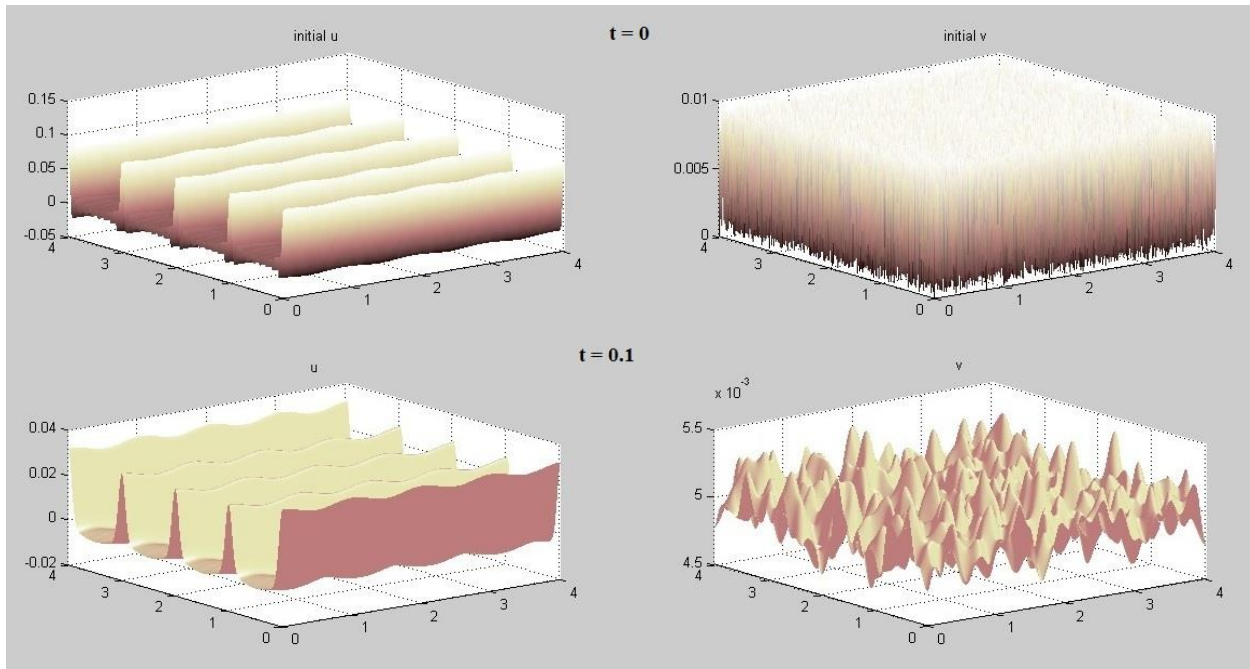


**Figure 4.4: Time evolution of  $u$  and  $v$  values in two different time steps (Third case, using equations 4.18 and 4.19) (Mortazavi & Nosonovsky, 2011b)**

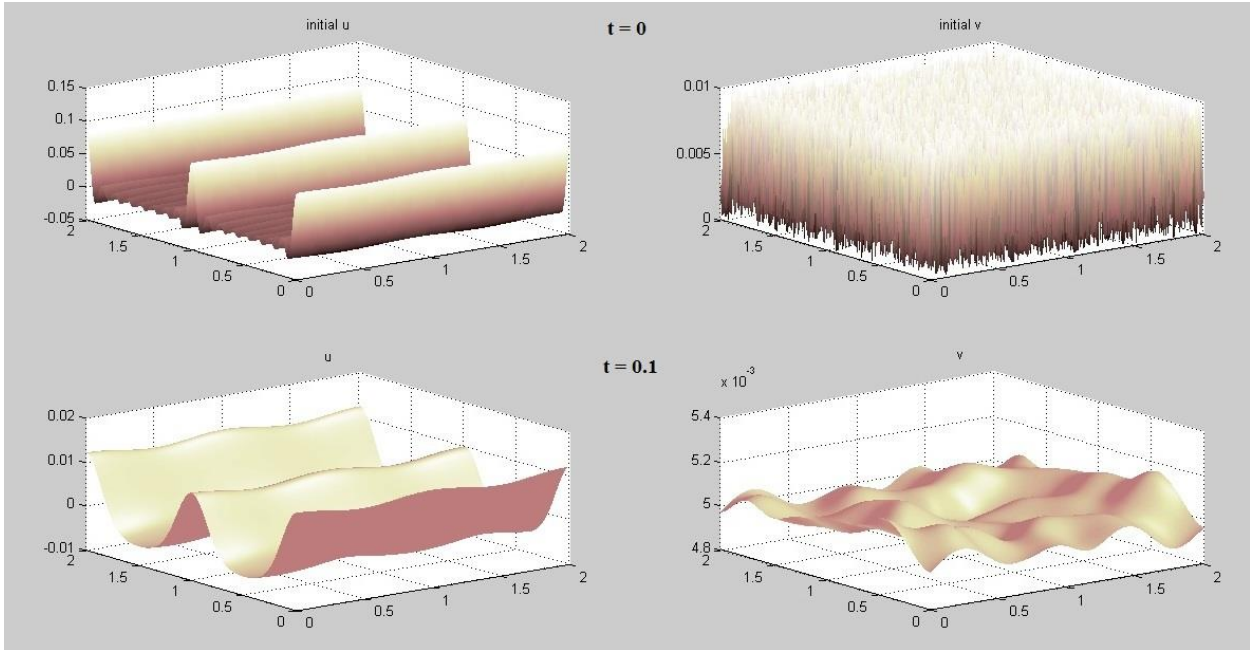


**Figure 4.5: Time evolution of  $u$  and  $v$  values in different time steps (Third case, using equations 4.18 and 4.20) (Mortazavi & Nosonovsky, 2011b)**

It is obvious that patterns found in **Fig. 4.5** and **4.6** are not the same as the patterns which we found in the two previous cases. However, we observe similar trends in the evolution of tribofilm thickness ( $v$ ) from an initially random distribution of roughness to a more organized and more patterned distribution. However, the investigation of pattern formation based on solving complete three-dimensional heat and mass transfer equations in tribofilm is needed to show more realistic picture of how and under what conditions such patterns could occur. In the next section we will discuss possible experimental evidence of friction-induced pattern-formation.

#### 4.5. Discussion

The modeling analysis in the preceding sections shows that properly selected functions  $f(u,v)$  and  $g(u,v)$  can lead to pattern-formation. The question remains on whether any experimental data can be interpreted as friction-induced patterns formed by the RD mechanism? It would be appropriate to look for this type of self-organization in processes involving viscoplastic contact or diffusion-dominated effects, e.g. in situ tribofilms. There are several effects which can be interpreted in this way. The so-called “secondary structures” can form at the frictional interface due to the self-organization (Fox-Rabinovich & Totten, 2006), and some of these structures can have a spatial pattern.

One example is the so-called “selective transfer” suggested by Garkunov (2000). This term refers to a dynamically formed protective tribofilm, which is formed due to a chemical reaction induced by friction. The film protects against wear, since the processes of wear and formation of the film are in dynamic equilibrium (Nosonovsky, 2010). While it is generally assumed that the film is homogeneous with constant thickness at any given moment of time, some data suggest that spatial structures can form. The non-homogeneity of the tribofilm may be caused by various reasons; a similar phenomenon is well known when destabilization of a thin liquid layer occurs during de-wetting (Herminghaus, et al., 1998) and it was found also in solid films due to the interplay of adhesion and friction (Shenoy and Sharma, 2001).

The selective layer (an in-situ tribofilm due to the selective transfer) formed during friction between steel and a copper alloy (bronze) was investigated experimentally by Ilie and Tita (2007). In the presence of glycerin or a similar lubricant, the ions of copper were selectively transferred from bronze to the frictional interface forming the copper tribofilm. This copper was different in its structure from the copper that falls out through normal electrolytic procedures. Ilia

and Tita (2007) investigated the selective layer using the Atomic Force Microscopy (AFM) and found that the layer formed micro-island pattern with the size on the order of 1  $\mu\text{m}$ , rather than a uniform film of constant thickness. Schematic figure of such layer could be seen in **Fig. 4.6**.

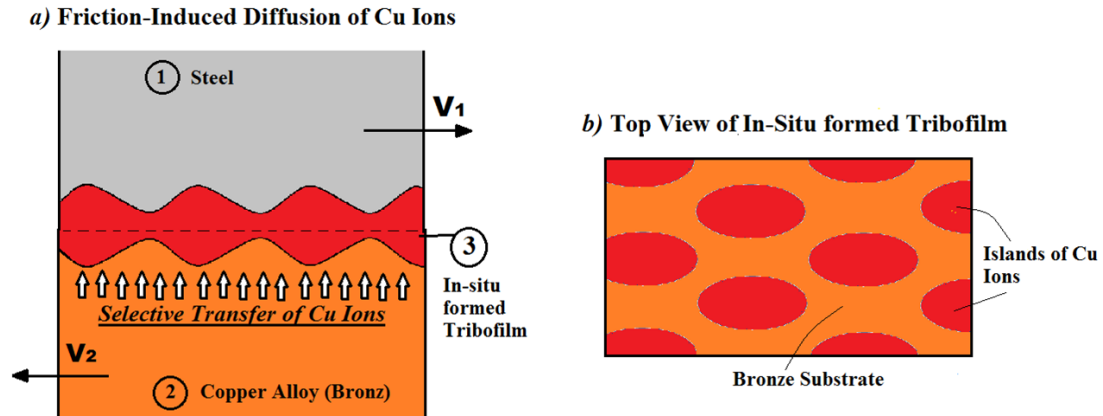


**Figure 4.6:** Schematic presentation of the selective layer (b) obtained by friction between a surface of steel and (a) a surface of copper alloy (bronze) (Mortazavi & Nosonovsky, 2011b)

Another important example of pattern-formation reported in the literature is related to the self-adaptive mechanisms improving the frictional properties of hard coatings, e.g., during dry cutting, by tailoring their oxidation behavior (Erdemir et al., 1991 and 1996, and Lovell et al., 2010). Thus, boric acid formation on boron carbide is a potential mechanism for reaching ultra-low friction. Such mechanism uses the reaction of the boric oxide ( $\text{B}_2\text{O}_3$ ) with ambient humidity ( $\text{H}_2\text{O}$ ) to form a thin boric acid ( $\text{H}_3\text{BO}_4$ ) film. The low friction coefficient of boric acid is associated with its layered triclinic crystal structure (Erdemir, 2001; Singer et al., 2003). The layers consist of closely packed and strongly bonded boron, oxygen, and hydrogen atoms, but the layers are widely separated and attracted by van der Waals forces only. During sliding, these atomic layers can align themselves parallel to the direction of relative motion and slide easily over one another (Erdemir et al., 1996).

The tribological behavior of protective coatings formed by both ex-situ and in-situ transfer films were studied by Singer et al. (2003). Coatings that exhibit long life in sliding contact often do so because the so-called “third body” forms and resides in the sliding interface. The concept of the “third body” as a separate entity, different from the two contacting bodies, is very similar to the concept of the tribofilm. Ex-situ surface analytical studies identified the composition and structure of third bodies and provided possible scenarios for their role in accommodating sliding and controlling friction. In-situ Raman spectroscopy clearly identified the third bodies controlling frictional behavior during sliding contact between a transparent hemisphere and three solid lubricants: the amorphous Pb–Mo–S coating was lubricated by an MoS<sub>2</sub> transfer film; the diamond-like carbon/nanocomposite (DLC / DLN) coating by a graphite-like transfer film; and the annealed boron carbide by H<sub>3</sub>BO<sub>3</sub> and/or carbon couples. In-situ optical investigations identified third body processes with certain patterns responsible for the frictional behavior (Singer et al., 2003).

TiB<sub>2</sub> thin films are well known for their high hardness which makes them useful for wear-resistant applications. Mayrhofer et al. (2005) showed that overstoichiometric TiB<sub>2.4</sub> layers have a complex self-organized columnar nanostructure precursor. Selected area electron diffraction (SAED) pattern from a TiB<sub>2.4</sub> layer showed a texture near the film/substrate interface with increased preferred orientation near the film surface (Mayrhofer et al., 2005). The film has a dense columnar structure with an average column diameter of ~20 nm and a smooth surface with an average root-mean-square roughness essentially equal to that of the polished substrate surface, ~15 nm.

Aizawa et al. (2005) investigated in-situ TiN and TiC ceramic coating films utilized as a protective coating for dies and cutting tools. They found that chlorine ion implantation assists

these lubricious oxide ( $\text{TiO}$  and  $\text{Ti}_n\text{O}_{2n-1}$ ) film to be in-situ formed during wearing. They also performed the microscopic analysis and observed worn surfaces and wear debris and found microscale patterns.

Lin and Chu (2009) described Bénard cell-like surface structures found from the observation of the Transmission electron microscopy (TEM) images of the scuffed worn surface as a result of lubricated steel vs. steel contact. They attributed the cells to high temperatures (800 °C) and very strong fluid convection or even evaporation occurring inside the scuffed surface. However, the possibility of diffusion-driven based pattern formation should not be ruled out.

The experimental evidences of pattern formation, which can, at least theoretically attributed to the reaction-diffusion mechanism, are summarized in **Table 4.1**. Further evidence is needed to rule out alternative explanations.

**Table 4.1:** Summary of different experimental pattern formation evidences discussed in literature  
(Mortazavi and Nosonovsky, 2011b)

	Materials in contact	Tribofilm material	Mechanism	Pattern	Reference
1.	steel vs. copper alloy (bronze)	copper	the selective transfer	Cu islands (~1 $\mu\text{m}$ )	Ilie & Tita (2007)
2.	boric oxide ( $\text{B}_2\text{O}_3$ )	thin boric acid ( $\text{H}_3\text{BO}_4$ ) film	Oxidation	Layered pattern	Erdemir et al. (1991 and 1996) and Lovell et al. (2010)
3.	Glass vs. Pb–Mo–S	MoS <sub>2</sub> films	transfer film	MoS <sub>2</sub> islands (nanoscale)	Singer et al. (2003)
4.	sapphire against a DLC/DLN coating	silicone-formed DLC/DLN coating	transfer film	Silicone islands (nanoscale)	Singer et al. (2003)
5.	TiN vs. AlN	TiB <sub>2</sub> thin films	oxidation	columnar structure (~20 nm)	Mayrhofer et al. (2005)
6.	steel vs. steel	TiN or TiC films of 1 $\mu\text{m}$	oxidation	microscale patterns	Aizawa et al. (2005)
7.	steel vs. steel	$\alpha$ -Fe inside the substrate of the unscuffed surface	Wear	Bénard cell like patterns	Lin and Chu (2009)



#### **4.6. Conclusion**

We conclude that the evolution of reaction-diffusion system can describe the formation of certain types of friction-induced interfacial patterns. These patterns can form at the sliding interface due to the processes of mass transfer (diffusion and wear), heat transfer and various tribochemical reactions. On the other hand, existing experimental data suggest that in-situ formation of tribofilms due to a variety of friction-induced chemical reactions (such as boric acid formation, oxidation, and selective transfer of Cu ions from the bulk to the interface) or wear can result in the formation of interfacial patterns (islands or honeycomb type domains). This pattern formation can be attributed to the Turing systems.

## Chapter 5

### Stick-slip motion and self-organization

#### 5.1. Objective

In this chapter, we investigate how interfacial patterns including propagating trains of stick and slip zones formed due to dynamic sliding instabilities can be categorized as self-organized patterns or dissipative secondary structures. We will treat stick and slip as two phases at the surface. Then, we will study the effects related to phase transitions.

#### 5.2. Different models of stick-slip motion

As it was discussed in chapter 1, the stick-slip phenomenon occurs if the coefficient of static friction is greater than the coefficient of kinetic friction. This phenomenon can be defined by sliding mass-spring systems like the one in **Figure 5.1**. A block with mass  $M$  is pushed by a spring or loading stage of stiffness  $K$ , at speed  $V$ . The driving force  $F_X$  is the force in the spring. One commonly observes the sliding regimes shown in **Figure 5.2**. In **Figure 5.2a** the system enters a steady sliding regime: the block moves at the driving speed and the force in the driving spring equals the dynamic friction force at this driving velocity. **Figure 5.2b** and **Figure 5.2c** show dynamic instability: the block alternates between sticking periods in which  $F_X$  builds up, and fast sliding events. In experiments the system can be brought into the steady sliding regime by increasing  $V$  and/or  $K$ . Stick-slip phenomenon depends not only on the friction force, but also on different system parameters such as the inertia, stiffness, surface roughness and mass of the moving parts.

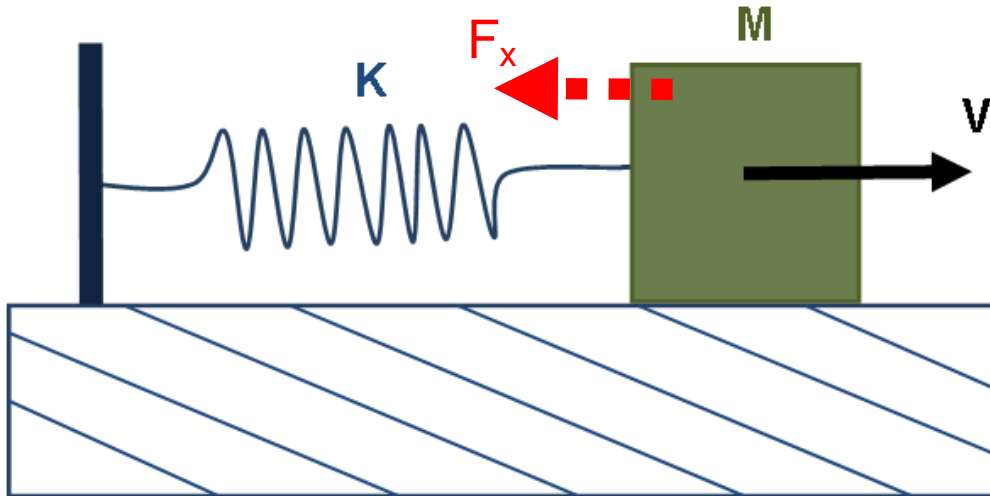


**Figure 5.1.** A typical mass-spring system. The stiffness  $K$  can represent an actual spring or an effective stiffness of the loading apparatus.  $M$  and  $V$  also represent mass, and velocity, respectively.

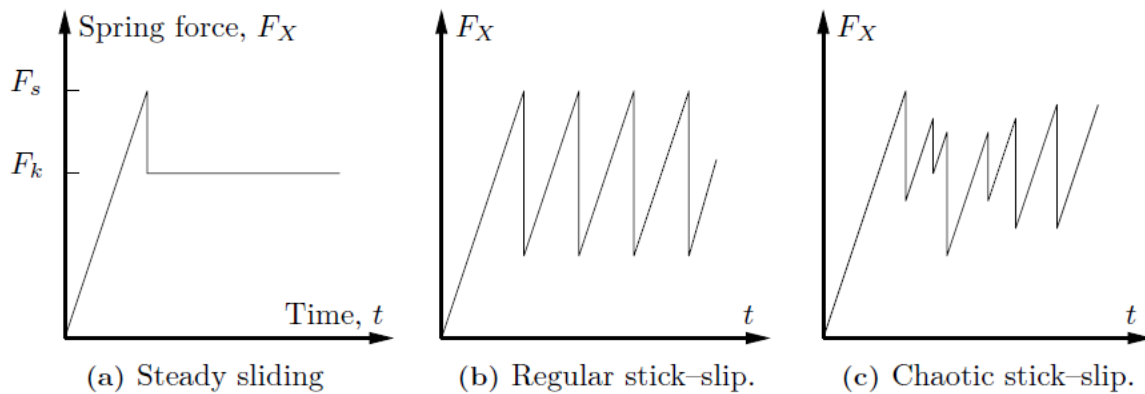


**Figure 5.2.** Three different sliding regimes for the system in Figure 5.1.

There has been several detailed models for stick-slip friction that include the effects of molecular or asperity size, sliding velocity, various relaxation times, previous history, and other system parameters as mentioned above. It has been suggested (Berman et al., 1996) that we can categorize three different models of stick-slip: surface topology (roughness) models, distance-

dependent models, and velocity-dependent models. However, this classification is not exclusive, and molecular mechanisms of real systems may exhibit aspects of these three different models, simultaneously (Berman et al., 1996).

The surface topology (roughness) models explain stick–slip in terms of the topology or roughness of the sliding surfaces (Berman et al., 1996; Rabinowicz, 1965). As the slider climbs an asperity on the substrate, a resisting force is encountered. Once the peak is reached, the slider will slide down rapidly into the valley, resulting in a slip. The measured friction trace with time will show regular or irregular stick–slip “spikes” depending on whether the surface corrugations are themselves regular, as for a lattice plane, or irregular, as for a randomly rough surface. The controlling factors of this type of stick–slip are the topology of the surface (the 2D amplitude and periodicity of protrusions) and the elastic and inertial properties of the sliding surfaces which determine the rate of slip (Berman et al., 1996). In addition, a stiffer material will have shorter slips because of the shorter recoil to elastic equilibrium. This would allow sticking to more of the smaller asperities, resulting in a richer stick–slip spectrum. With increasing hardness of the materials, plastic deformations during sliding are reduced and the friction pattern approaches a true “contour trace” of the surfaces. Topological stick–slip is observed in the sliding of macroscopically rough surfaces, as well as in atomic force microscopy (AFM) experiments where the intermittent motion of the slider (AFM tip) is a measure of the molecular-scale roughness or atomic-scale corrugations of the surface lattice (Berman et al., 1996).

Dependence of stick-slip motion to other topological parameters was also suggested (Menezes et al., 2010, Tanaka et al., 2003; Gee et al., 1990; Demirel & Granick, 1998). Menezes et al. (2010) observed that for the case of Al under lubricated conditions, the amplitude of stick-slip oscillations depends on the grinding angle. The amplitude of oscillations starts at 25° and

increases through  $90^\circ$ . They argued that the amplitude of stick-slip motion primarily depends on the plowing component (rather than on the adhesion component) of friction. At  $90^\circ$ , the condition at the asperity level is plane strain leading to higher stresses being generated during sliding. The lubricant present at the interface will experience higher compression and increased viscosity. The increased viscosity will ultimately lead to stick-slip motion. As the grinding angle decreases, the degree of plane strain condition decreases, which reduces the amplitude of stick-slip motion.

Tanaka et al. (2003) reported that under high load conditions the lubricant film, confined and sheared between two solid walls, is compressed and solidified which results in stick-slip motion due to molecular deformation. Gee et al. (1990) observed that the occurrence of solid-like characteristics are due to the ordering of the liquid molecule into discrete layers. In general, these properties depend not only on the nature of the liquid but also on the atomic structure of the surfaces, the normal pressure, and the direction and velocity of sliding (Gee et al., 1990). Demirel and Granick (1998) observed liquid-like response at low deformation rates and stick-slip-like response at high deformation rates. For the case of Mg, the stick-slip phenomenon was observed by Menezes et al. (2010) under both dry and lubricated conditions. When comparing the properties of Al and Mg, the two major differences are the hardness and the number of slip systems. Mg has a higher hardness and lower number of slip systems. A lower number of slip systems could itself promote stick-slip motion as some of the grains in contact at the asperity level would be difficult or easy depending on the orientation of the slip planes. Such a difference in slip within the contact zone would promote stick-slip which could explain why stick-slip is observed under both dry and lubricated conditions for Mg (Menezes et al., 2010).

Distance-dependent models of stick–slip suggest that two rough macroscopic surfaces adhere through their microscopic asperities of characteristic length (Berman et al., 1996; Rabinowicz, 2002; Rabinowicz, 1965). During shearing, each surface must first creep a distance of characteristic length - the size of the contacting junctions - after which the surfaces continue to slide, but with a lower (kinetic) friction force than the original (static) value. The reason for the decrease in the friction force is that even though, on average, new asperity junctions should form as rapidly as the old ones break, the time dependent adhesion and friction of the new ones will be lower than the old ones (Berman et al., 1996).

The friction force therefore remains high during the creep stage of the slip, but once the surfaces have moved the characteristic distance, the friction rapidly drops to the kinetic value (Berman et al., 1996). This type of friction has been observed in a variety of mainly dry systems such as paper-on-paper (Heslot et al., 1994; Baumberger, 1994) and steel-on-steel (Rabinowicz, 1958; Rabinowicz, 1951; Heymann et al., 1954). This model is also used extensively in geology to analyze rock-on-rock sliding (Yoshizawa, 1993).

Velocity-dependent models suggest different stick–slip mechanisms. Especially, they can be used for surfaces with thin liquid films (Berman et al., 1996). One of the simplest models is a pure velocity-dependent friction law. In this case there is a high static friction, when the surfaces are at rest because the film has solidified. Once the shearing force exceeds this value, the surfaces slide with a lower kinetic friction force, because the film is now in the molten, liquid-like state. Stick–slip sliding proceeds as the film goes through successive freezing–melting cycles. Freezing and melting transitions at surfaces or in thin films may not be the same as the freezing–melting transitions between the bulk solid and liquid phases (Berman et al., 1996). Such films may be considered to alternate between two states, characterized by two friction

forces, or they can have a rich friction-velocity spectrum, as proposed by Persson (1994). The tribological and other dynamic properties of such confined films have been extensively studied by Robbins & Thompson (1991) and Landman et al. (1992, 1989) using computer simulations. Carlson and Batista (1996) have developed a comprehensive rate and state dependent friction force law. This model includes an analytic description of the time-dependent freezing and melting transitions of a film, resulting in a friction force that is a function of sliding velocity in a natural way. This model predicts a full range of stick–slip behavior observed experimentally.

It was observed (Berman et al., 1996) that the experimental results of sliding with liquid lubricants in a number of systems involving smooth surfaces are consistent with velocity and time dependent phase transition models for stick–slip friction. For these idealized systems there was no need to invoke a distance-dependent model, nor the classical model based on a negative friction force–velocity profile. In general, more theoretical and mathematical work is needed to give a complete picture of friction mechanisms involved in stick-slip phenomenon, and to answer how self-organization occurs through these mechanisms.

### **5.3. Stick and slip friction phases**

As we discussed, the stick-slip phenomenon can occur if the coefficient of static friction is greater than the coefficient of kinetic friction. When the stick-slip motion occurs, the frictional force does not remain constant, but rather oscillates significantly as a function of sliding distance or time. During the stick phase, the friction force builds to a critical value. Once the critical force has been attained to overcome the static friction, slip occurs at the interface, and energy is released so that the frictional force decreases.

The stick-slip phenomenon is found in many situations, such as car brake vibration and squeal. However, it is particularly common at the atomic scale; for example, during the contact

of an atomic force microscope tip with an atomically smooth surface the energy dissipation takes place through stick-slip movement of individual atoms at the contact interface (Nosonovsky and Bhushan, 2008).

Stick and slip can be treated as two phases at the surface. The definition of a phase in physical chemistry is that properties of a medium do not change within the same phase. The effects related to phase transitions can be studied then. Einax et al. (2004) used this approach. Their numerical analysis demonstrated that for small interatomic interaction strength, the system is in a frictionless state, but when the strength is above the critical value, there is static friction. They analyzed scaling behavior of the order-parameter near the critical value and calculated corresponding critical exponents. The order-parameter and the energy functional can be powerful mathematical tools to study scaling laws of friction and near-critical behavior.

Rubinstein et al. (2004) studied experimentally with a high-speed camera the onset of frictional slip. They observed three fronts propagating with different velocities: subsonic, intersonic and an order of magnitude slower. No overall motion (sliding) of the blocks occurs until either of the slower two fronts traverses the entire interface. Their overall conclusion is that the static coefficient of friction is a “myth,” while kinetic friction is a result of stick-slip.

#### **5.4. Numerical modeling**

We introduce a model including spring-mass system describing wearless dry friction between two flat solids. We assume that upper body can be seen as a number of masses ( $N$ ) sliding on a lower body. We also consider that there is a total force of  $P$  which is applied through lower body to upper spring-mass system, resulting in friction force of  $P_i$  between mass number  $i$  and lower surface. The balance of the forces for each mass can be written as



$$m_i \ddot{x}_i + \eta_i (Vt - x_i) + k_i (x_{i+1} - 2x_i + x_{i-1}) = \mu_i W \quad (5.1)$$

Where  $m$  is the mass,  $\mu$  is the coefficient of friction,  $k$  is the spring constant,  $\eta$  is the damping coefficient, and  $V$  is the sliding velocity.

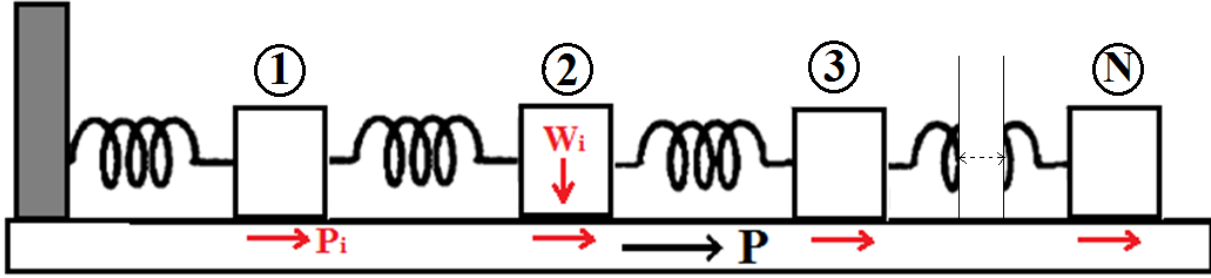


Fig 5.3. Schematic picture of spring-mass system;  $N$  denotes number of masses.

Furthermore, the dynamics of each mass can be described by the following equation,

$$m_i \ddot{x}_i = \frac{\partial U}{\partial x_i} \quad (5.2)$$

where  $U$  is the total potential energy of the system which can be described as following

$$P = \sum_{i=1}^N \frac{k_i}{2} (x_{i+1} - 2x_i + x_{i-1})^2 + \sum_{j=1}^N \frac{\eta_j}{2} (Vt - x_j)^2 + \sum_{i=1}^N \mu_i W x_i \quad (5.3)$$

We are interested to investigate behavior of the spring-mass system due to the applied force. To do so, the numerical simulation was performed as follows:

1. With introducing force to the system, for each time step ( $\Delta t$ ), we compute position of each cell by integration of Eq. 5.3

$$x_i = \iint \frac{1}{m_i} \frac{\partial U}{\partial x_i} dx \quad (5.4)$$

2. We then calculate kinetic friction force for each cell based on new position

$$F_i = m_i \ddot{x}_i + \eta_i (Vt - x_i) + k_i (x_{i+1} - 2x_i - x_{i-1}) \quad (5.5)$$

3. Now, based on the following, we will decide whether each mass sticks or slips

$$\begin{cases} \text{stick} & \text{if } |F_i| < \mu_i W \\ \text{Slip} & \text{if } |F_i| > \mu_i W \end{cases} \quad (5.6)$$

4. In the case of stick, the position of  $x_i$  will not change, but for the slip,  $x_i$  will be updated.

5. Simulation will be repeated for new time step.

The simulations were done for number of masses  $N=1000$ . In each simulation, we applied different amount of force ranging from 2 to 25 kN and investigated how spring-mass system evolves during the time. Values of  $m$ ,  $k$  and,  $\eta$  kept constant during simulations, i.e. 2, 10 and 0.3, respectively. **Fig 5.4** shows how kinetic friction force changes with time for different masses.

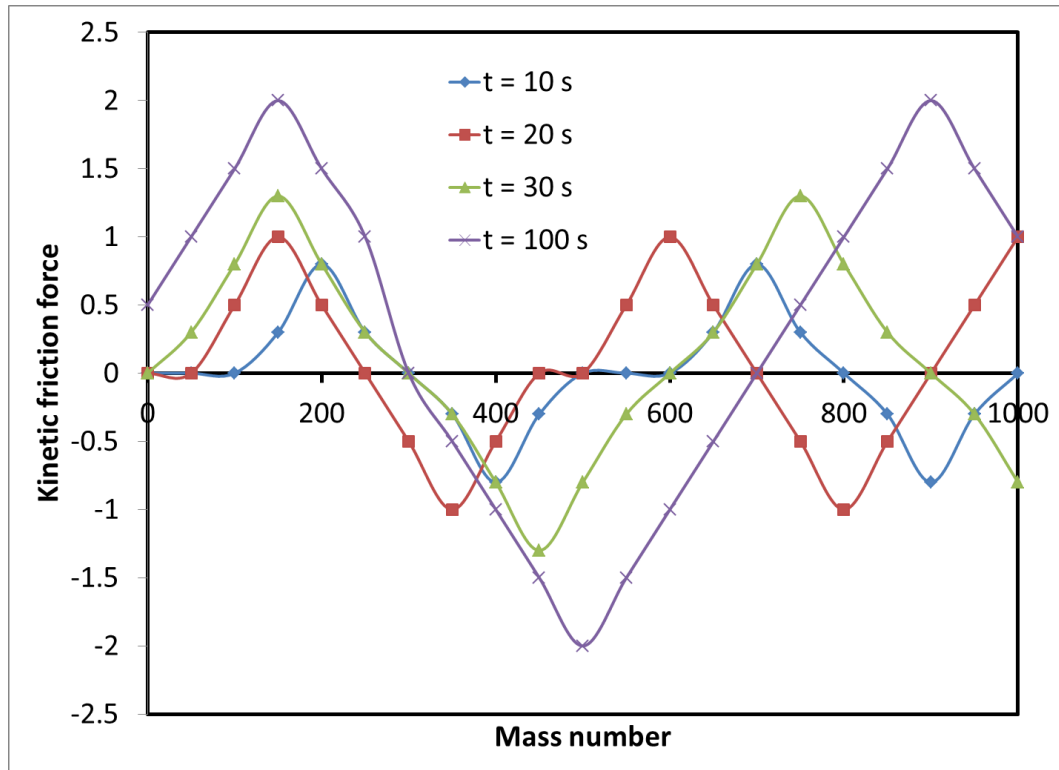


**Fig 5.4: Distribution of Kinetic friction force for different masses (Number of mass =1000)**

Then, we investigated how the size of slip zone changes due to tangential force. **Fig 5.5** shows the size of the stick region decreases, with increase of the tangential force, until overall sliding begins. We also see in **Fig 5.6** how local slips make instable regions which can finally lead to stable, self-organized region. These results clearly show how stick-slip patterns form during the first stages of sliding. These results are also in line with experimental observations by Rubinstein, Cohen, and Fineberg (2004) who showed that dynamic friction is a result of stick-slip fluctuations.

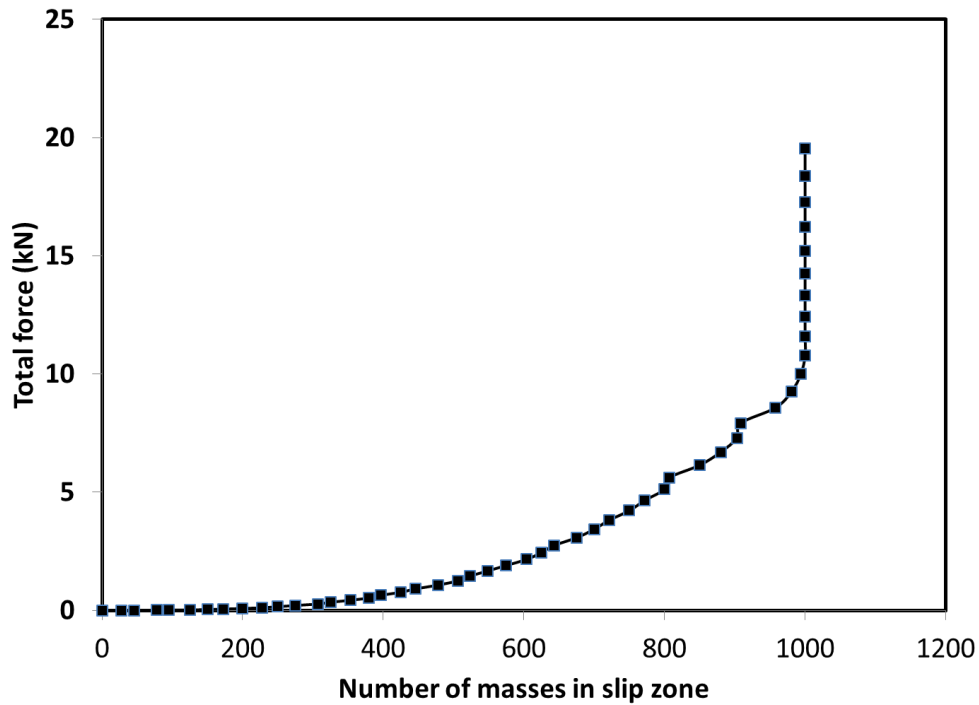


**Fig 5.5:** Total applied force versus slip zone (number of masses)

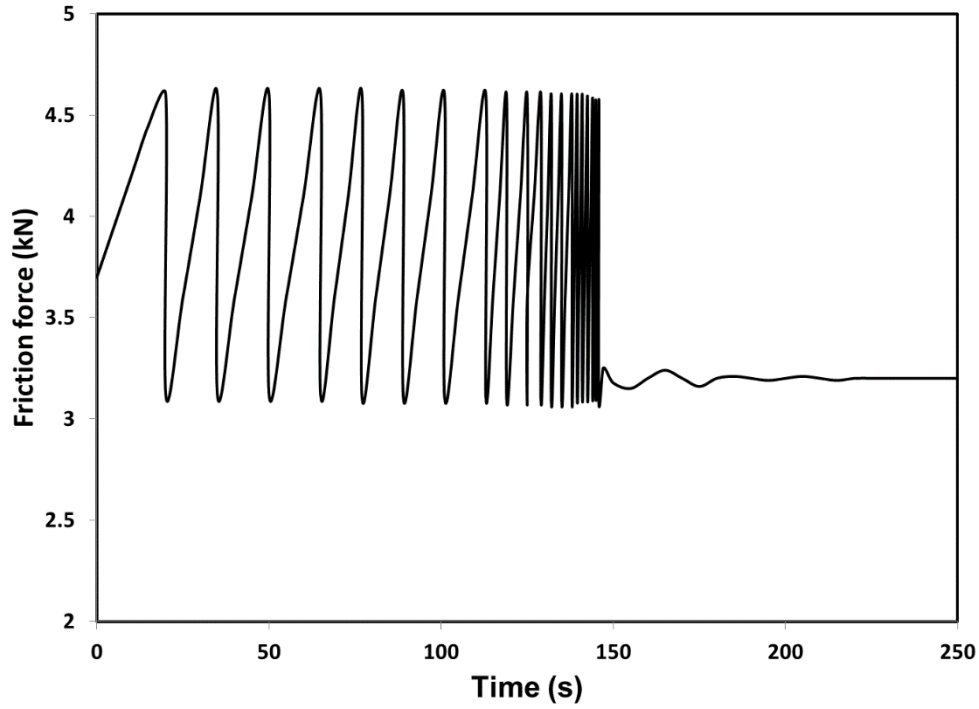


**Figure 5.6: Average friction force versus time**

## 5.5. Conclusion

Simple mechanical instabilities can result in a stick–slip motion with a certain pattern, which can result in “micro-slip” waves propagating along the frictional interface and be observed as friction reduction. Here, we presented a model which captures formation of overall slip based on evolution of different local slips. As the tangential force increases, the size of the stick region decreases until overall sliding begins. We showed how these local slips make instable regions which can finally lead to stable, self-organized region.

## Chapter 6

### Contact angle hysteresis as a solid-liquid energy dissipation

#### 6.1. Objective

In this chapter, we use Cellular Potts Model to study contact angle (CA) hysteresis as an example of solid-liquid energy dissipation. CA hysteresis is related to the more general phenomenon known as adhesion hysteresis which is observed also during a solid-solid contact. When two solid surfaces come in contact, the energy required to separate them is always greater than the energy gained by bringing them together, and thus the loading-unloading cycle is a thermodynamically irreversible dissipative process. A model was suggested by Nosonovsky (2007) which relates the origin of solid-liquid friction the adhesion hysteresis and surface roughness. Here, we simulate CA hysteresis for a droplet over the tilted patterned surface, and a bubble placed under the surface immersed in liquid. We discuss dependency of CA hysteresis on the surface structure and other parameters. We show how this analysis can allow decoupling of the 1D (pinning of the triple line) and 2D effects (adhesion hysteresis in the contact area) and obtain new insights on the nature of CA hysteresis.

#### 6.2. Numerical modeling of wetting

Superhydrophobicity has drawn attention of researchers in recent years because of the need to design non-wetting, non-sticky, antifouling, ice-phobic, and self-cleaning surfaces (Nosonovsky & Rohatgi, 2011; Shirtcliffe et al., 2010; Bhushan and Nosonovsky, 2010; Boinovich & Emelyanenko, 2009; Tadmor et al., 2009; Kietzig et al., 2009; Tadmor, 2008;

Bouteau, et al., 2008; Bormashenko et al., 2007, 2006; Choi and C-J. Kim, 2006; Ma and R.M. Hill, 2006; Li and A. Amirfazli, 2006; Krupenkin, 2004; Furstner, 2005; Patankar, 2004; Herminghaus, 2000). Significant progress has been made in design, synthesis and characterization of functional superhydrophobic surfaces (Hejazi & Nosonovsky, 2012a; Nosonovsky & Hejazi, 2011; Feng & Jiang, 2006; Huang, et al., 2005).

Besides experimental studies, analytical models of wetting of rough surfaces have been developed. The concept of the water contact angle (CA) was introduced by Young (1805) along with the concept of the surface tensions of the solid-vapor ( $\gamma_{SV}$ ), solid-liquid ( $\gamma_{SL}$ ), and liquid-vapor ( $\gamma_{LV}$ ) interfaces. Wenzel (1936) and Cassie & Baxter (1944) proposed two classical models to modify the Young equation for rough or heterogeneous surfaces in the case of the solid-water and composite solid-air-water interface. Their models have been expanded for various cases of patterned and random surfaces. In general, these models can be called macroscopic, since they treat both fluid and solid as continuum media which satisfy the equations of hydrodynamics and elasticity, and deal with the macroscale thermodynamic parameters such as the contact angle (CA). However, many interactions related to wetting of rough surfaces occur at the nanoscale (molecular scale) and the microscale (mesoscale). In order to study these interactions, numerical simulations are typically used.

In addition to static wetting and equilibrium CA, CA hysteresis has been subject of many investigations (e.g., Hejazi & Nosonovsky, 2012b; Biben & Joly, 2009; Pierce et al., 2008; Bouteau et. al., 2008). Even in the quasi-static case of low velocity, the value of the CA is not unique due to CA hysteresis, and it depends on whether water is added (the advancing CA) or recedes (the receding CA). This is because solid surfaces are often rough or chemically heterogeneous and because it may take too much time to attain the true equilibrium state which

corresponds to the equilibrium CA. Furthermore, due to molecular reorientation, surface deformation, dissolving, chemical and other interactions, water advancing is not reversible, and there is asymmetry between wetting and dewetting. In particular, due to this asymmetry, wetting of water droplets and air bubbles is different. In addition, so-called adhesion hysteresis exists making the energy of bringing surfaces together different from the energy needed to separate them. As a result, many interactions, both at the liquid volume, solid-liquid surface, and solid-liquid-air triple line are responsible for CA hysteresis and it is difficult to separate them and to tell which effect is dominant. To get better understanding of the role of these effects, numerical simulation can be helpful.

So far different analytical and numerical models have been suggested to explain wetting and estimate the CA. Among those are the models based on the molecular-kinetic theory (MKT) (Blake, 1993; Blake & Haynes, 1969). This theory neglects hydrodynamic aspects of flow and the viscous dissipation, and links macroscopic behavior of the triple line, and the CA, with microscopic quantities like the frequency ( $k$ ) and displacement ( $\lambda$ ) of movement of individual molecules in the vicinity of the triple line (Blake et al., 1997). While good agreement was obtained with experiment for the MKT models (Hayes, 1994), they used some phenomenological parameters, which could be obtained only by curve fitting (Blake et al., 1997).

Hydrodynamic (HD) models based on lubrication theory (e.g. Cox, 1986) are another significant approach in studying of wetting dynamics. The HD models, unlike MKT, describe dynamics of wetting from a continuum viewpoint by considering the balance between capillary and viscous forces (Dussan et al., 1991). Shikhmurzaev (1997) extended the approach by exploiting non-equilibrium thermodynamics to describe dissipation due to the interfacial creation and destruction processes occurring as the triple line moves along the solid surface.

Phenomenological phase field (PF) models have also been used to study CA hysteresis (Vedantam and Panchagnula, 2007).

Molecular dynamics (MD) simulation was applied to explore the details of wetting at the molecular scale. Alder & Wainwright (1957) described the solution of the classical equations of motion (Newton's equations) for a set of molecules. While the first MD studies of the static CA was done by Saville (1977), it's after the works of Koplik et al. (1989 & 1989) and Thompson et al. (1989 & 1993) that the approach has been used extensively for simulation of wetting. However, most practical MD simulations are still restricted to small systems of the order of tens of nanometers and short times of the order of a few nanoseconds. Scale-dependency of wetting parameters such as the CA, also, makes the practical application of the results of MD simulations questionable.

Usually it is very difficult to deduce macroscale parameters (such as the CA) directly from the molecular scale properties. This is because many important interactions occur at the mesoscale (with the typical length on the order of microns) involving surface roughness, heterogeneity, material domains and grains, etc. Therefore, the emphasis of the simulation activity should be on the mesoscale. The appropriate methods for mesoscale materials modeling include Monte Carlo (MC) simulation, Cellular Automata and others (Nosonovsky and Esche, 2008, 2009).

In this chapter, we use Cellular Potts model (CPM) to investigate CA hysteresis and decouple 1D (triple line) and 2D (contact area) effects on that. Cellular Potts model (Graner, 1992; Glazier & Graner, 1993) is a lattice-based computational modeling method to simulate the behavior of cellular structures, and has been applied to problems where the dynamics is driven by energy minimization arising from interfacial tensions between different media. In recent



years, the model has been used in different studies to simulate biological tissues (Glazier & Graner, 1993), grain growth (Glazier, 1990), foam structure (Jiang et al., 1990), coarsening (Glazier et al., 1990), and drainage (Jiang et al., 1990), fluid flow and reaction-advection-diffusion systems (Dan et al., 2005). Messenger et al. (1991) used the Potts model to study the wetting of the interface between two ordered phases by the disordered phase and we established the validity of the Antonov's rule. More recently, De Oliveira et al. (2011) suggested using the model for simulation of superhydrophobic behavior of liquid droplets.

The strength of the CPM in the study of wetting is that, unlike MD, it does not require the detailed interaction potentials among the molecules. It can deal with the processes at the mesoscopic level, while at the same time simulating the macroscopic behavior of the system as a whole. Thus, the CPM simulation can serve as a numerical experiment with a level of control that would be very difficult or even impossible to achieve in a physical experiment. This provides further insights on how different physical mechanisms and parameters influence CA hysteresis of droplets and bubbles.

### **6.3. Contact angle hysteresis**

Since the concept of the CA was introduced, it was realized that this single parameter cannot completely characterize wetting. Furthermore, there is no unique value of the CA, but it can have a range of values  $\theta_{rec} \leq \theta \leq \theta_{adv}$ , where  $\theta_{rec}$  and  $\theta_{adv}$  denote the receding and advancing CAs when liquid is removed or added, respectively. The difference between the advancing and receding CA is called CA hysteresis. The phenomenon of CA hysteresis on chemically heterogeneous surface was apparently noticed for the first time by A. Pockels (1891) and then investigated by Ablett (1923), Frenkel (1948), Bartell and J.W. Shepard (1953), Furmidge

(1962), Johnson and Dettre (1964) and others. However, most attention was paid to CA hysteresis after the discovery of the superhydrophobicity and the Lotus effect.

Superhydrophobicity is the ability of some surfaces to have very high water CA ( $>150^\circ$ ) and low CA hysteresis. The Lotus effect is characterized by surface roughness induced superhydrophobicity and self-cleaning. The field of superhydrophobicity is relatively new, although the phenomenon has been discussed in the literature since the 1930s, by Adam and other surface scientists of the time (Adam et al., 1925). Wenzel (1936) was the first who investigated wetting of rough surfaces. Using simple arguments related to the surface tension force equilibrium, he derived an equation for the water contact angle (CA) with a rough surface. The same equation was derived, independently, by Derjaguin (1946) and Good (1952), using thermodynamic arguments and a very powerful concept of the “disjoining pressure” (Boinovich & Emelyanenko, 2011). Cassie and Baxter (1944) studied wetting of a surface composed of two fractions. The Wenzel and Cassie-Baxter equations correspond to two distinct wetting regimes. The Cassie wetting regime with air pockets trapped between the solid and liquid is desirable for superhydrophobicity. It is recognized that the Cassie regime is needed to attain small CA hysteresis and superhydrophobicity.

CA hysteresis can be measured also on a tilted surface, although it is recognized that the values measured in this way do not always provide true values of the advancing and receding angles (Whyman et al., 2008; Krasovitski & Marmur, 2004). There are several theories explaining CA hysteresis. One theory attributes CA hysteresis to pinning of the triple line by sharp asperities at the surface (Nosonovsky, 2007). Two surfaces come together at a sharp edge, so the value of the CA is not unique at the edge, being in the range of values from the minimum value (corresponding to the slope on one side of the edge) to the maximum value (corresponding

to the slope on the other of the edge). When liquid front advances, the triple line will be pinned at the edge until the CA reaches its maximum value. Similarly, when liquid recedes, the triple line is pinned until the CA reaches its minimum value. Therefore, varying surface slope results in CA hysteresis (Hejazi & Nosonovsky, 2012b).

In a similar manner, chemical heterogeneity or contamination leads to CA hysteresis. If a surface is composed of spots with different surface energies, water will cover the spots with higher energy first and leave them last, effectively resulting in CA hysteresis. It has been discussed (Hejazi & Nosonovsky, 2012b) that CA hysteresis is equal to dissipated energy during the motion of a droplet. This dissipation can occur either in the bulk of the liquid, at the solid-liquid interface or at the triple line. The bulk dissipation (3D) is mostly due to the viscosity and it can be eliminated in the quasi-static limit of low velocity, however, the interfacial (2D) and triple line (1D) dissipation cannot be eliminated completely and both contribute to CA hysteresis. Therefore, CA hysteresis involves a term proportional to the contact area and a term proportional to the length of the triple line. Despite many studies on the topic (Hejazi & Nosonovsky, 2012b; Biben & Joly, 2009; Pierce et al., 2008; Bouteau et. al., 2008), more advanced modeling is needed to separate of these effects and investigate how different parameters such as surface roughness, heterogeneity and drop/bubble size affect CA hysteresis.

#### **6.4. The Cellular Potts Model**

The Cellular Potts Model (CPM) is a method to model mesoscale phenomenon using statistical techniques. The simulation domain is discretized using a lattice, as shown in **Fig. 6.1**. Each lattice site has a spin. Contiguous simply-connected lattice sites with the same spin constitute a generalized cell. A generalized cell can be a bubble, a biological cell, or a metal grain. The configuration of the simulation domain evolves one lattice site at a time based on a set

of probabilistic rules. Configuration changes are based on a Hamiltonian function that is used of calculating the probability of accepting configuration changes (Graner & Glazer, 1992). The CPM Hamiltonian is given by:

$$H = H_j + H_s + H_v + H_o \quad (6.1)$$

where  $H_j$  is the adhesive term,  $H_v$  is the volume restriction term,  $H_s$  is the surface area restriction term and  $H_o$  is the potential energy term. The adhesive term is given by:

$$H_j = \sum_{i,j \text{ neighbors}} J(\tau(\sigma(i)), \tau(\sigma(j)))(1 - \delta(\sigma(i), \sigma(j))) \quad (6.2)$$

Here  $J(\tau(\sigma(i)), \tau(\sigma(j)))$  is the interfacial energy term between cells of type  $\tau$  encompassing neighboring lattice sites  $i, j$ , and  $\sigma(i)$  is the spin of lattice site  $i$ . The summation is over a pre-specified radius centered on the lattice site  $i$ . The volume restriction term is given by:

$$H_v = \sum_{\sigma} \lambda_{\text{volume}} [V(\sigma) - V_{\text{target}}(\sigma)]^2 \quad (6.3)$$

where  $V(\sigma(i))$  is the current volume of the cell encompassing the lattice site  $i$ ,  $V_{\text{target}}(\sigma(i))$  is the target volume of the same cell,  $\lambda_{\text{volume}}$  is the Lagrange multiplier for the volume term. The surface area restriction term is given by:

$$H_s = \sum_{\sigma} \lambda_{\text{surface}} [S(\sigma) - S_{\text{target}}(\sigma)]^2 \quad (6.4)$$

where  $S(\sigma(i))$  is the current surface area of the cell encompassing the lattice site  $i$ ,  $S_{\text{target}}(\sigma(i))$  is the target surface area of the same cell,  $\lambda_{\text{volume}}$  is the Lagrange multiplier for the surface area restriction term. The potential energy term is given by:

$$H_o = \sum_i \vec{F} \bullet \vec{R}(i) \quad (6.5)$$

where  $\vec{F}$  is a uniform potential field, and  $\vec{R}(i)$  is the position of the lattice with respect to the reference frame.

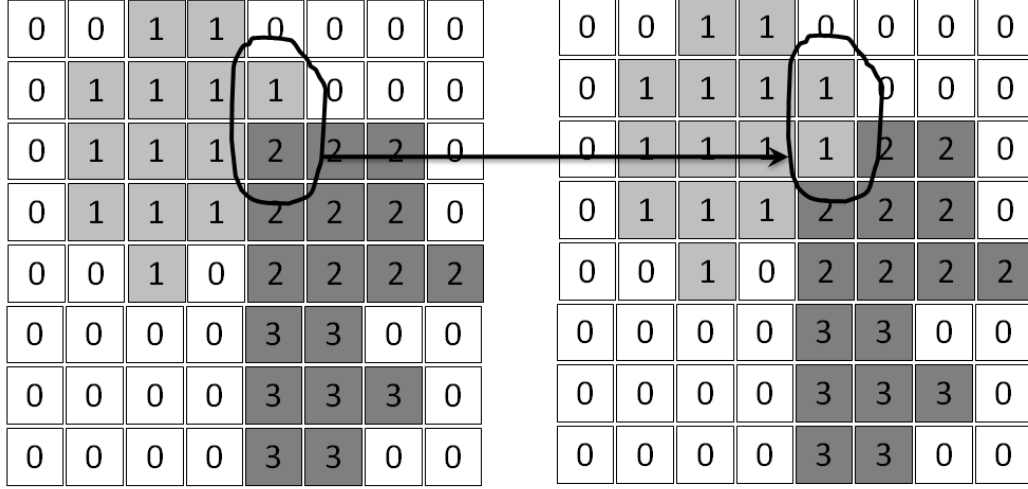


**Figure 6.1.** Schematic of a 2D lattice and a spin flipping attempt in CPM.

Monte Carlo simulations of Potts models have traditionally used local algorithms such as that of Metropolis (Graner & Glazer, 1992). A lattice site  $i$  is chosen at random and a new trial spin is also chosen at random from one of its pre-defined neighborhood lattice sites  $j$  (usually the immediate Moore neighborhood) to test local boundary energy minimization (**Fig. 6.1**). The probability  $P(\sigma(i) \rightarrow \sigma(j))$  of accepting such a reassignment is (Graner & Glazer, 1992):

$$P = \begin{cases} 1 & \Delta H \leq 0 \\ e^{-\Delta H/kT} & \Delta H > 0 \end{cases} \quad (6.6)$$

Where  $\Delta H$  is variation in energy,  $T$  is fluctuations, and  $k$  is Boltzmann constant. Simulation time is measured by Monte Carlo steps (MCS), where one MCS corresponds to as many spin flip attempts as the total number of lattice sites  $N$ . The updating rules are exactly the same for each lattice site and the evolution is continuous.

### 6.5. The Cellular Potts Modeling of wetting

To study CA hysteresis with CPM, we simulate two different cases: first, a droplet moving along a tilted solid surface, second, bubble placed on the solid surface immersed in liquid. Although, in principle, it is expected that the bubble and the droplet demonstrate same CA hysteresis (dealing with the same solid-liquid-gas system), experimental study show that the values can be quite different (Hejazi & Nosonovsky, 2012). The asymmetry between the droplets and the bubbles is attributed to the compressibility of gas bubbles (as opposed to almost incompressible water droplets), interactions at the solid-water interface, and even to the fractal structure of the interface (Letellier et al., 2007).

Consider the case of small droplet on a plane surface with in equilibrium with the gas phase, and where a spherical gas-liquid interface has a surface energy  $\gamma$  without gravity or line tension effects. The conditions for mechanical equilibrium can be determined by minimizing Gibbs free energy

$$dE = -\Delta P dV + \gamma dA_{lg} + (w_{ls} - w_{gs})dA_{ls} \quad (6.7)$$

where  $P$  is pressure,  $V$  and  $A$  are volume and surface area, and  $w$  represents work of cohesion between two different surfaces. We can say that Energy equation consists of pressure and surface energy terms. To present total energy in terms of Hamiltonian,  $H_J$  acts as a surface energy term, and  $H_J$  (or  $H_s$ , depends of the type of the problem) represent pressure term.

As it was pointed out, The CPM minimizes total surface energy and essentially solves the minimal surface equations for a lattice. Our model consists of a 2D lattice with the dimensions of  $L^2 = 500 \times 250$  sites, and three different media:  $\sigma = 0$  for vapor,  $\sigma = 1$  for liquid and  $\sigma = 2$  for solid. The adhesive term of Hamiltonian,  $H_J$ , as defined in Eq. 2, is based on the interaction between neighboring cells, and involves interfacial energies. When neighboring cells belong to

the same medium, we have  $J(\tau, \tau') = 0$ ; which means the Potts energy imposes that there is an interfacial energy only between cells of different media, i.e., between neighboring liquid-vapor, liquid-solid, and vapor-solid cells.

The volume restriction term,  $H_v$ , in Eq. 7.3 is responsible for the compressibility of the medium. When spin flip is attempted, one cell will increase its volume and another cell will decrease. Thus the overall energy of the system may change. Volume constraint essentially ensures that cells maintain the volume close to its target volume. In simulations, for the liquid medium, the value of  $\lambda_{volume} = 1$ , and target volume for each cell was its initial volume. Although, since we did not require imposing any prior constraint on surfaces, we set the value of  $\lambda_{surface} = 0$ . Then, solution will seek for the shape of the liquid-vapor interface with minimizing Hamiltonian, without any intrinsic constraint.

Moreover, to include gravity effect on the droplet (or on the bubble), Eq. 6.4 was written in the following form:

$$H_o = \sum_i gh(i) \quad (6.8)$$

here  $g$  is the acceleration due to gravity, and  $h(i)$  is the height of each cell with respect to a reference frame.  $H_o$  was only calculated for liquid medium.

The range of interactions for each site in computing the adhesive term in the Hamiltonian was specified to be fifth Moore neighbor. We observed that increasing this range to 6 or 7 neighbors did not affect the final results. Since all values in CPM are dimensionless, we were free to set different parameters as means to fix the length scale and time scale of the simulations in the order of micron and millisecond, respectively. For example, we set 1 pixel to 20  $\mu\text{m}$  and 1 MCS to 10 ms; then, other parameters like gravity, surface energy, etc. can be found based on

their actual relative values. In this way, our choice of parameters is somewhat arbitrary, since after experiments, and comparison with simulation results, we can set their exact values.

The initial configuration for droplet on the homogenous solid surface is shown in **Fig. 6.2** for  $f_{SL} = 1$ , where  $f_{SL}$  (solid-liquid fraction) is defined as the ratio of solid-liquid length to whole contact length. We changed structure of solid surface in next simulations to investigate the effect of solid-liquid fraction, slope of surface, and its material (surface energy) on CA hysteresis. Simulations were performed using the CompuCell3D software (Cickovski et al., 2005), which is an open source modeling environment, primarily used to study cellular behavior, and was built with the C++ programming language.

The surface energies of the vapor–liquid, liquid–solid and vapor–solid interfaces were considered to be equal to 80, 110, and 70, respectively (all values are dimensionless in the CPM), i.e., in Eq. 2, we have  $J(v, l) = 80$ ,  $J(l, s) = 110$ , and  $J(v, s) = 70$ . Note that, according Young's equation, only the ratios of the surface energies matter for determining of the CA, rather than their absolute dimensional values. Substituting the dimensionless values in Young's equation we will have

$$\theta = \cos^{-1} \left[ \frac{J(v, s) - J(l, s)}{J(v, l)} \right] = \cos^{-1} \left[ \frac{70 - 110}{80} \right] = 120^\circ \quad (6.9)$$

and to verify results by CPM, we obtained the same value with simulation of the droplet on a smooth surface, without considering gravity.

Looking into Eq. 7.1, we can say it is the gravity term in the Hamiltonian responsible for the weight of the droplet (or buoyancy of a bubble) which results in the asymmetry between the advancing and receding angles. Physically, the system is finding a compromise shape between the lowest possible position of its center of mass and minimized surface area.



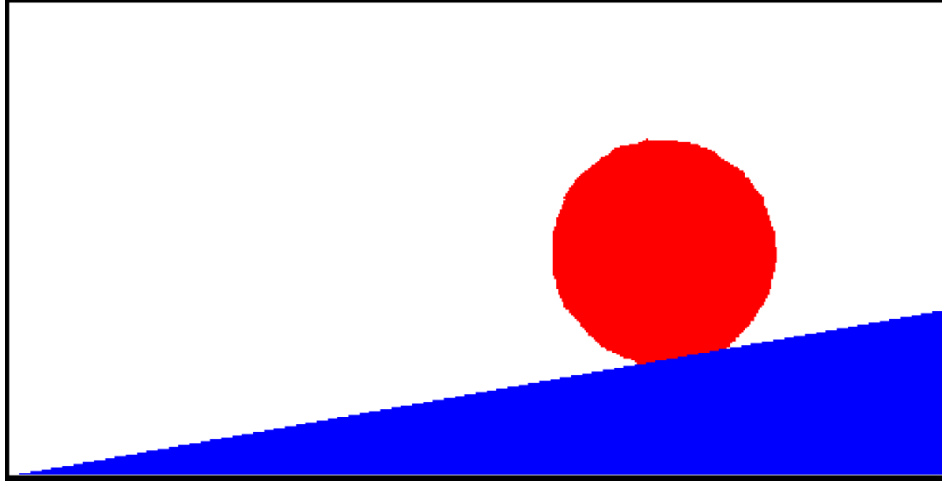


Figure 6.2. Initial configuration of simulation for droplet along a tilted homogeneous ( $f_{SL} = 1$ ) solid surface

## 6.6. Results

The slope of the tilted surface (the tilt angle) was initially set at  $10^\circ$ , and the radius of the initial circular droplet was set to 35, 50 and 60 lattice sites, in three different simulations. The simulation was performed for different values of  $f_{SL} = (0.1, 0.2, 0.4, 0.6, 0.8, \text{ and } 1.0)$ , and in each case we changed initial configuration. Values of  $f_{SL}$  and the slope enter into the simulation just as a part of the initial configuration. The influence of the solid-liquid fraction on the CA hysteresis is presented in **Fig. 6.3**. The values of the CA and its hysteresis were obtained using *DropSnake* plug-in for *ImageJ* software (Stalder et al., 2006). For all three different droplets, with decreasing  $f_{SL}$ , the CA hysteresis decreased, and around  $f_{SL} = 0.2$ , it reached very low values ( $3.28^\circ$ ,  $2.13^\circ$  and  $1.5^\circ$ , for  $R=35, 50$  and  $60$ , respectively). For lower values ( $f_{SL} = 0.1$ ), an increase of CA hysteresis was observed. This is apparently because two different factors contribute to CA hysteresis. First, for large contact areas the droplet diverges from the spherical shape making asymmetry more pronounced and, thus, larger CA hysteresis, as observed visually

from the modeling results. Second, for small solid-liquid fractions, contact area acts as large roughness pinning the droplet and thus leading to hysteresis. The second effect fades out quickly with increasing  $0 \leq f \leq 0.2$ , so the minimum CA hysteresis is at around  $f=0.2$ . The same effect (with the minimum at  $f=0.2$ ) was also reported by De Oliveira et al. (2011) who attributed it to the possible Cassie/Wenzel wetting transition.

The evolution of advancing and receding contact angles as a function of the surface energy of solid-liquid for homogeneous interface ( $f_{SL} = 1$ ) is presented in **Fig. 6.4**. For this comparison, all other parameters were kept constant, and the same as the ones described for previous simulations. An increase of CA hysteresis (from  $7.15^\circ$  to  $18.33^\circ$ ) is noticeable with increasing surface energy (from  $J(l, s) = 80$  to  $J(l, s) = 140$ ).

The effect of droplet size on the advancing and receding contact angles was investigated as well. **Fig. 6.5** compares these two parameters for different radii of initial circular droplet ranging from 35 to 60 lattice sites. While advancing CA increased (from  $121.46^\circ$  to  $124.08^\circ$ ) with increasing droplet size, there was little decrease in receding CA (from  $113.15^\circ$  at  $R = 60$  to  $109.5^\circ$  at  $R = 35$  sites). This leads to increasing CA hysteresis with droplet size, which can be attributed to gravity effect.

In order to investigate the effect of the compressibility and separate the triple line and the contact area effects on CA hysteresis, we compared CA hysteresis for droplets and bubbles on the same surface. We considered the surface energies of the gas-liquid, liquid-solid and gas-solid to be equal to 80, 110, and 70, respectively. **Fig. 6.6** shows advancing and receding CAs of droplet for different tilt angles (TA), i.e., 0, 10, 45, 75 and 90 degrees after 20000 MCS. The results show that CA hysteresis increased with large tilt angles and reached its maximum value ( $31^\circ$ ) at the  $90^\circ$  tilt (a vertical surface). The similar results were obtained for bubble and are

shown in **Fig. 6.7**. In this case, for tilt angles greater than  $40^\circ$ , the bubble detached from the solid. The reason that the water droplet remained attached to the solid even at the tilt angle of  $90^\circ$ , can be attributed to the fact that droplet-solid adhesion was stronger since the solid-water interface (2D contact area) component was present in addition to the triple line (1D) component, while air bubble did not have contact area adhesion. **Fig. 6.8** compares CA hysteresis in these two systems. It is observed that CA hysteresis for a bubble is larger than that for a droplet. The difference is attributed to the fact that the gas bubble is compressible and that no interaction occurs between the gas and the solid at the bubble-solid contact area.

In order to verify simulation results, we measured experimentally hysteresis for water droplets and air bubbles for different sizes of droplet/bubble. The experiments on droplet were done on concrete  $\text{TiO}_2$  coated tile, and on bubble on Aluminum sample. We measured the arithmetic mean value of surface roughness,  $R_a$ , of the two samples by a profilometer (Mitutoyo SurfTest, 40) which were found to be  $3.286\ \mu\text{m}$ , and  $0.763\ \mu\text{m}$  for tile and Aluminum sample, respectively. For all experiments, the droplets and air bubbles of different volume were deposited on the solid surface. The advancing and receding CAs for samples were measured by a standard ramé-hart goniometer/tensiometer, model 250, for different tilt angles. The results are presented in **Fig. 6.9**. **Fig 6.9a** shows effect of droplet size on CA hysteresis for three different tilt angles. Similar to the simulation results, for large droplets, large value of CA hysteresis was observed, i.e., with increasing droplet volume from around  $8\ \mu\text{m}$  to nearly  $60\ \mu\text{m}$ , CA hysteresis increases from  $4.09^\circ$  to  $15.76^\circ$  (for  $\text{TA}=10^\circ$ ),  $6.80^\circ$  to  $27.89^\circ$  (for  $\text{TA}=20^\circ$ ) and  $9.86^\circ$  to  $34.13^\circ$  (for  $\text{TA}=30^\circ$ ). The same phenomenon can also be seen for air bubbles (**Fig 6.9b**), i.e., with increasing bubble volume from around  $7\ \mu\text{m}$  to nearly  $25\ \mu\text{m}$ , CA hysteresis increases from  $4.5^\circ$  to  $14.98^\circ$  (for  $\text{TA}=10^\circ$ ), and  $6.95^\circ$  to  $20.08^\circ$  (for  $\text{TA}=20^\circ$ ). In this case, depends on bubble size, for tilt

angles larger than  $20^\circ$ , bubbles detached from the solid surface. This detachment, also, observed by increasing size of bubbles, as well. These experimental observations confirm the argument made above about compressibility of the gas bubbles and no interaction occurrence between the gas and the solid at the bubble-solid contact area.

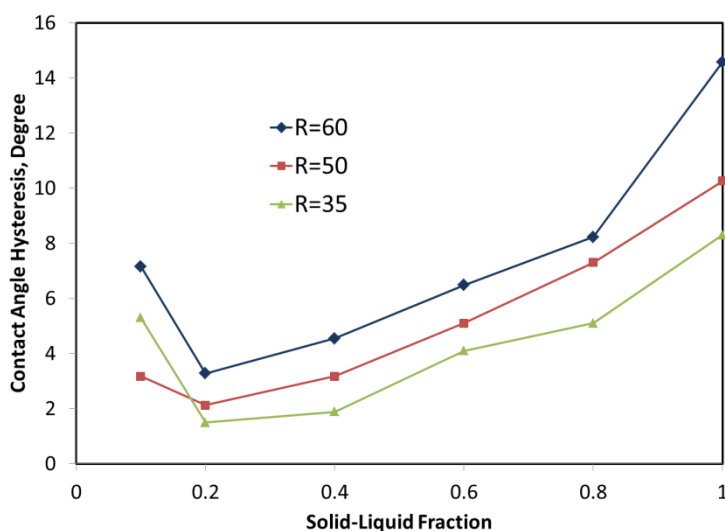


**Figure 6.3. Contact angle hysteresis versus solid-liquid fraction for droplet on the tilted surface; for three different drop diameters**

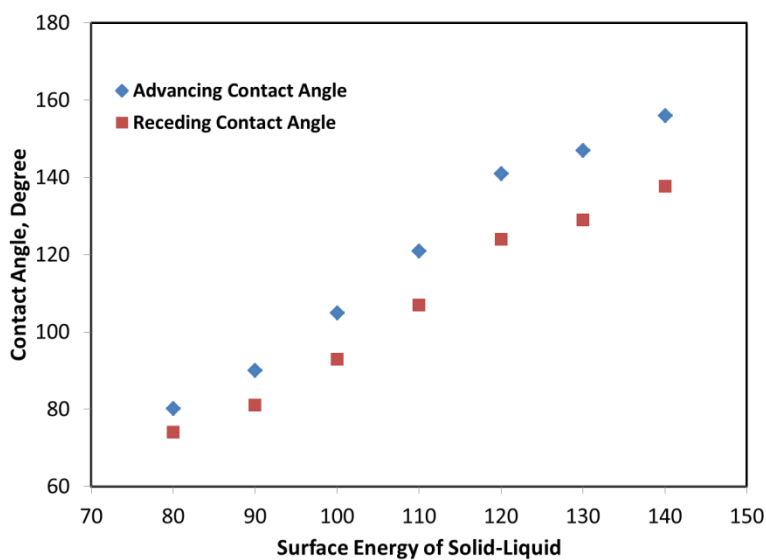


**Figure 6.4. Advancing and receding contact angles for different surface energies of solid-liquid**

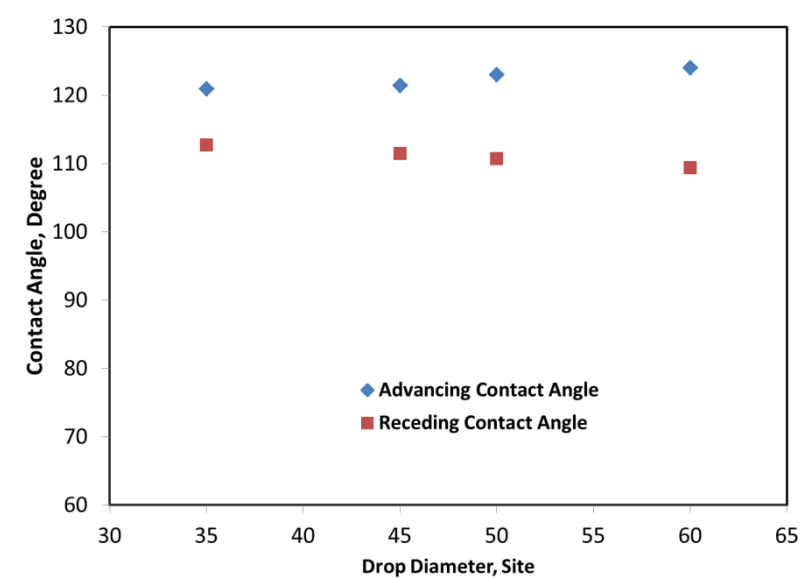


Figure 6.5. Advancing and receding contact angles for different drop diameters

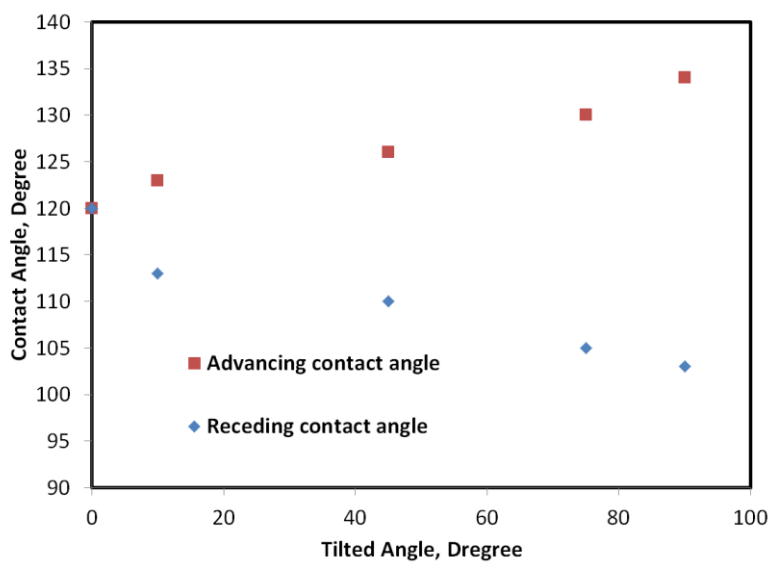


Figure 6.6. Advancing and receding contact angles versus titled angle for a droplet on the tilted surface

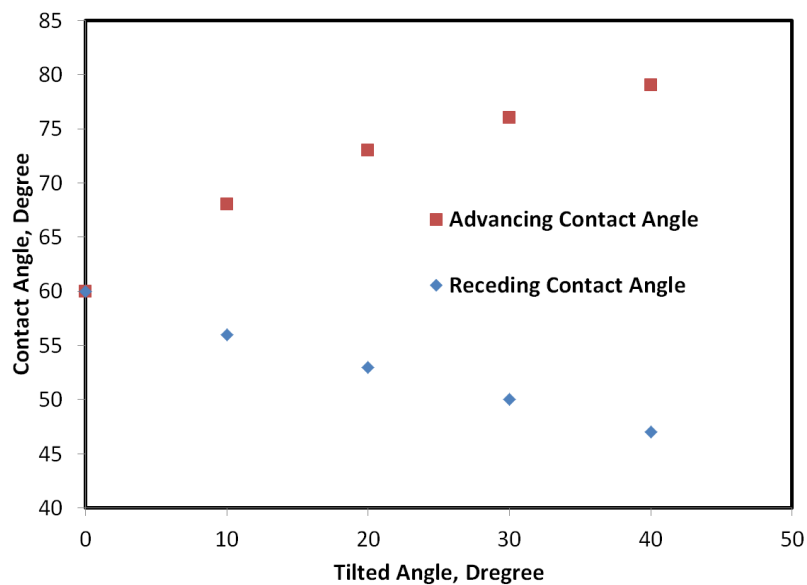


Figure 6.7. Advancing and receding contact angles versus titled angle for a bubble submerged in liquid

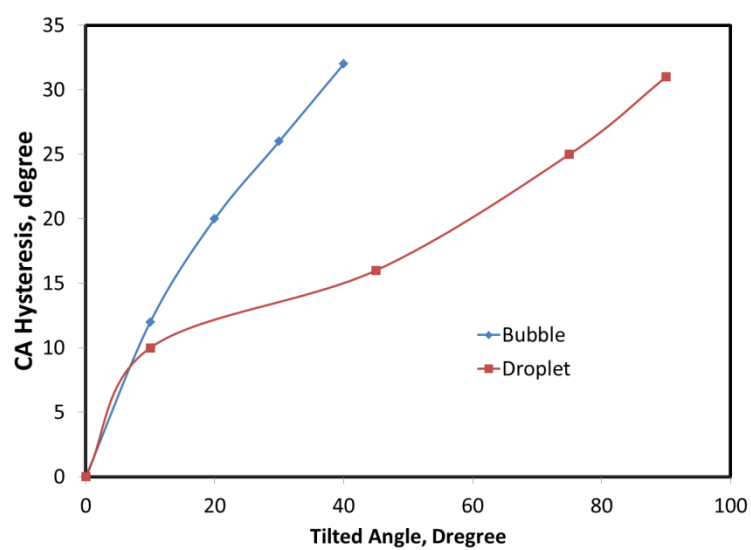
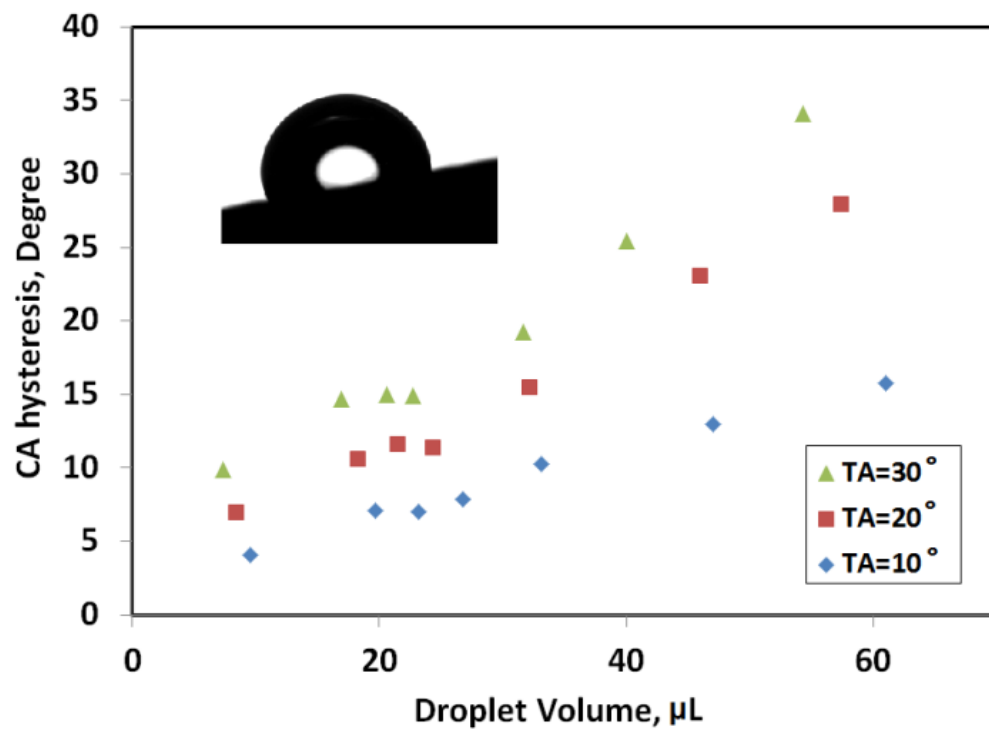
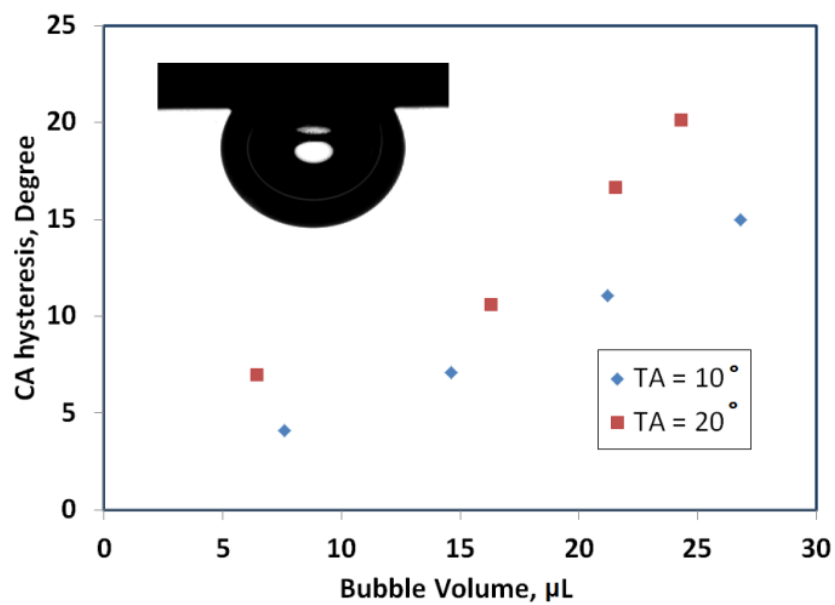


Figure 6.8. Comparison of CA hysteresis for bubbles and droplet of the same surface energies



(a)



(b)

Figure 6.9. CA hysteresis obtained by experiment for (a) different droplet sizes on concrete TiO<sub>2</sub> coated tile, and for bubble (b) different bubble sizes on Al sample, for different tilt angles (TA)

## 6.7. Conclusion

We used cellular Potts model (CPM) to study CA hysteresis for a droplet moving along a tilted solid surface, and bubble placed on the solid surface immersed in liquid. CPM minimizes total surface energy of the solid-liquid-vapor system, and shows how system reaches its single value of the contact angle. The dependency of CA hysteresis on surface structure is discussed based on the simulation results. We observed how CA hysteresis decreases in heterogeneous interfaces with decreasing the solid-liquid fraction, and reaches its minimum value. The effects of solid-liquid surface energy and droplet size on advancing and receding contact angle were also discussed. We compared the dependency of CA hysteresis on the titled angle for bubble and droplet. The value of hysteresis depends on the interactions in the solid-liquid contact area and at the triple line. Although the solid-liquid-vapor triple line is the same for bubbles and droplets, the adhesion of droplets was much stronger, which points to the role of the 2D interface and bubble compressibility.



## Chapter 7

### Final conclusions

In this thesis, we investigated several problems of friction-induced vibrations, instabilities and self-organization. While, in most cases, irreversible dissipation and degradation occur at the frictional interface, in certain situations, self-organizing behavior might take place. This is because friction is a non-equilibrium and irreversible process. The self-organization is usually beneficial for friction and wear reduction because the entropy production rate is minimized in a self-organized state. In first chapter, we discussed leading to the self-organization occurs through the destabilization of the steady-state (stationary) sliding. Different types of instabilities in frictional interface were also discussed: thermoelastic instabilities, instabilities due to the velocity dependence of the coefficient of friction, destabilization of interface elastic waves, thermal expansion and the effect of wear.

We studied practical engineering cases that might lead to self-organization. These are include the instability due to the temperature-dependency of the coefficient of friction, the transient process of frictional running-in, frictional Turing systems, the stick-and-slip phenomenon, and, finally, contact angle (CA) hysteresis as an example of solid-liquid friction and dissipation. In all these cases, motivation was to start from fundamental thermodynamical and mechanical concepts, and to end up with solutions can be implemented in optimized design, synthesis, and characterization of different materials and tribosystems to reduce wear and other degrading effects of friction.

In chapter 2, we studied the stability of frictional sliding with the temperature-dependent coefficient of friction. We presented a mathematical model and formulated the stability condition governing whether the perturbations imposed on the surface temperature in the frictional sliding can grow or decay depending upon the working conditions such as pressure, sliding velocity and geometry. Although it is usually ignored in most disk-pad contact models, this temperature-dependency can have a significant effect on the stability. The temperature-dependency of the coefficient of friction leads to the formation of hot and cold spots on the disks. The number of these spots or domains depends upon the thermal diffusivity of the disk material and affects the reproducibility of the brake test results. Larger number of spots is desirable for better reproducibility. It can be achieved either by decreasing of the thermal diffusivity, by increasing the disk area, or, alternatively, by texturing the surface and dividing it artificially into domains. Future researches are needed to show how combined effects of instabilities discussed in this chapter and other “well-known” instabilities could be investigated and used for much improved design and selection of materials.

In chapter 3, we developed a theoretical approach to study running-in period as an example of friction-induced self-organization. We conclude that friction, due to non-linear effects, can lead to a less random surface profile, and we proposed Shannon entropy as a measure of profile self-organization. The adjustment of surface roughness to an equilibrium value during the running-in transient process leads to the minimization of friction and wear and it was investigated by considering a feedback loop due to the coupling of two processes or mechanisms (in our example, adhesion and deformation). We found experimental evidences for our theoretical considerations. We observed that how Shannon entropy as a characteristic of a rough surface profile which quantifies the degree of orderliness of the self-organized system decreased

during running-in period, indicating to reach more smother and more ordered surface profile. What underlines findings of this chapter is that with better control of short and transient running-in stage, we could achieve operation of mechanical system with less degradation and deterioration. This needs to be done by investigation of more detailed interactions of rheological parameters with mechanical effects and chemical reactions.

In chapter 4, we conclude that the evolution of reaction-diffusion system can describe the formation of certain types of friction-induced interfacial patterns. These patterns can form at the sliding interface due to the processes of mass transfer (diffusion and wear), heat transfer and various tribochemical reactions. On the other hand, existing experimental data suggest that in-situ formation of tribofilms due to a variety of friction-induced chemical reactions (such as boric acid formation, oxidation, and selective transfer of Cu ions from the bulk to the interface) or wear can result in the formation of interfacial patterns (islands or honeycomb type domains). This pattern formation can be attributed to the Turing systems. We suggest that understanding of how these self-organized patterns are formed can be beneficial for optimized design of composite tribomaterials.

In chapter 5, we discussed how simple mechanical instabilities can result in a stick-slip motion with a certain pattern, which can result in “micro-slip” waves propagating along the frictional interface and be observed as friction reduction. Here, we presented a model which captures formation of overall slip based on evolution of different local slips. As the tangential force increases, the size of the stick region decreases until overall sliding begins. We showed how these local slips make instable regions which can finally lead to stable, self-organized region.

In chapter 6, we used Cellular Potts Model to study contact angle (CA) hysteresis as an example of solid-liquid energy dissipation. CA hysteresis is related to the more general phenomenon known as adhesion hysteresis which is observed also during a solid-solid contact. When two solid surfaces come in contact, the energy required to separate them is always greater than the energy gained by bringing them together, and thus the loading-unloading cycle is a thermodynamically irreversible dissipative process. A model was suggested by Nosonovsky (2007) which relates the origin of solid-liquid friction the adhesion hysteresis and surface roughness. We used cellular Potts model (CPM) to study CA hysteresis for a droplet moving along a tilted solid surface, and bubble placed on the solid surface immersed in liquid. CPM minimizes total surface energy of the solid-liquid-vapor system, and shows how system reaches its single value of the contact angle. The dependency of CA hysteresis on surface structure is discussed based on the simulation results. We observed how CA hysteresis decreases in heterogeneous interfaces with decreasing the solid-liquid fraction, and reaches its minimum value. The effects of solid-liquid surface energy and droplet size on advancing and receding contact angle were also discussed. We compared the dependency of CA hysteresis on the titled angle for bubble and droplet. The value of hysteresis depends on the interactions in the solid-liquid contact area and at the triple line. Although the solid-liquid-vapor triple line is the same for bubbles and droplets, the adhesion of droplets was much stronger, which points to the role of the 2D interface and bubble compressibility.

In conclusion, with investigating several types of friction-induces self-organization including reaction-diffusion systems, mutual adjustment of surfaces during the running-in transient process, and stick-slip patterns, two common features of these diverse processes should be mentioned. First, they all arise from instabilities of stationary states. These instabilities can be

studied with the use of the criterion  $\delta^2\dot{S} > 0$  discussed in chapter 1. Second, these processes tend to lead to friction and wear reduction. This is in line with the minimum entropy production principle as stated in chapter 1. The property of friction and wear reduction may be beneficial for the development of novel smart self-healing, self-cleaning and self-lubricating materials, which still requires future researches, and more consideration.

## References

1. Abdel-Aal, H. A. (2006), wear and irreversible entropy generation in dry sliding, Annals of University "Dunarea De Jos" Galati, Fascicle VIII, ISSN 1221-4590, Tribology, 34-45.
2. Ablett, R. (1923), An investigation of the angle of contact between paraffin wax and water, Phil. Mag., vol. 46, p. 224.
3. Adams, G. G. (1995) Self-excited oscillations of the two elastic half-spaces sliding with a constant coefficient of friction, ASME J. Appl. Mech. 62, 867–872.
4. Adam N. K. and G. Jessop G. (1925) Angles of contact and polarity of solid surfaces, J. Chem. Soc., p. 1863.
5. Adams, G. G. (1998), Steady sliding of two elastic half-spaces with friction reduction due to interface stick-slip, ASME J. Tribol. 65, 470-475.
6. Alder B. J. and Wainwright T. E. (1957) Phase transition for a hard sphere system, J. Chem. Phys. , vol. 27, 1208–9.
7. Adler, M., Ferrante, J., Schilowitz, A., Yablon, D., Zypman, F., (2004) Self-Organized Criticality, In Nanotribology Mater. Res Soc. 782, p. 111.
8. Aizawa A., Mitsuo A., Yamamoto S., Sumitomo T. and Muraishic S. (2005) Self-lubrication mechanism via the in situ formed lubricious oxide tribofilm, Wear, 259, 1-6, 708-718.
9. Bak, P. (1996), How nature works: the science of self-organized criticality, New York, NY: Springer.
10. Barber, J.R. (1969), Thermoelastic instabilities in the sliding of conforming solids, Proc. Royal Soc. London A, 312, 381-394.
11. Bartell F. and Shepard J. (1953), Surface Roughness as Related to Hysteresis of Contact Angles, J. Phys. Chem., vol. 57, pp. 455-458.
12. Biben T. and Joly L. (2008), Wetting on Nanorough Surfaces, Phys. Rev. Lett., vol. 100, p. 186103.

13. Bhushan, B. & Nosonovsky, M (2010), The rose petal effect and the modes of superhydrophobicity, *Philos Transact A Math Phys Eng Sci*, vol. 368, no. 1929, pp. 4713-28.
14. Bhushan, B. & Nosonovsky, M. (2003), Scale effects in friction using strain gradient plasticity and dislocation-assisted sliding (microslip), *Acta Mater.* 51, 4331–4340.
15. Blake T. D., Clarke A., and Ruijter M. J. de (1997), Contact angle relaxation during droplet, *Langmuir*, vol. 13, pp. 2164–66, p. 13.
16. Blake T. D. (1993) in *Wettability*; Berg, J. C., Ed.; Marcel Dekker, New York, pp. 251-309.
17. Blake T. D. and Haynes J. (1969), Kinetics of liquidliquid displacement, *J. Colloid Interface Sci.* , vol. 30, p. 421.
18. Blau, P. J. (2006), On the nature of running-in. *Tribology international*, 38(11), 1007-1012.
19. Blau, P. J. (1989), *Friction and wear transitions of materials: Break-In, Run-In, Wear-In*; (Noyes Publications: Park Ridge, NJ, USA).
20. Boinovich L. and Emelyanenko A. (2011), Wetting and surface forces *Advances, Colloid and Interface Science*, vol. 165, pp. 60-69.
21. Boinovich L. and Emelyanenko A. (2009) *Principles of Design of Superhydrophobic Coatings by Deposition from Dispersions*, *Langmuir*, pp. 2907-2912.
22. Bormashenko E., Bormashenko Y., Stein T., Whyman G. and Pogreb R. (2007), Environmental Scanning Electron Microscopy Study of the Fine Structure of the Triple Line and Cassie–Wenzel Wetting Transition for Sessile Drops Deposited on Rough Polymer Substrates, *Langmuir*, vol. 23, no. 8, p. 4378–4382.
23. Bormashenko E., Stein T., Whyman G., Bormashenko Y. and Pogreb R. (2006) Wetting Properties of the Multiscaled Nanostructured Polymer and Metallic Superhydrophobic Surfaces, *Langmuir*, vol. 22, no. 24, p. 9982–9985.

24. Bouteau M., Cantin S., Benhabib F. and Perrot F. (2008), Sliding behavior of liquid droplets on tilted Langmuir-Blodgett surfaces, *J Colloid Interface Sci*, vol. 317, no. 1, pp. 247-54, 2008.
25. Bryant, M.D. (2009), Entropy and Dissipative Processes of Friction and Wear, *FME Transactions*, 37, 55-60.
26. Bryant, M. D., Khonsari, M. M. & Ling, F. F. (2008), On the thermodynamics of degradation, *Proc. R. Soc. A*, 464, 2001–2014. (doi:10.1098/rspa.2007.0371)
27. Buldyrev, S. V., Ferrante, J. & Zypman, F. R. (2006), Dry friction avalanches: experiments and theory, *Phys. Rev. E* 74, 066 110. (doi:10.1103/PhysRevE.74.066110)
28. Bushe, N.; Gershman, I.S.; Compatibility of Tribosystems. (2006), In *Self-Organization during Friction, Advanced Surface-Engineered Materials and Systems Design*; Fox-Rabinovich, G.S. and Totten, G.E., eds.; CRC Taylor & Francis: Boca Raton, FL, pp. 59-80.
29. Cassie A. and Baxter S. (1944), Wettability of Porous Surfaces, *Trans. Faraday Soc.*, vol. 40, pp. 546-551.
30. Choi C.-H. and Kim C.-J. (2006), Large Slip of Aqueous Liquid Flow over a Nanoengineered Superhydrophobic Surface, *Phys. Rev. Lett.*, vol. 96, no. 6, pp. 066001-4.
31. Cox, R. G., (1986) *J. Fluid Mech.* , vol. 16, p. 169–194.
32. Dai, Z., Yang, S. & Xue, Q. (2000) Thermodynamic model of fretting wear. *J. Nanjing Univ. Aeronaut. Astronaut.* 32, 125–131.
33. Dan D., Mueller C., Chen K. and Glazier J. A., (2005) *Phys. Rev. E*, vol. 72, p. 041909.
34. Derjaguin B. V. (1946), On the dependence of the contact angle on the microrelief or roughness of a wetted solid surface, *C. R. (Dokl.) Acad. Sci. URSS*, vol. 51, p. 361–364.
35. Doelling, K.L., Ling, F.F., Bryant, M.D. & Heilman, B.P. (2000), An experimental study of the correlation between wear and entropy flow in machinery components, *J. Appl. Phys.* 88, 2999-3003.
36. Dufiet V. and Boissonade J. (1991), Conventional and nonconventional Turing patterns, *J Chem Phys*, 96, 664-673.



37. Dufiet V. and Boissonade J. (1992), Numerical studies of turing patterns selection in a two-dimensional system, *Physica A*, 188, 158-171.
38. Dussan E., E. Rame and S. Garoff (1991) *J. Fluid Mech.*, vol. 230, p. 97.
39. Erdemir A, Erck RA, Robles J. (1991), Relationship of Hertzian contact pressure to friction behavior of selflubricating boric acid films, *Surf Coat Technol*; 49:435–8.
40. Erdemir A, Bindal C, Zuiker C, Savrun E. (1996), Tribology of naturally occurring boric acid films on boron carbides, *Surf Coat Technol*; 86–87:507–10.
41. Erdemir A. (2001) In: Bhushan B, editor. *Modern tribology handbook*, vol. II. Boca Raton: CRC.
42. Feng X. and L. Jiang (2006) *Advanced Materials*, vol. 18, no. 23, p. 3063–3078, 2006.
43. Fleurquin, P., Fort, H., Kornbluth, M., Sandler, R., Segall, M. & Zypman, F. (2010), Negentropy Generation and Fractality in dry Friction of Polished Surfaces, *Entropy*. 12, 480-489.
44. Frenkel Y. I., On the Behavior of Liquid Drops on a Solid Surface. 1. The Sliding of Drops on an Inclined Surface, *J. Exptl. Theoret. Phys. (USSR)*, vol. 18, p. 659, 948.
45. Fox-Rabinovich, G. S. & Totten, G. E. (eds) (2006), *Self-organization during friction*, Boca Raton, FL: CRC Press.
46. Fox-Rabinovich, G. S., Veldhuis, S. C., Kovalev, A. I., Wainstein, D. L., Gershman, I. S.,
47. R. Furstner, W. Barthlott, C. Neinhuis and P. Walzel, *Wetting and Self-Cleaning Properties of Artificial Superhydrophobic Surfaces*, *Langmuir*, vol. 21, pp. 956-961, 2005.
48. L. Furmidge C. G. (1962), *Studies at Phase Interfaces. I. The Sliding of Liquid Drops on Solid Surfaces and a Theory for Spray Retention*, *J. Colloid Science*, vol. 17 , pp. 309-324.
49. Garkunov, D. N. *Triboengineering (wear and non-deterioration)*. Moscow Agricultural Academy Press: Moscow, 2000 (in Russian).
50. Garkunov, D.N. *Scientific Discoveries in Tribotechnology*. MSHA: Moscow, 2004 (in Russian).
51. Gershman, I.S. & Bushe, N. (2006) *Elements of Thermodynamics of Self-Organization during Friction*, In *Self-Organization during Friction. Advanced Surface-Engineered*

- Materials and Systems Design; Fox-Rabinovich, G.S. and Totten, G.E., eds.; CRC Taylor & Francis: Boca Raton, FL, pp. 13-58
52. Gershman, I.S. (2006) Formation of Secondary Structures and Self-Organization Process of Tribosystems during Friction with the Collection of Electric Current. In Self-Organization during Friction. Advanced Surface-Engineered Materials and Systems Design; Fox-Rabinovich, G.S. and Totten, G.E., eds.; CRC Taylor & Francis: Boca Raton, FL, pp. 197-230.
  53. Glazier, J. A., and Graner, F. (1993) Phys. Rev. E, vol. 47, pp. 2128-2154.
  54. Glazier, J. A., Anderson, M. P. and Grest, G. S. (1990) Philosophical Magazine B, vol. 62, p. 615.
  55. Anderson, M. P. and Grest, G. S. (1990), Coarsening in the Two-Dimensional Soap Froth and the Large-Q Potts Model: A Detailed Comparison, Philosophical Magazine B, vol. 62, p. 615.
  56. Good R. J. (1952), J. Am. Chem. Soc., vol. 79, p. 5041.
  57. Graner F. and Glazier (1992) Phys. Rev. Lett., vol. 69, pp. 2013-2016.
  58. Haken, H. (1983), Synergetics. An Introduction. Nonequilibrium Phase Transitions in Physics, Chemistry and Biology. 3<sup>rd</sup> ed. Springer-Verlag: New York.
  59. Hayes, R. A. and Ralston, J. (1994), Langmuir, vol. 10, p. 340.
  60. Hejazi, V. and Nosonovsky, M. (2012a), Wetting transitions in two-, three-, and four-phase systems, Langmuir, vol. 28, no. 4, pp. 2173-2180.
  61. Hejazi, V. and Nosonovsky, M. (2012b), Contact angle hysteresis in multiphase systems, Colloid & Polymer Science, 291(2), 329-338.
  62. Herminghaus, S. (2000), Roughness-Induced Non-Wetting, Europhys. Lett., vol. 52, p. 165 – 170, 2000.

63. Herminghaus, S., Herminghaus, S., Jacobs, K., Mecke, K., Bischof, J., Fery, A., Ibn-Elhaj, M., & Schlagowski, S. (1998), Spinodal dewetting in liquid crystal and liquid metal films, *Science* 282:916.
64. Ilie, F. and Tita, C (2007), Investigation of Layers Formed Through Selective Transfer with Atomic Force Microscopy, paper presented in ROTRIB '07, 10th International Conference on Tribology, Bucharest, Romania.
65. Jiang, Y., P. J. Swart, A. Saxena, M. Asipauskas and J. A. Glazier (1999), Hysteresis and Avalanches in Two-Dimensional Foam Rheology Simulations, *Physical Review E*, vol. 59, pp. 5819-5832.
66. Jiang, Y. and Glazier, J. A. (1996), Extended Large-Q Potts Model Simulation of Foam Drainage, *Philosophical Magazine Letters*, vol. 74, pp. 119-128.
67. Johnson R. and Dettre, R. H. (1964) Contact Angle Hysteresis, in *Contact Angle, Wettability, and Adhesion* (Ed.: F. M. Fowke).
68. Kagan, E., (2010) Turing Systems, Entropy, and Kinetic Models for Self-Healing Surfaces. *Entropy*, 12, 554-569.
69. Kietzig A.-M., S. G. Hatzikiriakos and P. Englezos (2009), Patterned Superhydrophobic Metallic Surfaces, *Langmuir*, vol. 25, no. 8, p. 4821–4827.
70. Klamecki, B.E. (1980), Wear – an entropy production model, *Wear*. 58, 325-330
71. Koplik, J., Banavar, J. R. and Willemsen, J. F. (1988), Molecular dynamics of Poiseuille flow and moving contact lines, *Phys. Rev. Lett.*, vol. 60, p. 1282–85.
72. Koplik, J., Banavar, J. R. and Willemsen, J. F. (1989), Molecular dynamics of fluid flow at solid surfaces, *Phys. Fluids A*, vol. 1, p. 781–94.
73. Krasovitski B. and Marmur A. (2004), Drops Down the Hill: Theoretical Study of Limiting Contact Angles and the Hysteresis Range on a Tilted Plane, *Langmuir*, vol. 21 , pp. 3881-3885.

74. Krupenkin T., Taylor, J., Schneider, T. and Yang, S. (2004), From Rolling Ball to Complete Wetting: The Dynamic Tuning of Liquids on Nanostructured Surfaces, *Langmuir*, vol. 20, pp. 3824-3827.
75. Leppänen, T (2004) Computational Studies of Pattern Formation in Turing Systems, Dissertation for the degree of Doctor of Science in Technology, Helsinki University of Technology.
76. Lin, J. F. and Chu, H. Y. (2009) Analysis of the Bénard Cell-Like Worn Surface Type Occurred During Oil-Lubricated Sliding Contact, *Proceedings of the ASME/STLE 2009 International Joint Tribology Conference, IJTC2009*, Memphis, Tennessee, USA.
77. Lau S. P., H. Y. Yang, E. S. P. Leong and S. F. Yu (2005) *J. Phys. Chem. B*, vol. 16, no. 7746–7748, p. 109.
78. Letellier P., Mayaffre A., Turmine M. (2007), Drop size effect on contact angle explained by nonextensive thermodynamics. Young's equation revisited, *Journal of Colloid and Interface Science*, vol. 314, pp. 604–614.
79. Li W. and Amirfazli, A. (2006), A Thermodynamic Approach for Determining the Contact Angle Hysteresis for Superhydrophobic Surfaces, *J. Colloid. Interface Sci.*, vol. 292, pp. 195-201.
80. Lovell M. R., Kabir M. A., Menezes P. L., and Higgs III C. F. (2010) Influence of boric acid additive size on green lubricant performance, *Phil. Trans. R. Soc. A*, 368, 1929, 4851-4868
81. Ma M. M. and R. Hill, (2006) Superhydrophobic Surfaces, *Current Opinion in Colloid and Interface Science*, vol. 11, pp. 193-202.
82. Maegawa S. and Nakano K. (2010), Mechanism of stick-slip associated with Schallamach waves, *Wear*, 268, 924–930.
83. Mayrhofer P. H., Mitterer C., Wen J. G., Greene J. E., and Petrov I. (2005), Self-organized nanocolumnar structure in superhard TiB<sub>2</sub> thin films, *APPLIED PHYSICS LETTERS* 86, 131909.

84. Messenger A., Miracle-Sole, S., and Shlosman, S. (1991), Interfaces in the Potts model II: Antonov's rule and rigidity of the order disorder interface, *Communications in Mathematical Physics*, Volume 140, pp.275-290
85. Martins JAC, Guimaraes J, Faria LO, (1995) Dynamic surface solutions in linear elasticity and viscoelasticity with frictional boundary conditions, *ASME J Vib Acou*, 117:445–51.
86. Mayrhofer, P. H., Mitterer, C., Hultman, L. and Clemens, H. (2006), Microstructural design of hard coatings, *Progress in Materials Science*, 51, 8, 1032-1114.
87. Menezes P. L., Kishore and Kailas, Satish V (2006) Studies on friction and transfer layer using inclined scratch. In: *Tribology International*, 39 (2). pp. 175-183.
88. Mortazavi V., Wang C., Nosonovsky M., (2012), Stability of Frictional Sliding with the Coefficient of Friction depended on the Temperature, *Journal of Tribology*, 041601-7.
89. Mortazavi V, D'Souza R. M, Nosonovsky M. (2012), Study of contact angle hysteresis using Cellular Potts Model, *Physical Chemistry Chemical Physics*, 15(8), 2749-2756.
90. Mortazavi V., Nosonovsky, M. (2011a) Wear-induced microtopography evolution and wetting properties of self-cleaning, lubricating and healing surfaces, *Journal of Adhesion Science and Technology*, 1337-1359.
91. Mortazavi, V and Nosonovsky, M., (2011b), Friction-Induced Pattern-Formation and Turing systems, *Langmuir*, 4772–4779.
92. Murray J.D. (1989), *Mathematical Biology*, 2nd. ed., Springer Verlag, Berlin.
93. Nosonovsky M., & Mortazavi V., *Friction-induced vibrations and self-organization: mechanics and non-equilibrium thermodynamics of sliding contact*, CRC Press (2013).
94. Nosonovsky, M. (2010a), Self-organization at the frictional interface for green tribology, *Phil. Trans. R. Soc. A*, 368, 1929, 4755-4774.
95. Nosonovsky, M. (2010b), Entropy in Tribology: in Search of Applications, *Entropy*, 12(6), 1345-1390; doi:10.3390/e12061345.
96. Nosonovsky, M. & Adams, G. G. (2001), Dilatational and shear waves induced by the frictional sliding of two elastic half-spaces, *Int. J. Eng. Sci.* 39, 1257–1269. (doi:10.1016/S0020-7225(00)00085-9)

97. Nosonovsky, M. & Adams, G. G. (2004), Vibration and stability of frictional sliding of two elastic bodies with a wavy contact interface, *ASME J. Appl. Mech.* 71, 154–300. (doi:10.1115/1.1653684)
98. Nosonovsky M. & Bhushan, B. (2009), Thermodynamics of surface degradation, self-organization and self-healing for biomimetic surfaces, *Phil. Trans. R. Soc. A.*, 367, 1607–1627.
99. Nosonovsky M. & Bhushan, B. (2010), Surface Self-Organization: from Wear to Self-Healing in Biological and Technical Surfaces, *Appl. Surf. Sci.*, 256, 3982–3987
100. Nosonovsky, M., Amano, R., Lucci, J.M. & Rohatgi, P.K., (2009), Physical chemistry of self-organization and self-healing in metals, *Phys. Chem. Chem. Phys.*, 11, 9530–9536
101. Nosonovsky, M., V. Hejazi, A. E. Nyong and P. K. Rohatgi, Metal Matrix Composites for Sustainable Lotus-Effect Surfaces, *Langmuir*, vol. 27, no. 23, p. 14419–14424, 2011.
102. Nosonovsky, M., and P. K. Rohatgi (2011), *Biomimetics in Materials Science: Self-Healing, Self-Lubricating, and Self-Cleaning Materials*, Springer.
103. Nosonovsky, M., X. Zhang and S. Esche (2009), Scaling of Monte Carlo simulations of grain growth in metals, *Modeling Simul. Mater. Sci. Eng.*, vol. 17, p. 025004.
104. Nosonovsky, M. and S. Esche (2008), Multi-scale Effects in Crystal Grain Growth and Physical properties of metals, *Phys. Chem. Chem. Phys.*, vol. 10, pp. 5192–5195.
105. Nosonovsky M. (2007), Model for Solid-Liquid and Solid-Solid Friction for Rough Surfaces with Adhesion Hysteresis, *J. Chem. Phys.*, vol. 126, p. 224701.
106. Oliveira L. de, D. M. Lopes, S. M. M. Ramosb and J. C. M. Mombach (2011) Two-dimensional modeling of the superhydrophobic behavior of a liquid droplet sliding down a ramp of pillars, *Soft Matter*, vol. 7, p. 3763.
107. Patankar N. A. (2004), Transition between Superhydrophobic States on Rough Surfaces, *Langmuir*, vol. 20, pp. 7097–7102.

108. Pierce, E. F. J. Carmona and A. Amirfazli (2008), Understanding of sliding and contact angle results in tilted plate experiments, *Colloids and Surfaces A: Physicochemical and Engineering Aspects*, vol. 323, pp. 73-82.
109. Pockels A. (1891), Surface tension, *Nature*, vol. 43 , pp. 437-439.
110. Prigogine, I. (1968) *Thermodynamics of Irreversible Processes*. John Willey & Sons: New York.
111. Prigogine, I., (1980) *From Being to Becoming*; WH Freeman and Company: San Francisco, CA.
112. Prigogine, I. & Stengers, I. (1984) *Order Out of Chaos*; Bantam: N.Y.
113. Rubinstein, S. M., Cohen, G., and Fineberg, J. (2004.) Detachment fronts and the onset of dynamic friction. *Nature* 430 (7003): 1005–1009.
114. Saville G. (1977), Computer simulation of the liquid-solid-vapor contact angle, *Faraday II*, vol. 73, p. 1122–32.
115. Singer I L, Dvorak S D, Wahl K J, Scharf TW, (2003) Role of third bodies in friction and wear of protective coatings. *J Vac Sci Technol A*; 21:232–40.
116. Shirtcliffe N., McHale G., Atherton S. and Newton M. I. (2010), An introduction to superhydrophobicity, *Advances in Colloid and Interface Science*, vol. 161, no. 1-2, pp. 124-138.
117. Shikhmurzaev Y. (1997), *J. Fluid Mech.*, vol. 334, p. 211.
118. Sosnovskiy L.A.; Sherbakov, S.S. *Surprises of Tribo-Fatigue*; Magic Book: Minsk, 2009.  
Shenoy, V. and Sharma, A (2001) Pattern Formation in a Thin Solid Film with Interactions, *Phys. Rev. Lett.* Vol. 89:119-122.
119. Tadmor R., Bahadur P., Leh A., N'guessan H. E., R. Jaini and L. Dang (2009) Measurement of Lateral Adhesion Forces at the Interface between a Liquid Drop and a Substrate, *Phys. Rev. Lett*, vol. 103, no. 26, pp. 266101-4.

120. Tadmor R. (2008), Line energy, line tension and drop size, *Surface Science*, vol. 602, p. L108–L111.
121. Thompson P. A., Brinckerhoff W. B. and Robbins M. O. (1993), Microscopic studies of static and dynamic contact angles, *J. Adhes. Sci. Technol*, vol. 7, p. 535–41.
122. Thompson P. A. and Robbins M. O. (1989), Simulations of contact-line motion: slip and the dynamic contact angle, *Phys Rev. Lett.*, vol. 63, p. 766–69.
123. Turing, A.M. (1952), The chemical basis of morphogenesis, *Phil. Trans. R. Soc. B*, 237, 37–72.
124. Vedantam S. and Panchagnula M. (2007), Phase Field Modeling of Hysteresis in Sessile Drops, *Phys. Rev. Lett.* , vol. 99, p. 176102.
125. Wenzel R. N. (1936), Resistance of Solid Surfaces to Wetting by Water, *Indust. Eng. Chem.*, vol. 28, pp. 988-994, 1936.
126. Wu, G., Gao, F., Kaltchev, M., Gutow, J., Mowlem, J. K., Schramm, W. C., Kotvis, P. V. and Tysoe, W. T., (2002), An investigation of the tribological properties of thin KCl films on iron in ultrahigh vacuum: modeling the extreme-pressure lubricating interface, *Wear*, 252, 595-606
127. Whyman G., Bormashenko E. and Stein T. (2008), The rigorous derivation of Young, Cassie-Baxter and Wenzel equations and the analysis of the contact angle hysteresis phenomenon, *Chemical Physics Letters*, vol. 450, no. 4-6, p. 355–359.
128. Young T. (1805), An Essay on the Cohesion of Fluids, *Phil. Trans. R. Soc. Lond.*, vol. 95, pp. 65-87.
129. Zmitrowicz, A. (1987), A thermodynamical model of contact, friction, and wear, *Wear*, 114, 135-221.
130. Zwaag, S. van der, (2009), Self-healing behaviour in man-made engineering materials: bioinspired but taking into account their intrinsic character, *Phil. Trans. R. Soc. A* (2009) 367: 1689-1704.



131. Zypman, F., Ferrante, J., Jansen, M., Scanlon, K. & Abel, P. (2003) Evidence of self-organized criticality in dry sliding friction. *J. Phys. Condens. Matter* 15, L191–L196.

# CURRICULUM VITAE

**Vahid Mortazavi**

**Place of birth:** Tabriz, Iran

## Education

- B.Sc., Bu-Ali Sina University, May 2001
- Major: Mechanical Engineering
- M.Sc., Tarbiat Modares University, Tehran, May 2004
- Major: Mechanical Engineering
- PhD., University of Wisconsin-Milwaukee, January 2010 - May 2014
- Dissertation Title: Modeling of Instabilities and Self-organization at the Frictional Interface

## Awards

- UWM Distinguished Dissertation Fellowship (DDF) 2013
- UWMs Chancellor's Graduate Student Award – 2011, 2012, 2013

## Publications (highlights):

### Book

- M. Nosonovsky & V. Mortazavi, "Friction-induced vibrations and self-organization: mechanics and non-equilibrium thermodynamics of sliding contact", CRC Press (2013).

### Journal Papers

- V. Mortazavi, R. M. D'Souza & M. Nosonovsky (2013), "*Study of contact angle hysteresis using the Cellular Potts Model*", Physical Chemistry Chemical Physics, 15 (8), 2749-2756.
- R. Masoodi, P. Krishna Pillai, V. Mortazavi, and A. Ostadhossein (2013), "*Modeling Isothermal Flow in Saturated Porous Media Compressing between Two Parallel Plates*", Open Journal of Heat, Mass and Momentum Transfer, 1(2):74-83

- V. Mortazavi, C. Wang & M. Nosonovsky (2012), "*Stability of Frictional Sliding With the Coefficient of Friction Depended on the Temperature*", Journal of Tribology, 134, 041601.
- V. Mortazavi & M. Nosonovsky (2011), "*Friction-Induced Pattern Formation and Turing Systems*", Langmuir, 27 (8), 4772-4779.
- V. Mortazavi & M. Nosonovsky (2011) "*Wear-induced microtopography evolution and wetting properties of self-cleaning, lubricating and healing surfaces*", Journal of Adhesion Science and Technology, 25 (12), 1337-1359.
- M.R. Ansari & V. Mortazavi (2007) "*Transient Response of a Co-current Heat Exchanger to an Inlet Temperature Variation with Time Using an Analytical and Numerical Solution*", Numerical Heat Transfer, Part A: Applications, 52 (1), 71 – 85.
- M.R. Ansari & V. Mortazavi (2006) "*Simulation of Dynamical Response of a Countercurrent Heat Exchanger to Inlet Temperature or Mass Flow Rate Change*", Applied Thermal Engineering, 26, 401-2408, 605-636.

### **Book Chapters**

- M. Nosonovsky, V. Hejazi & V. Mortazavi (2013), "*Green and Biomimetic Tribology*" In Tribology for Scientists and Engineers (Eds. P. R. Menezes, S.P. Ingle, M. Nosonovsky, S. Kailas, M.R. Lovell, M.R.)
- V. Mortazavi, V. Hejazi, R. M. D'Souza & M. Nosonovsky (2013), "*Computational and Experimental Study of Contact Angle Hysteresis in Multiphase Systems*", In Advances in Contact Angle, Wettability and Adhesion (Ed. K. L. Mittal), Volume 001, 19-48.
- M. Nosonovsky & V. Mortazavi (2012), "*Self-Organization at the Frictional Interface*", In Green Tribology (Ed. M. Nosonovsky & B. Bhushan), Springer Berlin Heidelberg, 41-78.